Polar chromosomes are rescued from missegregation by spindle elongation-driven microtubule pivoting

Isabella Koprivec*[1], Valentina Štimac*[1], Mario Đura[1], Kruno Vukušić[1], Petra Mikec[1], Iva M. Tolić[#1]

* These authors contributed equally to this work
[#] Corresponding author

[1] Ruđer Bošković Institute, Bijenička cesta 54, 10 000 Zagreb, Croatia

ABSTRACT

Polar chromosomes, which initially attach to the mitotic spindle behind the pole, are prone to missegregation and micronuclear entrapment, contributing to chromosomal instability in cancer. Yet, the mechanisms ensuring their faithful segregation remain unclear. Here, we show that polar chromosomes require a unique step involving spindle elongation, which repositions chromosome-bound astral microtubules by pivoting them around the centrosome toward the spindle surface. By modulating Eg5/KIF11 activity, we demonstrate that spindle elongation determines the direction and extent of pivoting, with microtubules from the opposite spindle half facilitating final movement. Kinetochores on polar chromosomes form mixed lateral and immature monotelic attachments, recruiting corona components and partially Mad2, but lacking Astrin. In several cancer cell lines, limited spindle elongation delays polar chromosome resolution, whereas enhanced elongation accelerates it. These findings highlight the role of spindle elongation in the timely rescue of polar chromosomes from the 'danger zone' behind the pole, and provide mechanistic insight into how chromosome congression errors can arise in cancer.

Introduction

Chromosomes must efficiently congress to the equatorial plane of the spindle to ensure proper segregation (Maiato et al., 2017). Based on their position at the nuclear envelope breakdown (NEBD), chromosomes undertake different pathways toward the equator, resulting in distinct congression efficiencies and segregation error rates (Vukušić and Tolić, 2022). Chromosomes behind the spindle poles are particularly at risk of missegregation, as they are shielded by the pole and require a multi-step process to reach the equator (Barisic et al., 2014; Klaasen et al., 2022). First, these chromosomes approach the spindle pole from the back through centripetal movement driven by kinetochore dynein pulling along astral microtubules and nuclear actomyosin (Barisic et al., 2014; Booth et al., 2019; Li et al., 2007; Rieder and Alexander, 1990; Yang et al., 2007). Subsequently, the chromosomes travel along the main spindle surface using CENP-E at kinetochores, pulling forces by end-on attached microtubules, and polar ejection forces (Barisic et al., 2014; Cai et al., 2009; Craske and Welburn, 2020; Kapoor et al., 2006; McEwen et al., 2001; Renda et al., 2022; Shrestha and Draviam, 2013; Vukušić and Tolić, 2024; Wandke et al., 2012). However, the mechanism by which polar chromosomes traverse the pole and shift from the astral region to the main spindle remains unknown.

Chromosomes that fail to escape the area behind the pole before the spindle fully forms risk stabilization of improper attachments, ensheathment by the endoplasmic reticulum, and missegregation in case of the spindle assembly checkpoint (SAC) weakness, bypass or delayed satisfaction (Dick and Gerlich, 2013; Ferrandiz et al., 2022; Gomes et al., 2022; Kabeche and Compton, 2013; Klaasen et al., 2022). Recent studies discovered that such unaligned (i.e., behind the spindle pole) and misaligned (i.e., near the pole on the main spindle) chromosomes represent an important source of segregation errors, with the highest probability of ending up in micronuclei, the strongest correlation with chromosomal instability, and a direct link to metastatic potential (Gomes et al., 2022; Tucker et al., 2023). Several labs have observed mis- and unaligned chromosomes in cancer cell lines, such as ovarian, bone, colorectal and breast cancer, and in patient samples of primary and metastatic breast cancer (Ertych et al., 2014; Gomes et al., 2022; Tamura et al., 2020; Tucker et al., 2023). Multiple lines of evidence also indirectly suggest that chromosome 1, whose 1q arm gain directly leads to cancer development and malignant transformation, might often be located behind the pole and thus at risk of unalignment (Bolzer et al., 2005; Girish et al., 2023; Klaasen et al., 2022; Tovini and McClelland, 2019). While these implications highlight the importance of escaping the polar region on time, the reason why chromosomes occasionally fail to do so, especially in cancer cells, is still unclear.

Here, we develop approaches integrating stimulated emission depletion (STED), lattice light-sheet (LLS), and confocal microscopy with molecular perturbations to overcome spatiotemporal resolution barriers that hinder studies of polar chromosome dynamics, which occurs quickly within a spindle region that is densely populated with microtubules. We present a mechanism crucial for chromosome segregation, based on a fundamental, yet previously unexplored, property of centrosome-anchored microtubules—their ability to pivot around the centrosome. Our study reveals that spindle elongation prompts microtubules attached to polar chromosomes to pivot towards the center of the spindle, releasing the chromosomes from the

"danger zone" behind the spindle pole and enabling their contact with the spindle surface. During pivoting, polar chromosomes form predominantly mono-lateral and other complex attachments with astral microtubules, which persist until the chromosome contacts the spindle surface and contribute to spindle assembly. From a functional perspective, we demonstrate a critical role of spindle elongation-driven pivoting in promoting timely mitosis and preventing chromosome alignment errors in cancer cells, suggesting potential strategies to modulate these errors.

Results

Polar chromosomes require a unique congression step to transit across the spindle pole

Given that chromosomes located behind the spindle pole at NEBD take longer to congress to the metaphase plate in comparison to other chromosomes (Klaasen et al., 2022), we hypothesized that they require a specific congression step. Alternatively, they may exhibit slower progression of the steps shared with other chromosomes. To distinguish between these possibilities, we imaged human retinal pigment epithelium (RPE1) cells with labeled centromeres and either tubulin or centrosomes using a synergy of STED immunofluorescence (Figure 1A) and LLS live-cell imaging (Figure 1B). STED microscopy enabled visualization of microtubules within the polar region in super-resolution (50-100 nm, Supplementary Figure 1A) (Koprivec et al., 2025). This level of resolution was essential for distinguishing individual microtubules or small bundles together with their attachments to kinetochores within a microtubule-packed region, considering that human spindles contain about 6000 microtubules (Kiewisz et al., 2022). LLS microscopy enabled imaging of all kinetochores throughout mitosis at a time resolution of 6 seconds due to the low phototoxicity of this technique (Shi et al., 2024). The high time resolution was crucial for tracking individual polar kinetochores, as they move quickly and pass closely by other kinetochores (Video 1).

By using LLS movies (Figure 1B), we found that at NEBD, 15 ± 2 chromosomes per cell (all data are given as mean ± SEM, n = 24 cells) were located behind the spindle poles (Supplementary Figure 1B-D). Out of those 15, 8 ± 1 ended their centripetal movement in the region between the two poles, whereas 7 ± 1 chromosomes ended their centripetal movement in the region behind the pole (see examples in Figure 1A and Supplementary Figure 1B). We refer to the latter group as polar chromosomes. By constructing a timeline of the polar chromosome movements (Figure 1B-C, see individual stages inferred from the arrangements of microtubules and kinetochores in Figure 1A), we found that after NEBD a typical polar chromosome started its centripetal movement approaching the spindle pole from the back until it reached a relatively stable distance from the pole at 3.4 ± 0.2 minutes, which roughly corresponds to the formation of the prometaphase chromosome ring around the nascent spindle (Magidson et al., 2011). Remarkably, it took additional 4 minutes for polar chromosomes to reach the spindle surface, an event we term "landing", which occurred 7.4 ± 0.3 minutes after NEBD (Figure 1B-C). During this time gap, the spindle rapidly elongated and other chromosomes have already started congressing to the metaphase plate. Once the polar

111 chromosomes landed on the spindle surface, they immediately started traveling towards the
112 spindle midplane, finishing aligning at 12.3 ± 0.3 minutes (Figure 1B-C, Supplementary Figure
113 1E).

114 The observed time gap may be specific to the location of polar chromosomes behind
115 the pole in prometaphase, but it may also be due to their large distance to the spindle midplane.
116 To discriminate between these possibilities, we compared the timing of polar and non-polar
117 chromosomes with a similar initial distance to the centrosome midpoint (Supplementary Figure
118 1F), and found that only polar chromosomes showed a delay in landing and a time gap from
119 the end of the centripetal movement to the attachment to the spindle surface, indicating that the
120 gap is specific to chromosome location (Supplementary Figure 1G-H). The other segments of
121 the chromosome's travel, the centripetal movement and the transfer along the spindle surface,
122 lasted similarly for polar and non-polar chromosomes (Supplementary Figure 1I-J), which
123 argues against polar chromosomes having slower progression of shared steps. Thus, the
124 delayed alignment of polar chromosomes causing their susceptibility to missegregation is due
125 to a time gap wherein the polar chromosome traverses across the pole to reach the main spindle
126 surface. This reveals an additional step in congression specific to polar chromosomes (Figure
127 1D).

128 To test whether this additional step includes the attachments to microtubules, we
129 analyzed STED images (Figure 1A) and found that 58.1 ± 3.2 % of chromosomes already had
130 microtubules next to their kinetochores at a time close to NEBD, whereas 41.9 ± 3.2 % were
131 completely unattached (Supplementary Figure 1K-L). By the end of the centripetal movement
132 phase all kinetochore pairs were attached to microtubules and remained attached throughout
133 the subsequent phases (Supplementary Figure 1K-L). Some of the chromosomes that were
134 unattached and located behind the pole at NEBD might have remained unattached as they were
135 passed by the moving centrosome, resulting in their first contact with spindle microtubules
136 between the spindle poles. In contrast, all polar chromosomes, which made the first contact
137 behind the pole, were attached to microtubules during the transit across the pole. Thus, pole
138 crossing by the polar chromosomes involves the attachment of kinetochores to microtubules.

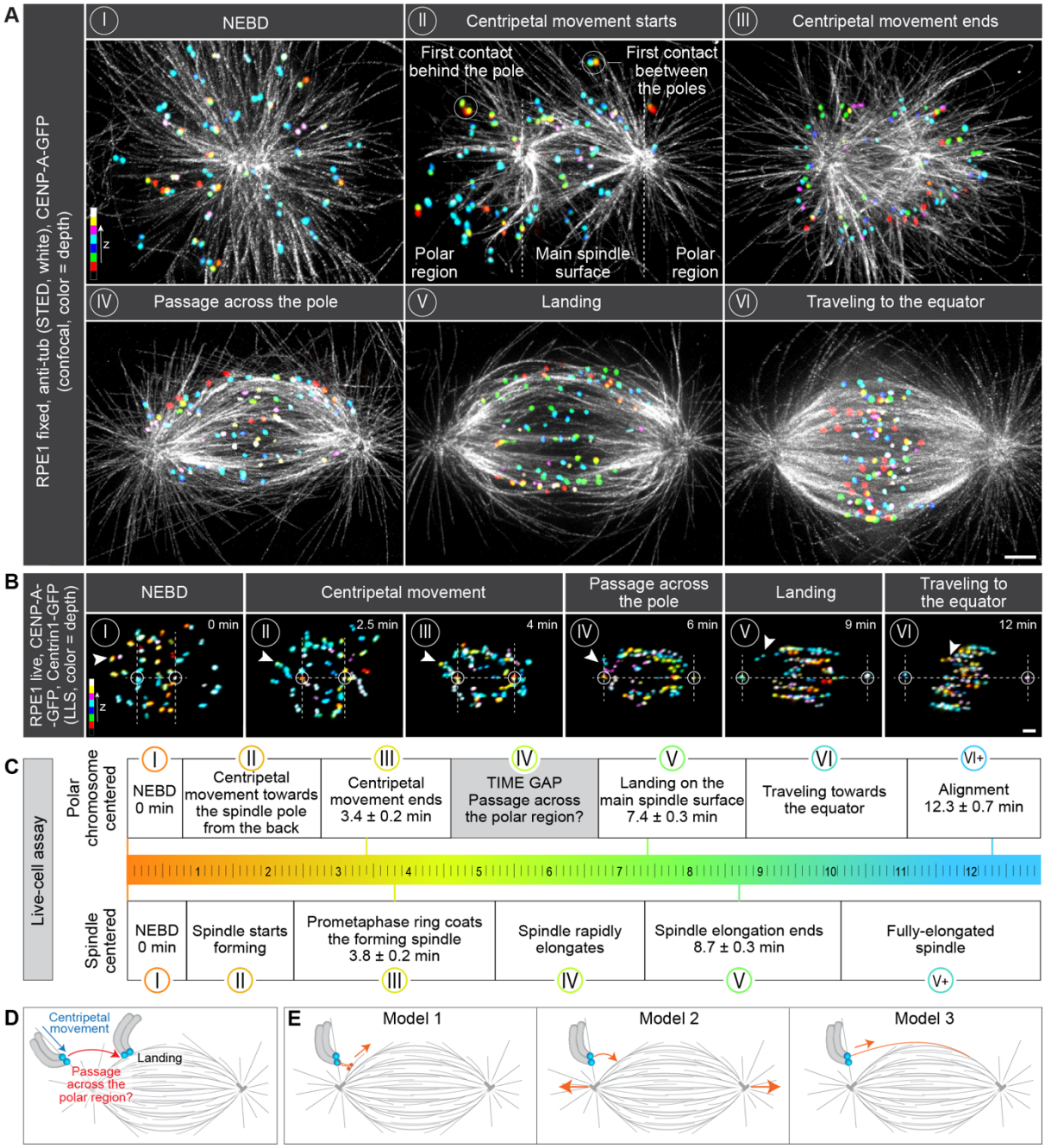

Figure 1. Polar chromosomes require an additional congression step to pass the polar region. **(A)** STED superresolution images of microtubules immunostained for α-tubulin (white) in RPE1 cells stably expressing CENP-A-GFP (colorful, confocal). Images show maximum intensity projections of the whole cell. Kinetochores are color-coded for depth with the brgbcmyw LUT in ImageJ throughout 8-12 z-planes in prometaphase and 35 z-planes in metaphase, corresponding to 2.4-3.6 µm and 10.5 µm, respectively. The images represent different phases of mitosis: I – nuclear envelope breakdown (NEBD), II – a spindle starts forming and kinetochores in the polar region start their centripetal movement towards the spindle pole from the back, III – a prometaphase ring forms and centripetal movement of kinetochores ends, IV – a spindle rapidly elongates while kinetochores located at the back of the pole pass the polar region, V – spindle elongation ends and all kinetochores land onto the

152 spindle surface, VI – a spindle is fully elongated and kinetochores travel towards the spindle
153 equator. These stages were inferred from the arrangements of microtubules and kinetochores,
154 see Methods. The polar region and the main spindle surface are denoted in image II. **(B)** Time-
155 lapse images of RPE1 cells stably expressing CENP-A-GFP and Centrin1-GFP (colorful,
156 lattice light-sheet). Images show maximum intensity projections of the whole cell.
157 Kinetochores are color-coded for depth with the brgbcmyw LUT in ImageJ throughout 32-40
158 z-planes, corresponding to 4.6-5.8 µm. Mitotic phases from I to VI correspond to the ones
159 described in (A). The polar region is denoted as a region behind two dashed lines perpendicular
160 to the long spindle axes. Centrosomes are denoted with white circles. White arrows represent
161 one polar kinetochore pair tracked from NEBD until alignment to the spindle equator. **(C)** Polar
162 chromosome-centered (upper) and spindle-centered (lower) timelines of prometaphase events.
163 Events are marked with roman numerals that correspond to the ones shown in (A) and (B). The
164 times are calculated based on 39 kinetochore pairs in 20 cells from 8 experiments. **(D)**
165 Schematic representation of the first (end of centripetal movement) and the last (landing)
166 known time points between which the time gap and possible passage across the polar region
167 occur. **(E)** Three possible models for passing the spindle pole. In the first model, a motor bound
168 to polar kinetochores brings them onto the spindle surface, representing diverse mechanisms
169 based on kinetochore- and chromosome-bound motors. The second model proposes that
170 spindle elongation drives pivoting of astral microtubules that consequently bring polar
171 kinetochores in front of the spindle pole. In the last model, polar kinetochores attach to
172 microtubules emanating from the opposite spindle half that bring them onto the spindle surface.
173 All scale bars, 2 µm.

174

175 **Passage across the pole occurs independently of the motor proteins implicated in**
176 **chromosome congression**

177 To uncover the mechanism of the passage across the polar region, we envisioned three models
178 (Figure 1E). In the first model, motor proteins located at the kinetochore (CENP-E or dynein)
179 or on the chromosome arm (chromokinesins) of polar chromosomes attach to the microtubules
180 of the main spindle surface and pull the polar chromosome in the direction of the spindle
181 surface. In the second model, the spindle elongates, causing both poles to move outward,
182 thereby repositioning chromosomes from the back of the spindle pole to the main spindle
183 surface. In the third model, microtubules extending from the opposite side of the spindle attach
184 to the polar chromosome and pull it towards the main spindle surface.

185 To test the first model, we depleted CENP-E (kinesin-7) (Barisic et al., 2014; Cai et al.,
186 2009; Kapoor et al., 2006; Maiato et al., 2017), Spindly, which promotes dynein recruitment
187 to kinetochores in early mitosis (Griffis et al., 2007), or co-depleted the chromokinesins KIF4A
188 (kinesin-4) and Kid (kinesin-10) (Mazumdar et al., 2004; Wandke et al., 2012; Yajima et al.,
189 2003) by using small interfering RNAs (siRNAs) (Supplementary Figure 2A). As an alternative
190 approach to disrupt CENP-E activity, we used the small-molecule inhibitor GSK923295
191 (Wood et al., 2010) (Supplementary Figure 2A). We also perturbed actomyosin contraction
192 (Booth et al., 2019) by depolymerizing actin via Latrunculin A (Supplementary Figure 2A),

193 thereby completing the test of motor-driven mechanisms that were previously implied in
194 chromosome congression (Maiato et al., 2017). Even when those proteins were effectively
195 depleted or inhibited, as determined by a ~90 % reduction of their signal, absence from the
196 expected location, and the characteristic phenotype (Supplementary Figure 2B-C), nearly all
197 polar chromosomes successfully traveled from the back of the spindle towards the main spindle
198 surface (Supplementary Figure 2D). A tiny fraction (~2 %) of polar chromosomes after Spindly
199 depletion remained behind the pole, as they were ejected more than 6 µm away from the pole
200 into the region beyond the future area of the spindle (Supplementary Figure 2D-E). In contrast,
201 in control cells, polar kinetochores approached the pole and remained at a distance of about 3
202 µm, indicating the importance of proximity to the pole for successful passage across the pole
203 (Supplementary Figure 2E). Given that Spindly and CENP-E are essential for the expansion of
204 the kinetochore fibrous corona (Pereira et al., 2018; Sacristan et al., 2018; Wu et al., 2023),
205 these data show that the expanded corona is dispensable for the initial chromosome transit
206 across the pole. Taken together, these results show that the passage across the pole occurs
207 independently of the previously described congression drivers, but benefits from the role of
208 dynein in keeping the chromosomes close to the spindle pole.

209

210 **Pivoting of astral microtubules around the centrosome repositions polar chromosomes**
211 **close to the spindle surface**

212 In the second model of polar chromosome resolution (Figure 1E), spindle elongation leads to
213 repositioning of polar chromosomes attached to astral microtubules towards the main spindle
214 surface. This model relies on two assumptions: 1) chromosome-attached microtubules are able
215 to pivot around the centrosome, 2) chromosomes move through the cytoplasm considerably
216 less than the centrosomes. To explore these assumptions, we tracked in 3D the polar
217 kinetochores and their microtubules, as well as centrosomes and chromosome arms, from the
218 end of the centripetal movement until after landing on the spindle surface (Figure 2A-C,
219 Supplementary Figure 2F, Video 2-4). To quantify the pivoting motion of a polar chromosome,
220 we measured the angle between the centrosome-centrosome axis and the line connecting the
221 sister kinetochores midpoint with the centrosome, termed "pivoting angle" (Figure 2D). The
222 pivoting angle showed a fast decrease during the period of rapid spindle elongation and
223 stabilized as the spindle length stabilized (Figure 2E-F). Moreover, the pivoting angle was
224 strongly anti-correlated with the spindle length for individual kinetochore pairs (Figure 2G,
225 Supplementary Figure 2G). These results indicate that polar kinetochores, along with their
226 attached microtubules, pivot around the centrosome towards the spindle center.

227 To directly see the pivoting motion of astral microtubules, which are undetectable in
228 typical videos of mitosis, we developed a confocal microscopy protocol with adjusted pixel
229 size (See Methods) to image RPE1 cells expressing EYFP-α-tubulin with added HaloTag-
230 CENP-A (Figure 2A, Video 2 and 3). The kinetochores of a polar chromosome were found to
231 be adjacent to a microtubule signal representing a single astral microtubule, or a few in a
232 bundle. We found that this astral microtubule pivoted around the centrosome in the direction
233 of the spindle surface, while maintaining its connection to the polar chromosome, during the

234 centrosome's movement outwards (Figure 2A and 2H-I). The microtubules remained straight
235 instead of bending (Supplementary Figure 2H), indicating that the entire microtubule pivots
236 around the centrosome, as opposed to solely the plus-end-proximal segment gliding along the
237 cell cortex or organelles. Overall, these direct observations of microtubule pivoting support the
238 second model and indicate that the force driving the pivoting of chromosome-attached
239 microtubules exceeds the force preserving their extension direction at the centrosome.

240 In contrast to the chromosome-carrying astral microtubules, the microtubules that were
241 not attached to a chromosome did not exhibit directed pivoting but instead pivoted around the
242 centrosome in a random manner (Figure 2B and 2H-I, Supplementary Figure 2I-J). Their
243 pivoting was similar in the cases when their centrosome moved significantly and when it
244 appeared stationary (Figure 2B and 2H-I, Supplementary Figure 2I-K). Stationary poles were
245 observed in cells where one pole was positioned at the nuclear border during NEBD, resulting
246 in the absence of polar chromosomes and the presence of only chromosome-free microtubules
247 at this pole. Whereas chromosome-carrying microtubules pivoted by ~36°, on average, in 3
248 minutes, the chromosome-free microtubules changed their angle by less than ~8° irrespective
249 of the pole movement (Supplementary Figure 2I). These findings suggest that the force driving
250 the pivoting of chromosome-free microtubules is independent of the centrosome movement
251 and smaller than the force maintaining their direction at the centrosome.

252 For spindle elongation to reposition polar chromosomes towards the main spindle
253 surface, chromosomes must move less than centrosomes during this process. This was
254 confirmed by temporal maximum-intensity projections of spindles labeled with EB3-GFP and
255 H2B-mCherry, which showed that chromosomes remained relatively stationary while the
256 centrosomes moved outward (Figure 2C, Video 4). Collectively, these findings support the
257 model in which spindle elongation induces pivoting of astral microtubules attached to
258 stationary polar chromosomes (Figure 2J), enabling their interaction with the spindle surface.

259

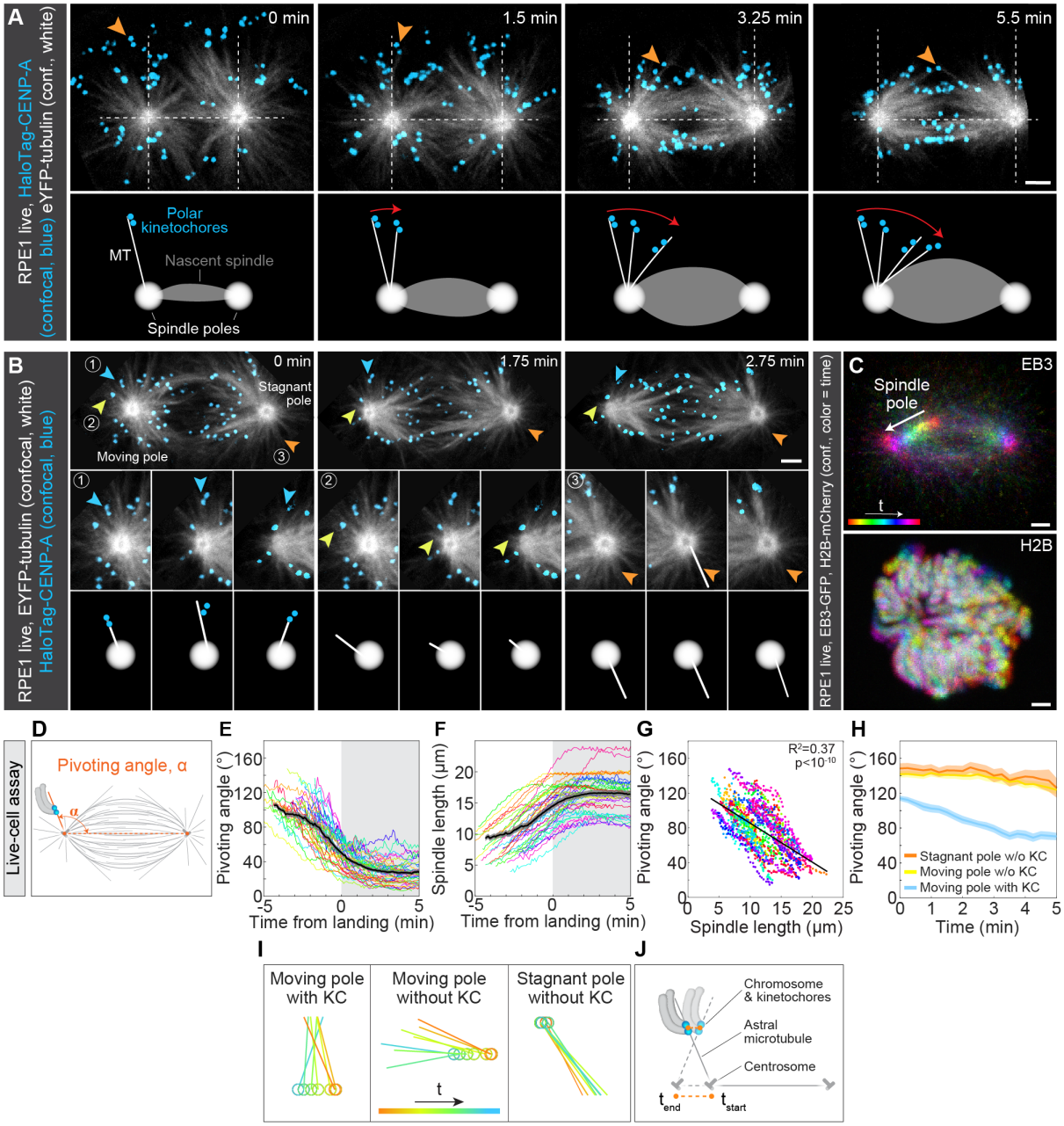

Figure 2. Polar chromosomes rely on spindle elongation-driven pivoting of astral microtubules to pass the polar region. **(A)** Upper panel: time-lapse images of RPE1 cells stably expressing EYFP-tubulin (white, confocal) and H2B-mRFP (not imaged) with added HaloTag-CENP-A (blue, confocal). Each image represents a single central z-plane and was rotated and cropped to align the spindle horizontally and position it in the center of the frame. The orange arrow denotes the kinetochore pair attached to the pivoting astral microtubule. Lower panel: Schematic representation of pivoting (red arrow) based on the images from the upper panel, showing the current and previous microtubule positions. **(B)** Time-lapse images of RPE1 cells stably expressing EYFP-tubulin (white, confocal) and H2B-mRFP (not imaged) with added HaloTag-CENP-A (blue, confocal). Moving and stagnant spindle poles are denoted in the first image. The blue arrow represents the microtubule attached to the polar kinetochore

273 tracked over time. Yellow and orange arrows represent microtubules without attached polar
274 kinetochores on the moving and stagnant spindle pole, respectively. Insets and schematic
275 representations of the previously described microtubule types are shown below the images of
276 the whole spindle; spindle poles are depicted as white circles. Images are maximum intensity
277 projections of 3 central z-planes, corresponding to 3 µm. **(C)** Images of RPE1 cells stably
278 expressing EB3-GFP (colorful, confocal, upper image) and H2B-mCherry (colorful, confocal,
279 lower image). Images are temporal maximum intensity projections of the centrosome (upper)
280 and chromosome (lower) movements over 3 central z-planes (3 µm) and a time period of 3.3
281 minutes, color-coded for time with the Spectrum LUT in ImageJ. Spindle pole movement is
282 depicted with white arrow. **(D)** Schematic representation of measured parameters for polar
283 kinetochores along with the starting (end of centripetal movement) and last (landing) tracking
284 point (t = 0 minutes). Spindle length was determined as the distance between the two spindle
285 poles. The pivoting angle was determined as an angle that the midpoint of the kinetochore pair
286 closes with the long spindle axis. **(E)** The pivoting angle of polar kinetochore pairs and **(F)**
287 corresponding spindle length in time. The landing point of each kinetochore pair is set to zero.
288 Values are shown as mean (dark line) and SEM (shaded areas). N = 39 kinetochore pairs in 20
289 cells from 8 experiments. **(G)** Anticorrelation of the pivoting angle and spindle length for the
290 same polar kinetochores as in (E). Each color represents one polar kinetochore pair and each
291 dot represents its pivoting angle and the corresponding spindle length in time. Linear
292 regression. N = 39 kinetochore pairs in 20 cells from 8 experiments. **(H)** The pivoting angle of
293 the microtubule attached to the kinetochores on the moving pole (blue), microtubule without
294 attached kinetochores on the moving pole (yellow) and microtubule without attached
295 kinetochores on the stagnant pole (orange) in time. Values are shown as mean (dark line) and
296 SEM (shaded areas). N = 16 microtubules with polar kinetochores attached to them on the
297 moving pole in 10 cells from 4 experiments. N = 16 microtubules without polar kinetochores
298 attached to them on the moving pole in 10 cells from 4 experiments. N = 14 microtubules
299 without polar kinetochores attached to them on the stagnant pole in 6 cells from 4 experiments.
300 The fourth group, microtubules with polar kinetochores attached to them on the stagnant pole,
301 could not be found, as poles were stagnant only when they were already at the nuclear border
302 at NEBD and, therefore, had no polar chromosomes to begin with. **(I)** Schematic representation
303 of the spindle pole movement and pivoting angle for each microtubule marked in (B) in time
304 (from red to blue). Note that only the microtubule attached to polar kinetochores pivots around
305 the spindle pole. **(J)** Schematic representation of the centrosome, astral microtubule and
306 chromosome movements during pivoting. Note that the centrosome moves significantly while
307 microtubules pivot under the weight of a chromosome which moves only slightly. All scale
308 bars, 2 µm.

309

310 **Direction of the centrosome movement dictates the direction of microtubule pivoting**

311 The pivoting model provides a straightforward prediction: if the spindle dynamics reverses
312 from elongation to shortening, the direction of microtubule pivoting should also reverse,
313 implying that microtubules should pivot towards the region behind the spindle pole instead of
314 towards the main spindle surface. Similarly, a constant spindle length should be associated with

315 negligible pivoting. To test these predictions, we designed a set of manipulations of Eg5/KIF11
316 (kinesin-5), the main motor protein driving spindle elongation (Kapitein et al., 2005; Kashina
317 et al., 1997), to either reverse, restore, or block spindle elongation (Figure 3A-D, Video 5 and
318 6).

319 To reverse spindle elongation into shortening, we added the Eg5 inhibitor STLC (S-
320 Trityl-L-Cysteine) (Skoufias et al., 2006) during prometaphase at a point when the spindle had
321 formed, and the kinetochores of polar chromosomes approached the main spindle surface but
322 had not yet attached to it. After the addition of STLC, the spindle started shortening, and the
323 kinetochores of the polar chromosomes that were already close to the spindle surface started
324 pivoting towards the back of the spindle (Figure 3B, Video 5). This reversed pivoting was
325 evident as an increase in the pivoting angle during spindle shortening in STLC-treated cells, in
326 contrast to the decrease of the pivoting angle during spindle elongation in untreated cells
327 (Figure 3E-F, Supplementary Figure 3A-C). Remarkably, the pivoting direction was reversible,
328 moving back and forth (Figure 3D, Supplementary Figure 3D, Video 6). The washout of the
329 Eg5 inhibitor monastrol (Mayer et al., 1999) reversed the inhibitor-induced spindle shortening
330 into elongation, which triggered kinetochore pivoting towards the main spindle surface (Figure
331 3G-H). The number of kinetochore pairs behind the pole decreased before monastrol addition,
332 increased during monastrol treatment, and decreased again after monastrol washout (Figure
333 3I), in agreement with the predictions from the model.

334 To block spindle elongation, we added the ATP-competitive Eg5 inhibitor FCPT (2-(1-
335 (4-fluorophenyl)cyclopropyl)-4-(pyridin-4-yl)thiazole) (Groen et al., 2008; Rickert et al.,
336 2008), which induces tight binding of Eg5 onto microtubules. Subsequently, the spindle length
337 remained constant, and the kinetochores of polar chromosomes did not pivot significantly,
338 providing further support to the model (Figure 3C and 3E-F, Supplementary Figure 3A-B and
339 3E, Video 5). Finally, to exclude the possibility that the observed effects of Eg5 inhibitors were
340 due to roles of Eg5 other than driving spindle elongation, we employed an orthogonal approach.
341 This involved adding a low dose of nocodazole (20 nM), which induces mild spindle shortening
342 after NEBD while preserving the attachments of chromosomes to astral microtubules
343 (Rajendraprasad et al., 2021). In agreement with the results from Eg5 inhibition, spindle
344 shortening caused an increase in the number of kinetochores behind the pole (Supplementary
345 Figure 3F-H). Collectively, these data show that the centrosome movement due to spindle
346 elongation or shortening dictates the direction of kinetochore pivoting.

347 To quantitatively test our model, we explored whether the extent of pivoting can be
348 explained by the extent of spindle elongation or shortening. A strong correlation between the
349 change in spindle length and the simultaneous change in the pivoting angle supports this notion
350 (Figure 3J). Moreover, we calculated the expected change in the pivoting angle for a given
351 change in the spindle length, assuming immobile chromosomes (see Methods and
352 Supplementary Figure 3I). The resulting theoretical prediction closely matched the linear fit of
353 the data (Figure 3J). Taken together, our results reveal spindle elongation as a necessary and
354 sufficient driver of chromosome passage across the spindle pole, dictating both the direction
355 and magnitude of pivoting of chromosome-carrying astral microtubules (Figure 3K).

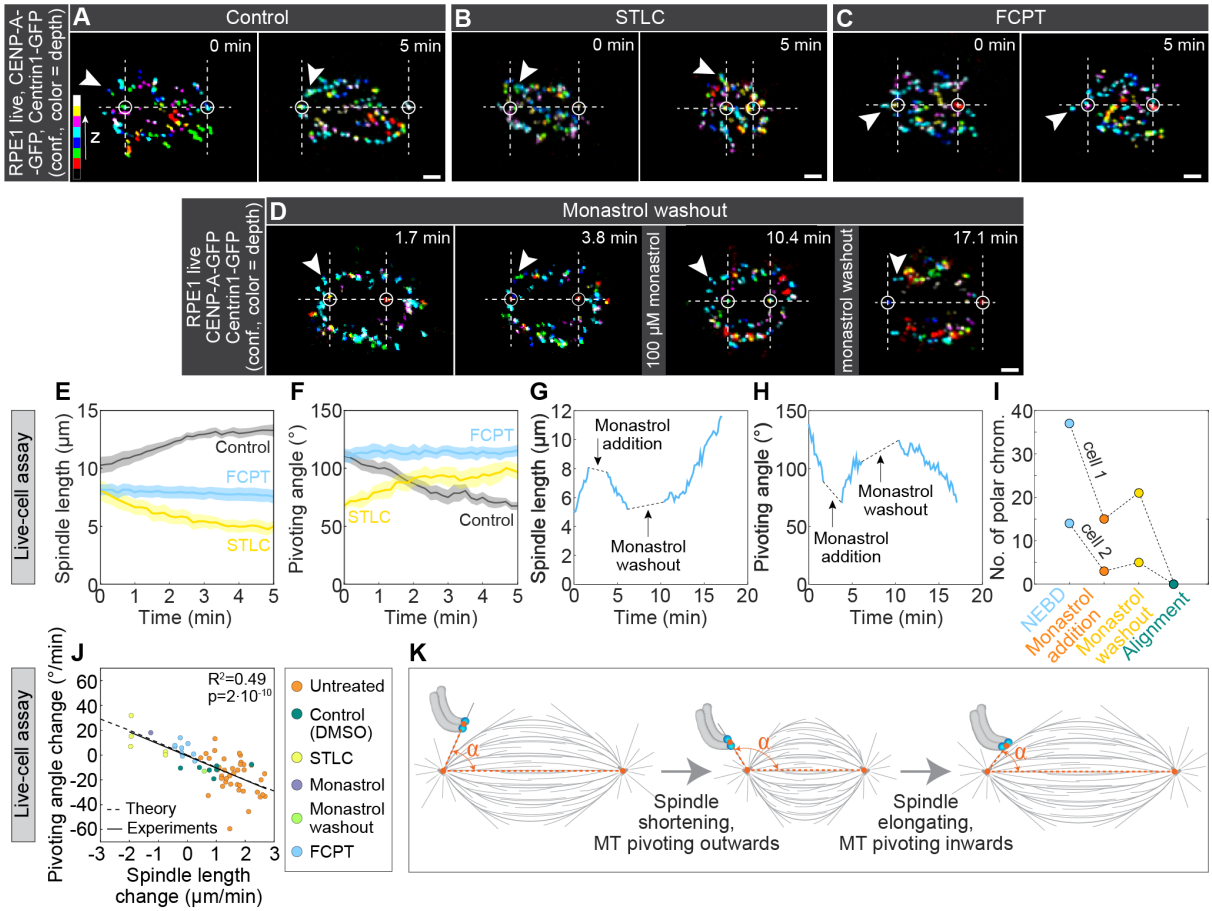

Figure 3. Centrosome movement determines the direction and magnitude of pivoting. **(A-D)** Time-lapse images of RPE1 cells stably expressing CENP-A-GFP and Centrin1-GFP (colorful, confocal) for (A) DMSO control, (B) STLC-, (C) FCPT-, and (D) monastrol-treated cells. White arrows represent one polar kinetochore pair over time. White circles represent spindle poles, horizontal dashed lines represent the long spindle axis and lines perpendicular to it denote the borders of the polar region. Note that the STLC treatment caused spindle shortening, FCPT treatment blocked spindle elongation, whereas monastrol treatment caused spindle shortening that could be reversed by washout. Kinetochores are color-coded for depth with the brgbcmyw LUT in ImageJ throughout 14-21 z-planes, corresponding to 5.6-8.4 µm. **(E)** Spindle length and **(F)** pivoting angle in time for polar kinetochores in control (gray), STLC (yellow) and FCPT (blue) treatment. Values are shown as mean (dark line) and SEM (shaded areas). t = 0 minutes corresponds to inhibitor addition and activity. N = 7 kinetochore pairs in 7 cells from 7 experiments (DMSO), N = 5 kinetochore pairs in 3 cells from 3 experiments (STLC), N = 9 kinetochore pairs in 7 cells from 7 experiments (FCPT). **(G)** Spindle length and **(H)** pivoting angle in time during the monastrol washout experiment, for the spindle and kinetochore pair marked in (D). Dashed lines denote the time required for the addition or washout of monastrol together with the time required for the spindle length to start changing. **(I)** Number of chromosomes behind the pole at the indicated times in the monastrol washout experiment for Cell 1 (shown in (D)) and Cell 2 (shown in Supplementary Figure 3D). **(J)** The experimental correlation of the pivoting angle change and spindle length change for the control

(orange), DMSO control (dark green), monastrol washout (light green), FCPT (blue), monastrol (purple) and STLC (yellow) treatments along with the theoretical curve calculated based on the experimental parameters from DMSO and STLC experiments (See Supplementary Figure 3). Linear regression. **(K)** Schematic representation of pivoting angle change based on the spindle length change. All scale bars, 2 µm.

Polar chromosomes form complex attachments yet remain bound to the same microtubule during pivoting

Prior to establishing end-on attachments, kinetochores initially bind to microtubules laterally (Alexander and Rieder, 1991; Magidson et al., 2011; Shrestha and Draviam, 2013). To explore the types of attachments that polar kinetochores form with astral microtubules during their pivoting, and to determine if they transition between different microtubules, we imaged microtubules by STED microscopy in fixed RPE1 cells expressing CENP-A-GFP, at various stages between the end of chromosome centripetal movement and landing (Figure 4A). Surprisingly, rather than primarily observing lateral attachments, we found a wide variety of attachment types, including lateral, monotelic, and syntelic configurations, together with more complex and previously unidentified types (Figure 4A). We define them as: 1) bilateral, when two sister kinetochores attach laterally to two astral microtubules, 2) mono-lateral, when one sister kinetochore has an end-on attachment in addition to both sisters being laterally attached to the same astral microtubule, 3) mono-bilateral, as a combination of bilateral and one end-on attachment, and 4) syn-lateral, as a combination of syntelic and one lateral attachment. Mono-lateral attachments were the most frequent, followed by lateral and bilateral ones (Figure 4B).

To explore if chromosomes can switch from one microtubule to another during pivoting, we imaged live cells expressing EYFP-α-tubulin and H2B-mRFP with HaloTag-CENP-A (Supplementary Figure 4B). We found that 63.1 ± 11.1 % of polar chromosomes remained attached to a single microtubule during pivoting, 21.1 ± 9.4 % made one change between microtubules, whereas multiple changes were rare (Figure 4C). Most of the observed changes included only a change for the further kinetochore, whereas the closer one remained attached to the same microtubule during the entire process (Figure 4D and Supplementary Figure 4B). Thus, in a typical case with 7 polar chromosomes, 4 of them remain attached to a single microtubule during pivoting, 2 change the attachment of the further kinetochore, e.g. from lateral to bilateral, whereas 1 shows a more complex transition (Figure 4E). In sum, polar chromosomes make a variety of attachments with astral microtubules but typically remain attached to the same microtubules while crossing the polar region.

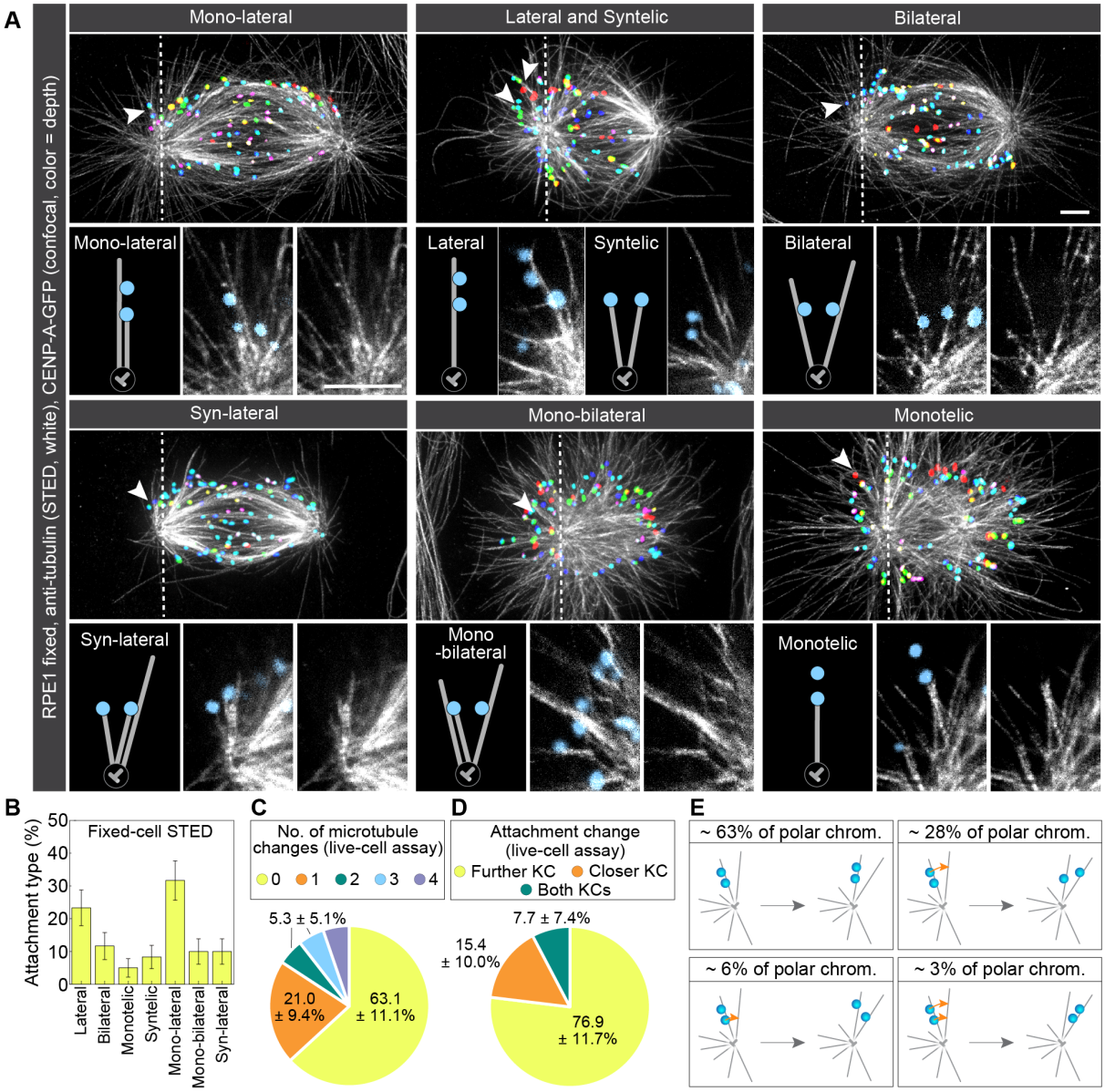

Figure 4. Polar kinetochores form complex attachments with the microtubules they remain attached to during pivoting. **(A)** STED superresolution images of microtubules immunostained for α-tubulin (white) in RPE1 cells stably expressing CENP-A-GFP (colorful, confocal). Images show maximum intensity projections of the whole cell. Kinetochores are color-coded for depth with the brgbcmyw LUT in ImageJ throughout 8-17 z-planes, corresponding to 2.4-5.1 µm. White arrows represent a kinetochore pair attached to microtubules shown in insets below the image. Insets show single z-planes or maximum intensity projections of 2-3 z-planes where the microtubule of interest is located, smoothed with 0.75-mm-sigma Gaussian blur. The schematic representations of different attachment types are shown next to the associated insets. **(B)** Fractions of different attachment types for polar chromosomes between the end of the centripetal movement and landing quantified from STED images. N = 60 kinetochore pairs in 24 cells from 5 experiments. **(C)** Pie chart for the number of microtubule changes during pivoting measured in live RPE1 cells stably expressing EYFP-tubulin with added HaloTag-CENP-A (See Supplementary Figure 4). N = 19

428 kinetochore pairs in 10 cells from 4 experiments. **(D)** Pie chart for attachment changes on
429 further (yellow), closer (blue) and both (green) polar kinetochores measured in the same cells
430 as in (C). N = 13 kinetochore pairs in 5 cells from 3 experiments. **(E)** Schematic representations
431 of types of attachment changes that polar kinetochores (blue circles) undergo during pivoting
432 and their frequencies. The orange arrows denote which kinetochore in a pair changes
433 microtubules during pivoting. All scale bars, 2 µm.

434

435 **Kinetochores on polar chromosomes show molecular signatures of lateral and immature**
436 **end-on attachments**

437 To characterize the molecular nature of polar kinetochore-microtubule attachments together
438 with STED imaging of microtubules during intact early mitosis, we tested the levels of Mad2,
439 a checkpoint protein that marks kinetochores with missing or unstable end-on attachments
440 (Kuhn and Dumont, 2017; Waters et al., 1998). Among sister kinetochores, the one positioned
441 further from the pole contained higher levels of Mad2 (Figure 5A-B and Supplementary Figure
442 4A). This suggests that the further kinetochore typically forms a lateral attachment, whereas
443 the closer one forms an end-on attachment in addition to the lateral one, in agreement with
444 microtubule localization observed by STED microscopy (Figure 5A). Mad2 levels at
445 kinetochores with end-on attachments (Figure 5A) were lower than at those with lateral
446 attachments, as expected, but higher than at end-on attached kinetochores in metaphase (Figure
447 5C), suggesting that the end-on attachments on polar chromosomes are immature.

448 To assess a positive marker of end-on attachments, we examined Astrin, which localizes
449 to aligned kinetochores with low Aurora B activity, but is absent from unaligned kinetochores
450 (Mack and Compton, 2001; Schmidt et al., 2010). Consistent with these findings, we observed
451 that Astrin was absent from both polar kinetochores within a pair irrespective of their relative
452 distance to the centrosome (Figure 5D-E). It was also absent from non-polar kinetochores in
453 prometaphase, which had intermediate levels of Mad2, but was present on the kinetochores
454 aligned at the metaphase plate, which were devoid of Mad2 (Figure 5E-F).

455 The levels of CENP-E and ZW10, components of the fibrous corona that promotes
456 lateral attachments (Yao et al., 1997), were high at polar kinetochores, including both sisters,
457 indicating the presence of a large corona (Figure 5G-J). In comparison with polar kinetochores,
458 non-polar kinetochores on prometaphase spindles recruited less CENP-E and ZW10, whereas
459 the lowest signal was at aligned kinetochores in metaphase (Figure 5G-J). Taken together, these
460 results suggest that in early intact mitosis, both sister kinetochores on polar chromosomes
461 typically form lateral attachments, while the sister closer to the pole additionally establishes
462 immature end-on attachments characterized by the presence of checkpoint and corona proteins
463 and the absence of Astrin. These attachments mature as the kinetochores interact with the
464 spindle body and congress, recruiting Astrin and losing corona and checkpoint proteins
465 (Vukušić and Tolić, 2024) (Figure 5K).

466

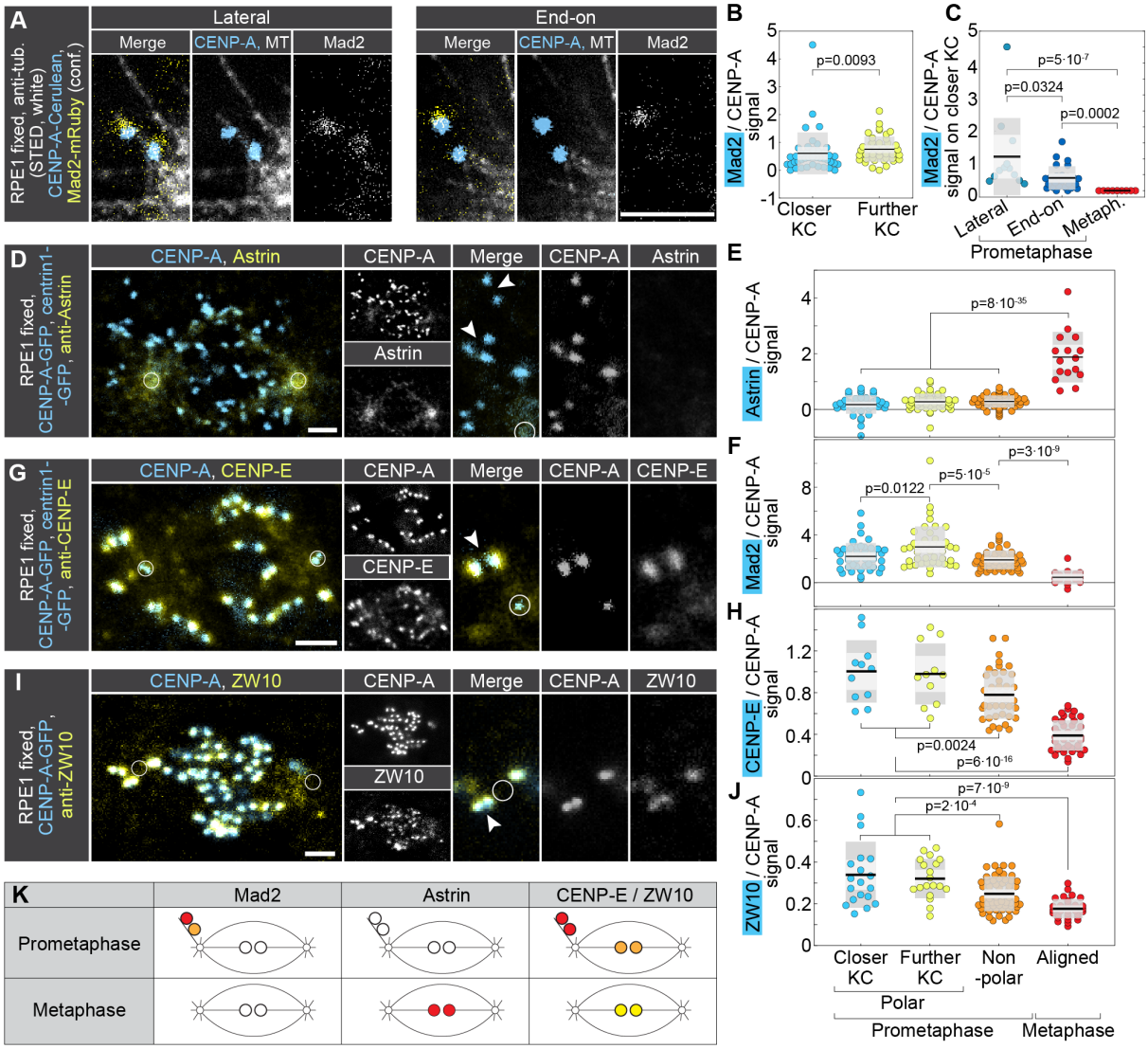

Figure 5. Kinetochores on polar chromosomes in early intact mitosis bind Mad2, CENP-E, and ZW10, but not Astrin. (A) STED superresolution images of polar chromosomes attached to microtubules immunostained for α-tubulin (white) in RPE1 cells stably expressing CENP-A-Cerulean (blue) and Mad2-mRuby (yellow). Images show a single z-plane, with kinetochores and microtubules smoothed with 0.75-mm-sigma Gaussian blur. Intensities of CENP-A and Mad2 are equally adjusted throughout the images. **(B)** Univariate scatter plot of the relative Mad2/CENP-A signal for closer (blue) and further (yellow) polar kinetochore. Measurements were done on STED images as from (A). N = 42 kinetochore pairs in 29 cells from 3 experiments. Statistical test: Mann-Whitney U test. **(C)** Univariate scatter plot of the relative Mad2/CENP-A signal for closer polar kinetochore in metaphase (blue), in prometaphase when the kinetochore makes an end-on attachment (orange) and in prometaphase when the kinetochore makes a lateral attachment (yellow). Measurements are done on STED images as from (A). N = 10 kinetochores from 5 kinetochore pairs in 2 cells from 1 experiment for metaphase, N = 26 end-on attached kinetochores and 12 laterally attached kinetochores in 29 cells from 3 experiments for prometaphase. Statistical test: Kruskal-Wallis with post-hoc

484 Dunn's test. **(D–I)** Confocal images of mitotic spindles in early prometaphase cells expressing
485 CENP-A-GFP and centrin-1-GFP (cyan), (D, G), or CENP-A-GFP alone (cyan, I),
486 immunostained for Astrin (yellow, D) and Mad2 (not shown, D), CENP-E (yellow, G), and
487 ZW10 (yellow, I). Individual fluorescence channels are shown on the right, along with merged
488 enlargements of the polar region and the corresponding individual channels. Circles denote
489 centrosome position and arrowheads point to polar kinetochores. Quantification of mean Astrin
490 (E), Mad2 (F), CENP-E (H), and ZW10 (J) signal intensities, normalized to mean CENP-A
491 levels at kinetochores, is shown for the specified spindle positions and mitotic phases. N = 116
492 kinetochore pairs in 20 cells (E and F) from 3 experiments; 92 kinetochore pairs in 8 cells (H),
493 and 115 kinetochore pairs in 10 cells (J), from 2 experiments. Statistical test in (E), (F), (H),
494 (J): ANOVA with post-hoc Tukey test. **(K)** Scheme of the observed protein levels (red: high,
495 orange: medium, yellow: low, white: absent) on polar and non-polar kinetochores (circles to
496 the upper left of the spindle and in the spindle center, respectively) in prometaphase and
497 metaphase, as indicated. All scale bars, 2 µm.

498

499 **Microtubules from the opposite spindle half help the movement of polar chromosomes**
500 **near the spindle surface**

501 To explore the contribution of microtubules extending from the other spindle half to the
502 movement of polar chromosomes (Figure 1E), we used STED microscopy and found that in
503 phases between the end of centripetal movement and landing, 30.0 ± 5.9 % of kinetochore pairs
504 in the polar region (i.e., those attached to an astral microtubule and within ~3 µm from the
505 spindle pole) were located next to a microtubule extending from the opposite side of the spindle
506 (Figure 6A), whereas 70.0 ± 5.9 % had no such microtubule nearby (Figure 6B). Attachments
507 to microtubules from the opposite spindle half were rare behind the pole, seen in only 20.5 ±
508 6.5 % kinetochore pairs, but were more frequent in the region in front of the pole, where 47.6
509 ± 10.9 % of kinetochore pairs showed attachments before joining the main spindle surface
510 (Figure 6B). Although we could not determine whether these microtubules originated at the
511 opposite pole or along the microtubules of the opposite spindle half, their origin at the opposite
512 side indicates that their plus end was facing the kinetochore. In agreement with this orientation,
513 these microtubules were attached to kinetochores predominantly in an end-on configuration
514 (Figure 6C, Supplementary Figure 5A). Most of these microtubules had tubulin intensity
515 similar to that of astral microtubules, suggesting they are single microtubules (Supplementary
516 Figure 5B).

517 If microtubules from the opposite side pull the chromosome across the pole, this is
518 expected to increase the distance between the kinetochores and the closer pole, as well as the
519 interkinetochore distance, assuming that these microtubules attach to the sister kinetochore that
520 is not end-on attached to the closer pole. We found such changes within one minute before
521 landing (Supplementary Figure 5C-D), when the kinetochores are typically close to the main
522 spindle surface (at an angle <60°, see Figure 2E), suggesting that the pulling by microtubules
523 from the opposite side contributes mainly to the last part of the chromosome movement towards
524 the spindle surface. Live-cell STED microscopy provided direct visualization of the process in

525 which such kinetochores attain end-on attachment to a microtubule extending from the opposite
526 spindle half, followed by an increase in interkinetochore distance and movement towards the
527 opposite pole (Supplementary Figure 5E). These findings show that microtubules extending
528 from the opposite side of the spindle can pull the chromosome, especially when it is already
529 close to the spindle surface. Together, our results suggest that of the 7 polar chromosomes,
530 around 5 cross the polar region and reach the main spindle surface only by elongation-driven
531 pivoting, 1-2 are pulled by microtubules from the opposite side after the initial pivoting,
532 whereas <1 chromosome per cell interacts with microtubules from the opposite side before
533 pivoting (Figure 6E).

534

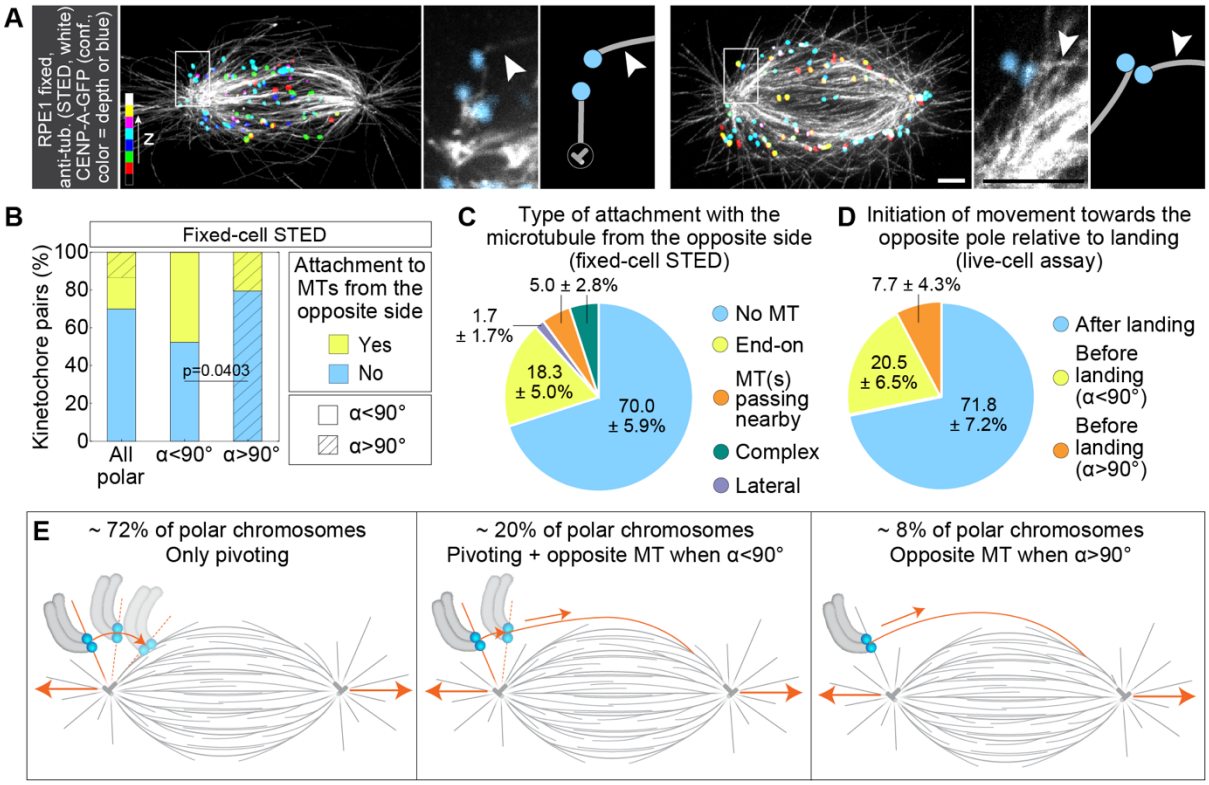

535
536

537 **Figure 6. Microtubules from the opposite side of the spindle facilitate the movement of**
538 **polar chromosomes in the region close to the spindle surface. (A)** STED superresolution
539 images of microtubules immunostained for α-tubulin (white) in RPE1 cells stably expressing
540 CENP-A-GFP (colorful, confocal). Images show maximum intensity projections of the whole
541 cell. Kinetochores are color-coded for depth with the brgbcmyw LUT in ImageJ throughout 16
542 and 9 z-planes, corresponding to 4.8 and 2.7 µm, respectively. White boxes represent regions
543 containing polar kinetochores attached to the microtubule from the opposite side of the spindle,
544 which are enlarged to the right and represented schematically. White arrows denote the
545 microtubule coming from the opposite side of the spindle. Enlargements are maximum
546 intensity projections of 2 and 3 z-planes where the microtubule of interest is located, smoothed
547 with 0.75-mm-sigma Gaussian blur. **(B)** Percentages of kinetochores that are unattached (blue)
548 or attached to the microtubule from the opposite side of the spindle (yellow) measured in cells

549 as in (A). The shaded area represents kinetochores located at the angle above 90° with respect
550 to the long spindle axis. N = 18 kinetochore pairs in 15 cells from 5 experiments. Statistical
551 test: Fisher's exact test. **(C)** Pie chart representing the percentage of different attachment types
552 with the microtubule from the opposite side. N = 18 kinetochore pairs in 15 cells from 5
553 experiments. **(D)** Pie chart representing the percentage of polar kinetochores from LLS videos
554 that initiate their movement towards the opposite pole after landing (blue), before landing at an
555 angle below 90° (yellow) and before landing at an angle above 90° (orange), indicative of a
556 force other than pivoting. N = 39 kinetochore pairs in 20 cells from 8 experiments. **(E)**
557 Schematic representation of percentages of polar chromosomes that pivot without forming an
558 attachment to the microtubule from the opposite side before landing (left), that pivot and attach
559 to microtubule from the opposite side once they reach the angle below 90° (middle) and the
560 ones that attach to microtubule from the opposite side at the angle above 90° (right). Scale bars,
561 2 µm.

562

563 **Incomplete spindle elongation leads to delayed chromosome passage across the pole and**
564 **missegregation**

565 To explore the functional relevance of the pivoting model, we asked whether incomplete
566 spindle elongation may lead to missegregation of polar chromosomes. To obtain a system with
567 chromosome segregation errors in RPE1 cells, we inhibited the mitotic kinase Mps1, a key
568 element of the spindle assembly checkpoint and the correction of erroneous attachments, by
569 the small-molecule inhibitor AZ3146 (Hewitt et al., 2010) (Figure 7A, Video 7). We reasoned
570 that due to the premature anaphase onset, spindle elongation may be incomplete in a subset of
571 cells. This should in turn lead to incomplete passage of polar chromosomes across the pole in
572 those cells, allowing us to explore the consequences of perturbed pole crossing on the
573 segregation fidelity of these chromosomes.

574 The chromosomes that were polar at NEBD missegregated more frequently than non-
575 polar chromosomes that were similarly positioned with respect to the nucleus and the
576 centrosome midpoint in Mps1-inhibited cells (Figure 7B) (Klaasen et al., 2022). Whereas polar
577 and non-polar chromosomes had a similar tendency to end up as misaligned and lagging
578 chromosomes in anaphase, there was a stark difference in the occurrence of unaligned
579 chromosomes (Figure 7B). About 20% of polar chromosomes remained unaligned throughout
580 mitosis, leading to aneuploid daughter cells. In contrast, such cases were absent in the non-
581 polar group (Figure 7B, Video 7). These results suggest that the missegregation bias towards
582 polar chromosomes is largely caused by their persistent unalignment.

583 Among the chromosomes with erroneous segregation, the persistently unaligned
584 chromosomes were the last ones to pass from the back to the front of the spindle pole
585 (Supplementary Figure 6A), suggesting that the cause for their unalignment lies in perturbed
586 passage around the pole. Based on the pivoting model, we expect that the cells that entered
587 anaphase with persistently unaligned chromosomes had less extensive spindle elongation than
588 those without unaligned chromosomes. Indeed, we found that among the Mps1-inhbited

589 spindles, those that had persistently unaligned chromosomes elongated more slowly, entering
590 anaphase at a ~4 µm shorter length than the spindles without such chromosomes (Figure 7C,
591 Supplementary Figure 6B-C). Different timing of anaphase was not the cause of persistent
592 unalignment, as the spindles with and without unaligned chromosomes entered anaphase at a
593 similar time (17.8 ± 2.5 vs. 17.9 ± 0.9 minutes). These data show that the propensity of polar
594 chromosomes to remain unaligned is higher in cells with slower spindle elongation, suggesting
595 the importance of effective chromosome passage across the pole.

596 The pivoting model may be linked with chromosome identity, as certain chromosomes
597 missegregate more frequently than others across various treatments and cancer types (Klaasen
598 et al., 2022; Worrall et al., 2018). We hypothesize that there is a zone within the interphase
599 nucleus, related to the axis of the future spindle, that would predispose chromosomes to
600 missegregate as persistently unaligned, which we term „danger zone.“ In most RPE1 cells,
601 centrosome separation occurs before NEBD, positioning one centrosome above and the other
602 below the nucleus, followed by spindle elongation and rotation that aligns the spindle parallel
603 to the coverslip surface (Magidson et al., 2011). Within this plane, we observed that in
604 prometaphase, the centrosome-centrosome axis aligns closely with the long nuclear axis from
605 the preceding interphase, as reflected by an angle of 26.1° ± 4.2° between the two axes (N =
606 24 cells, Figure 7D-F, Supplementary Figure 6D-E, Video 8). Furthermore, the nuclear axis in
607 interphase is typically aligned with the long cellular axis (Supplementary Figure 6F, Video 8)
608 (Stiff et al., 2020). This suggests that the danger zone is situated in the nuclear caps, defined as
609 regions near the ends of the major axis of the nucleus (Figure 7G, diagram), because the
610 chromosomes located there in interphase typically end up behind the centrosome in early
611 mitosis.

612 We then compared interphase positions of chromosomes 1 and 9 with respect to the
613 identified danger zone, which show a missegregation bias and random missegregation,
614 respectively (Klaasen et al., 2022) (Figure 7G). Remarkably, we found that chromosome 1
615 resides in the danger zone in 71.00 ± 2.78 % of cases. In contrast, chromosome 9 resides in the
616 danger zone in only 45.83 ± 5.87 % of cases (Figure 7H). These findings support the idea that
617 the missegregation bias of chromosome 1 arises from its preferential position in interphase
618 within the nuclear caps. Chromosomes located in this danger zone are susceptible to failure in
619 crossing the pole, leading to their persistent unalignment during mitosis (Klaasen et al., 2022).

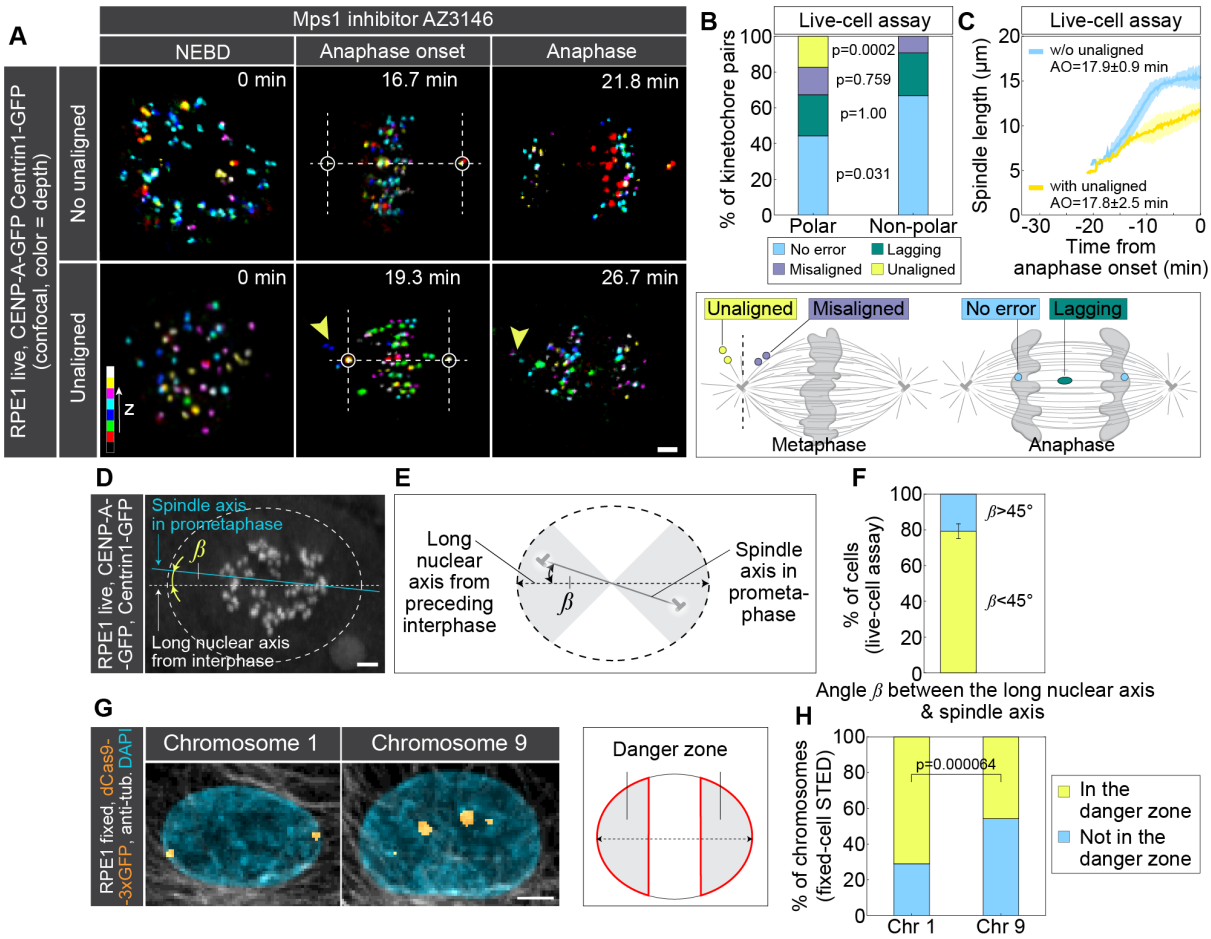

Figure 7. Incomplete spindle elongation compromises passage across the pole for polar chromosomes located in the danger zone. (A) Time-lapse images of RPE1 cells stably expressing CENP-A-GFP and Centrin1-GFP (colorful, confocal) and treated with Mps1 inhibitor AZ3146. The images show maximum intensity projections of the imaged cells. The upper panel represents cells without unaligned chromosomes and the lower panel represents cells with unaligned chromosomes. Kinetochores are color-coded for depth with the brgbcmyw LUT in ImageJ throughout 14-21 z-planes, corresponding to 5.6-8.4 µm. **(B)** Percentage of polar (left bar) or non-polar (right bar) kinetochore pairs, as determined at NEBD, that segregated normally (no error, light blue) or ended up as lagging (green), misaligned (dark blue) or unaligned (yellow) kinetochores in anaphase. Each group of kinetochores is depicted on the scheme below the graph. N = 52 polar kinetochore pairs in 7 cells from 4 experiments. N = 54 non-polar kinetochore pairs in 7 cells from 4 experiments. Statistical test: Fisher's exact test. **(C)** Spindle length in time for cells treated with AZ3146 divided into those that have (orange) or do not have (blue) unaligned chromosomes at anaphase onset. Values are shown as mean (dark line) and SEM (shaded areas). N = 3 cells with unaligned chromosomes from 2 experiments. N = 4 cells without unaligned chromosomes from 2 experiments. **(D)** RPE1 cell imaged using lattice light-sheet microscopy at the end of centripetal movement. The dashed oval denotes the approximate position of the nucleus in the preceding interphase (see Supplementary Figure 6). The straight white line denotes the position of the long nuclear axis in the preceding interphase, the blue line is the spindle axis in prometaphase at the end of the

642 centripetal movement, and β is the angle between them. The image is a maximum intensity
643 projection of 42 z-planes covering the whole cell, corresponding to 6.1 µm. **(E)** Scheme
644 showing the angle β as in (D), grey areas denote β < 45°. **(F)** Percentage of cells with β < 45°
645 (yellow) and β > 45° (blue). N = 24 cells from 8 experiments. **(G)** Images show nuclei in
646 interphase in fixed RPE1 cells stably expressing dCas9-3xGFP (orange) and stained with anti-
647 α-tubulin (gray) and DAPI (blue). Cells are transduced with lentiviruses for chromosome 1 or
648 chromosome 9, as indicated. Images are maximum intensity projections of 30 z-planes,
649 corresponding to 15 µm. The diagram on the right illustrates the "danger zone," which consists
650 of two nuclear caps. Each cap covers one-third of the nuclear long axis. Chromosomes
651 positioned in these caps during interphase are more likely to end up behind the centrosome in
652 early mitosis. **(H)** Percentage of cells with chromosome 1 or 9 located in the nuclear danger
653 zone (yellow) or outside the nuclear danger zone (blue). N = 266 chromosomes in 133 cells
654 from 4 experiments for chromosome 1. N = 72 chromosomes in 36 cells from 3 experiments
655 for chromosome 9. Statistical test: Chi-squared test. All scale bar, 2 µm.

656

657 **Spindle elongation helps to resolve polar chromosomes in cancer cell lines**

658 Finally, we set out to investigate the universality of the pivoting model by testing cancer-
659 derived cell lines. To determine whether microtubules attached to polar chromosomes pivot
660 around the spindle pole in cancer cells, we used the osteosarcoma U2OS cell line expressing
661 GFP-tagged EB3 (Stepanova et al., 2003) and CENP-A-mCherry. We visualized microtubule
662 contours using time projections of EB3 spots and observed that microtubules associated with
663 polar kinetochores pivoted around the pole as it moved outward during spindle elongation
664 (Figure 8A, Video 9). Tracking of kinetochores from NEBD to landing in live U2OS cells
665 expressing CENP-A-GFP and tubulin-mCherry showed that polar kinetochores transitioned
666 from the back to the front of the spindle pole, reflected by a decrease in their pivoting angle,
667 during spindle elongation (Figure 8B-D, Supplementary Figure 7A-B, Video 10). These
668 findings indicate that microtubule pivoting occurs during spindle elongation in U2OS cells
669 similarly to RPE1 cells.

670 To evaluate the efficiency of the pivoting mechanism in this U2OS cell line, which has
671 chromosome congression defects (Klaasen et al., 2022), we tracked and counted polar
672 kinetochores over time (Methods). We found that 96.1% of polar kinetochores successfully
673 crossed the pole and congressed to the metaphase plate, whereas 3.9% remained unaligned,
674 i.e., behind the pole, at the end of spindle elongation (N = 44 out of 1127 polar kinetochore
675 pairs from 101 cells). These results suggest that the pivoting mechanism is highly efficient in
676 U2OS cells and facilitates successful congression of most polar kinetochores. Tracking of
677 kinetochores that remained unaligned revealed that they eventually moved to the main spindle
678 surface (Supplementary Figure 7C), likely through capture by microtubules from the opposite
679 spindle half. However, this elongation-independent movement was significantly delayed, as
680 indicated by a threefold increase in mitotic duration in cells retaining an unaligned chromosome
681 after spindle elongation (Figure 8E). Thus, failure of timely polar chromosome transit during
682 spindle elongation prolongs mitosis in a cancer cell line.

683 According to our model, slower spindle elongation should delay the incorporation of
684 polar chromosomes into the spindle body, whereas enhanced elongation should promote it. To
685 test this prediction, we perturbed spindle elongation in two highly chromosomally unstable
686 cancer cell lines, OVSAHO (ovarian carcinoma) and MDA-MB-231 (triple-negative breast
687 cancer), both characterized by congression defects (Tamura et al., 2020; Tucker et al., 2023)
688 (Supplementary Figure 7D). We used low-dose monastrol to slow spindle elongation and
689 KIF4A depletion to enhance it (Jagrić et al., 2021) (Figure 8F, Supplementary Figure 7E-G,
690 Video 11 and 12). Monastrol concentrations were titrated in each line to reduce spindle
691 elongation post-NEBD without inducing monopolar arrest in most cells (Methods). Live-cell
692 imaging confirmed that monastrol-treated spindles were shorter and KIF4A-depleted spindles
693 were longer than untreated ones throughout early mitosis in OVSAHO and MDA-MB-231 cells
694 (Figure 8G). The duration of polar chromosome transit, defined as the time when the last polar
695 chromosome moved from the rear to the front side of the spindle pole, was inversely correlated
696 with spindle length in early prometaphase in both cell lines (Figure 8H), in agreement with our
697 model.

698 To extend our findings to larger cell populations, we analyzed fixed, immunostained
699 metaphase cells treated with either KIF4A siRNA to increase spindle length or low-dose
700 nocodazole (10 ng/mL) to reduce spindle length (Supplementary Figure 7H). Nocodazole was
701 selected over monastrol for the fixed-cell assay, as monastrol-treated spindles reached near-
702 normal length by metaphase (Figure 8G). In addition to OVSAHO and MDA-MB-231, we
703 analyzed the Caco-2 cell line (colorectal adenocarcinoma) (Thompson and Compton, 2008).
704 These experiments revealed an overall trend where cells with longer spindles had fewer polar
705 chromosomes than those with shorter spindles (Supplementary Figure 7I). In OVSAHO cells,
706 KIF4A depletion increased spindle length from 11.16 ± 0.09 μm (N = 319) to 12.74 ± 0.15 μm
707 (N = 157), and this was associated with a fourfold reduction in the fraction of cells harboring
708 polar chromosomes (from 13.2 ± 2.1% to 3.2 ± 1.4%) (Figure 8I-K). The distance of polar
709 chromosomes from the nearest pole was comparable between untreated and KIF4A-depleted
710 cells (Supplementary Figure 7J), indicating that polar ejection forces (Chong et al., 2024;
711 Novais-Cruz et al., 2023) were not significantly altered. Conversely, nocodazole treatment
712 shortened spindle length and increased the number of polar chromosomes relative to controls
713 (Supplementary Figure 7I), likely due to both spindle shortening and microtubule stabilization
714 (Rajendraprasad et al., 2021). MDA-MB-231 and Caco-2 cells exhibited changes in the same
715 direction as OVSAHO following KIF4A depletion and nocodazole treatment, though the effect
716 of Kif4A was not statistically significant (Supplementary Figure 7I).

717 In conclusion, our results demonstrate that the spindle elongation-driven pivoting
718 model applies across multiple cancer cell lines and plays a key role in ensuring rapid mitosis.
719 Treatments that reduce spindle elongation impair the resolution of polar chromosomes,
720 whereas enhanced elongation facilitates their timely incorporation into the spindle.

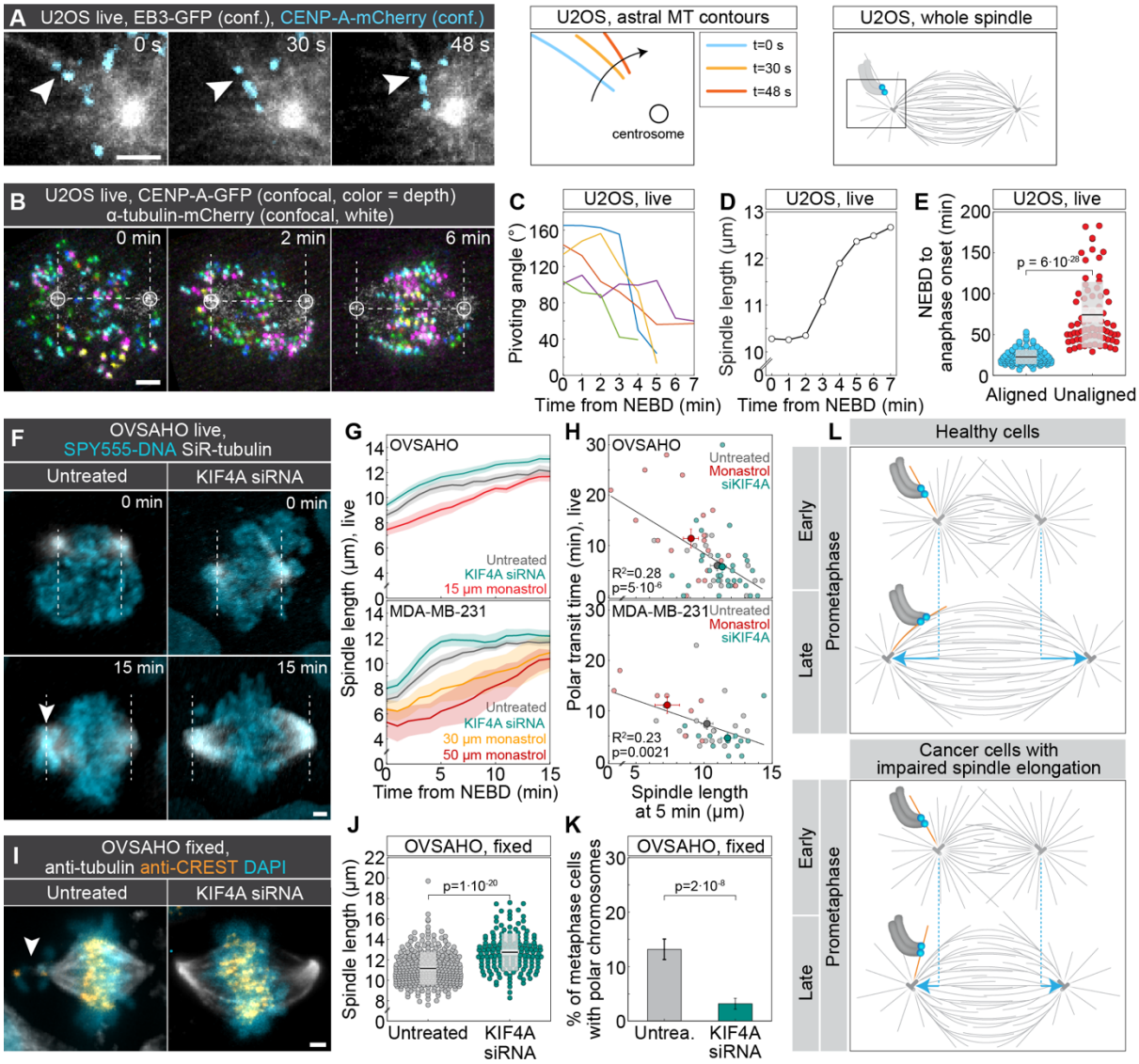

721

722

723 **Figure 8. Spindle elongation promotes chromosome alignment in cancer cell lines.**

724 **(A)** Time-lapse confocal images of live U2OS cells stably expressing EB3-GFP (white,
725 confocal) and CENP-A-mCherry (blue, confocal) showing astral microtubule attached to the
726 polar kinetochore pair and pivoting over time. Images are temporal maximum intensity
727 projections of a single z-plane in 3-5 sequential time frames during which the EB3 spot was
728 visible. Astral microtubule contours during the pivoting are shown to the right, and a scheme
729 showing the imaged region within the spindle is at the far right. (**B**) Time-lapse confocal images
730 of live U2OS cells stably expressing CENP-A-GFP (colored for depth) and tubulin mCherry
731 (white). Circles mark the poles and dashed lines the spindle axis and the edge of the polar
732 region. (**C-D**) Pivoting angle for 5 polar kinetochore pairs (C) and spindle length (D) over time
733 for the cell shown in (B). (**E**) Univariate scatter plot of the time from NEBD until anaphase
734 onset in live U2OS cells as in (B), comparing cells with aligned chromosomes (left, N = 111)
735 and those that had one or more chromosomes that were not aligned (right, N = 73) at the end
736 of spindle elongation. Statistical test: t-test. **(F)** Time-lapse images of control (left) and Kif4A
737 siRNA-treated (right) live OVSAHO cells stained with SPY-555-DNA (blue) and SiR-tubulin

738 (white), imaged using lattice light-sheet microscopy. Dashed lines denote the edge of the polar
739 regions; arrowhead points to chromosomes near the pole. **(G)** Spindle length over time for
740 OVSAHO (top; N = 19, 22, 20 cells for the indicated treatments) and MDA-MB-231 cells
741 (bottom; N= 18, 22, 5, 3 cells for the indicated treatments) treated as stated in the legend. Lines,
742 mean; shaded areas, SEM. (**H**) Polar transit time for OVASHO (top) and MDA-MB-231 cells
743 (bottom) as a function of the spindle length measured 5 minutes after NEBD. Small circles
744 show individual cells, and large circles with error bars are mean and SEM for each treatment.
745 Linear regression on individual data points is also shown. **(I)** Images of fixed OVSAHO cells,
746 control (left) and KIF4A siRNA-treated (right), stained with anti-α-tubulin antibody (white),
747 anti-CREST (orange), and DAPI (blue). The white arrow marks a chromosome at the pole in
748 metaphase. **(J)** Univariate scatter plot of the spindle length in untreated (N = 319) and KIF4A
749 siRNA-treated (N = 157) fixed OVSAHO cells. Statistical test: t-test. (**K**) Percentage of
750 metaphase cells with polar chromosomes in untreated and KIF4A siRNA-treated fixed
751 OVSAHO cells from (J). Statistical test: Chi-squared test. In (B), (F), and (I), images are
752 maximum intensity projections of the whole cell. All scale bars, 2 µm. **(L)** A model of how
753 polar chromosomes pass across the pole in normal cells and fail to cross the pole when spindle
754 elongation is impaired, such as in certain cancer cells. In healthy cells, polar chromosomes are
755 attached to astral microtubules. While the chromosomes remain largely immobile, the spindle
756 elongates, thereby driving the pivoting of astral microtubules around the spindle pole.
757 Consequently, the chromosomes with their microtubules get close to the main spindle surface,
758 where they attach and move to the spindle midplane. In cells with impaired spindle elongation,
759 this elongation is insufficient to drive microtubule pivoting from the back of the spindle pole
760 all the way towards the main spindle surface, leaving polar chromosomes persistently
761 unaligned.

762

763 **Discussion**

764 **The pivoting model**

765 Our study uncovers an essential step in chromosome congression that safeguards genome
766 integrity by rescuing polar chromosomes, which are at the highest risk of missegregation
767 (Klaasen et al., 2022), from the "danger zone" behind the spindle pole. During early
768 prometaphase, once the centripetal movement of chromosomes ends, the spindle begins to
769 elongate (Magidson et al., 2011). During this phase, the poles push outward, moving beyond
770 the polar chromosomes, which are relatively stationary. As the chromosomes remain attached
771 to astral microtubules throughout his process, these microtubules passively pivot around the
772 spindle pole from the outer to the inner spindle region, ultimately reaching the spindle surface
773 and enabling the interaction of polar chromosomes with it and subsequent congression (Figure
774 8L).

775 Our findings indicate that, once the centripetal chromosome movement ends, polar
776 chromosomes usually remain attached to the same microtubule bundle extending from the
777 centrosome until approaching the spindle surface. If the microtubules were to extend at a

constant angle from the centrosome without the ability to pivot, the chromosome would move along with the centrosome, away from the spindle center. However, instead of moving, the chromosome remains stationary, and it is the angle of the microtubules that changes, repositioning the chromosome from behind the centrosome to its front side where it can congress to the spindle midplane. Taking an evolutionary perspective, since a similar type of microtubule rotational movement has been observed in yeast (Kalinina et al., 2013), it will be valuable to assess how conserved microtubule pivoting, its underlying mechanisms, and functions are across various species.

The mechanism we propose relies on a biomechanical property of the microtubule-centrosome connection that enables the microtubules to pivot under force. Given that the pericentriolar material anchors the microtubules at the centrosome (Woodruff et al., 2014), it will be interesting to explore how mechanical properties of the pericentriolar material affect microtubule pivoting and, in turn, the rescue of polar chromosomes. Remarkably, the old and the young centrosomes behave differently in mitosis and the old one retains more unaligned chromosomes (Gasic et al., 2015). It may be that microtubule pivoting is different on the old and young centrosome and that this leads to a bias in chromosome alignment errors.

The role of microtubule pivoting in spindle assembly

The pivoting of microtubules attached to polar chromosomes may play a role in spindle assembly. We found that typical polar chromosomes arrive at the spindle surface with mono-lateral attachments. The microtubules in the “mono” part of the attachment may represent an early kinetochore fiber, which, upon chromosome arrival to the spindle surface, becomes incorporated into the growing spindle. Thus, kinetochore fibers of polar chromosomes may start to form already when the chromosome is behind the pole, which is much earlier than previously thought and can explain the observed fast chromosome biorientation occurring as soon as the chromosome interacts with the spindle surface (Renda et al., 2022; Vukušić and Tolić, 2024).

We propose that microtubules laterally attached to the polar chromosome also integrate into the spindle, forming antiparallel overlaps with microtubules extending from the opposite side. This antiparallel bundle likely facilitates the formation of end-on attachments on the sister kinetochore facing the further pole by guiding the growth of new microtubules towards this kinetochore. As end-on attachments of both sister kinetochores mature and lateral attachments diminish (Magidson et al., 2011), the previously laterally attached microtubules may turn into bridging fibers that connect sister kinetochore fibers (Kajtez et al., 2016; Simunić and Tolić, 2016). Thus, polar chromosomes bring along components of their fibers to the growing spindle.

The role of spindle elongation in maintaining genomic stability

Our findings show that incomplete or slow spindle elongation, accompanied by reduced microtubule pivoting, can lead to chromosome missegregation due to the delayed or

817 unsuccessful arrival of polar chromosomes to the spindle surface. Previous work has shown
818 that HeLa cells following the prophase pathway of spindle assembly, where centrosomes
819 quickly separate to the opposite sides of the nucleus before NEBD, exhibit fewer chromosome
820 segregation errors than those following the prometaphase pathway, where centrosome
821 separation is slower and continues during prometaphase (Kaseda et al., 2011). Our model
822 suggests that the differences in segregation errors between the two pathways arise from the
823 presence of polar chromosomes (Vukušić and Tolić, 2022). In the prophase pathway, rapid
824 spindle elongation ensures that no chromosomes are left behind the pole at NEBD, resulting in
825 error-free segregation. In contrast, the slower centrosome separation in the prometaphase
826 pathway leads to the presence of polar chromosomes, whose delayed arrival at the metaphase
827 plate may increase the likelihood of segregation errors.

828 The spatial arrangement of chromosomes and centrosomes at the start of mitosis may
829 explain why certain chromosomes are more prone to missegregation (Klaasen et al., 2022). As
830 the chromosomes that are found behind the spindle pole in early mitosis are typically positioned
831 at the nuclear periphery during the preceding interphase (Klaasen et al., 2022), our proposed
832 model identifies the biomechanical principles underlying the biased missegregation of
833 peripheral chromosomes.

834 In the context of disease, we demonstrate that insufficient spindle elongation, leading
835 to impaired microtubule pivoting, delays the alignment of polar chromosomes in several cancer
836 cell lines. Conversely, enhancing spindle elongation accelerates polar chromosome alignment.
837 However, additional mechanisms may contribute to efficient chromosome alignment. For
838 instance, in cell lines with short spindles but minimal accumulation of polar chromosomes,
839 such as the ovarian cancer cell line OVKATE (Risteski et al., 2024; Tamura et al., 2020),
840 pulling forces exerted by microtubules from the opposite spindle half may facilitate the
841 integration of polar chromosomes into the spindle. The relative contribution of these alternative
842 mechanisms across different cell lines and over time remains an interesting question for future
843 investigation. We further propose that the failure of polar chromosomes to cross the pole during
844 spindle elongation, observed in a subset of cancer cells and after nocodazole treatment, may be
845 linked to increased stabilization of end-on attached microtubules (Bakhoum et al., 2009;
846 Rajendraprasad et al., 2021; Vasquez et al., 1997), giving rise to thick microtubule bundles
847 with limited pivoting capacity. The resulting delay in the movement of polar chromosomes
848 may contribute to prolonged mitosis in cancer cell lines with chromosome congression defects.

849 We speculate that the spindle elongation-driven microtubule pivoting may be relevant
850 to explain and modify errors in chromosome alignment in cancer cells. This idea is supported
851 by the fact that cells without PTEN, the second most frequently mutated tumor suppressor after
852 p53 (Li et al., 1997; Turnham et al., 2020; Yin and Shen, 2008), recruit less Eg5 to their
853 spindles, resulting in both shorter spindles and misaligned chromosomes (He et al., 2016).
854 Thus, a PTEN mutation might be one of the indicators that a particular type of cancer has
855 unaligned chromosomes that stem from impaired spindle elongation and might be rescued by
856 restoring PTEN function. More broadly, we propose that manipulating spindle elongation in
857 certain cancer cells could be used to influence mitotic errors, either correcting them to maintain
858 genome stability or worsening them to a degree that compromises cell viability.

Materials & Methods

Cell lines and plasmids

The experiments were performed using the following cell lines: human hTERT-RPE1 (hTERT-immortalized retinal pigment epithelium) cells stably expressing CENP-A-GFP, human hTERT-RPE1 (hTERT-immortalized retinal pigment epithelium) cells stably expressing CENP-A-GFP and Centrin1-GFP (Magidson et al., 2011), and human hTERT-RPE1 cells stably expressing CENP-A-GFP and Mis12-mCherry, a gift from Alexey Khodjakov (Wadsworth Center, New York State Department of Health, Albany, NY, USA); human hTERT-RPE1 cells stably expressing CENP-A-Cerulean and Mad2-mRuby (Marcozzi and Pines, 2018), a gift from Jonathon Pines (Institute of Cancer Research, London, UK); human hTERT-RPE1 cells stably expressing tubulin-EYFP and H2B-mRFP (Holland et al., 2012), a gift from Andrew Holland (Johns Hopkins University School of Medicine, Baltimore, MD, USA); human hTERT-RPE1 cells stably expressing dCas9-GFP-3xFKBP (Truong et al., 2023), a gift from Susanne Lens (Utrecht University, Utrecht, Netherlands); human hTERT-RPE1 cells stably expressing EB3-GFP and H2B-RFP, a gift from Patrick Meraldi (University of Geneva) and generated by Will Krek; unlabeled human OVSAHO cell line (JCRB1046 Cell Bank, Tebubio, Le Perray-en-Yvelines, France); unlabeled human MDA-MB-231 cell line, a gift from Dragomira Majhen (Ruđer Bošković Institute, Zagreb, Croatia); unlabeled human Caco-2 cell line (86010202, Sigma Aldrich); and human U2OS cells stably expressing EB3-2xGFP and CENP-A-mCherry (Kajtez et al., 2016).

The plasmids used for the experiments were: pHTN HaloTag-CENP-A (Castrogiovanni et al., 2022), a gift from Patrick Meraldi (University of Geneva, Geneva, Switzerland); psPAX2 (Addgene, No. 12260); psMD2.G (Addgene, No. 12259); pLH sgRNA Chr1-telo (Dumont et al., 2020) and pLH sgRNA Chr9-cen (Truong et al., 2023), both gifts from Susanne Lens (Utrecht University, Utrecht, Netherlands).

Cell culture

All cell lines, except an OVSAHO cell line, were cultured in Dulbecco's Modified Eagle's Medium (DMEM) containing 1 g/L D-glucose, pyruvate and L-glutamine (Gibco), supplemented with 10% (vol/vol) heat-inactivated Fetal Bovine Serum (FBS, Sigma Aldrich, St. Louis, MO, USA) and penicillin (100 IU/mL)/streptomycin (100 mg/mL) solution (Lonza, Basel, Switzerland). The OVSAHO cell line was maintained in RPMI 1640 medium containing L-glutamine and sodium bicarbonate (Sigma-Aldrich, St. Louis, MO, USA), complemented with the same supplements used in the previously described DMEM medium. All cells were kept at 37 °C and 5% CO2 in a Galaxy 170 R humidified incubator (Eppendorf, Hamburg, Germany). All cell lines have been routinely examined for mycoplasma contamination by using SPY-555-DNA (1:100 000, Spirochrome, Stein am Rhein, Switzerland) and by checking if any extracellular DNA is present. All cell lines used for experiments have been confirmed to be mycoplasma free.

898 **RNAi treatment**

899 Cells for RNAi transfection were seeded on 35 mm uncoated dishes with the 0.17 mm (1.5
900 coverslip) glass thickness (Ibidi GmbH, Gräfeling, Germany) in 1 mL of the previously
901 described DMEM medium to reach approximately 60% confluence the following day. siRNA
902 constructs were diluted in OPTI-MEM medium (Life Technologies, Waltham, MA, US) and
903 RNAi treatments were performed using Lipofectamine RNAiMAX Reagent (Life
904 Technologies, Waltham, MA, US) according to the instructions provided by the manufacturer.

905 The siRNA constructs and their final concentrations were: 100 nM CENP-E siRNA (L-003252-
906 000010; Dharmacon, Lafayette, CO, USA), 100 nM Spindly/CCDC99 siRNA (L-016970-00-
907 0010, Dharmacon, Lafayette, CO, USA), 100 nM KIF4A siRNA (sc-60888; Santa Cruz
908 Biotechnology, Dallas, TX, USA), 100 nM Kid/KIF22 siRNA (4392420; Ambion, Austin, TX,
909 USA). Cells were incubated for four hours with the transfection mixture followed by medium
910 replacement into the previously described DMEM medium. All experiments were performed
911 24 hours after siRNA transfection.

912 **Plasmid transfection**

913 To transiently express CENP-A in an RPE1 cell line stably expressing tubulin-EYFP and H2B-
914 mRFP, 5 µg of pHTN HaloTag-CENP-A plasmid was used for transfection performed on
915 Nucleofector Kit R with the Nucleofector 2b Device (Lonza) following manufacturer's
916 instructions. The Nucleofactor Y-001 program was used for the transfection of the RPE1 cell
917 line. After transfection, around 500 000 cells were seeded on 35 mm uncoated dishes with the
918 0.17 mm (1.5 coverslip) glass thickness (Ibidi GmbH, Gräfeling, Germany) in 1 mL of the
919 previously described DMEM medium. Transfection was performed 48 hours before imaging.

920 **Lentivirus transduction and cell line generation**

921 To produce lentiviruses, HEK293T cells were seeded on 10 cm Petri dishes to reach 80%
922 confluence the next day. Plasmid constructs were diluted in OPTI-MEM medium (Life
923 Technologies, Waltham, MA, US) and transfections were performed using Lipofectamine 3000
924 Transfection Reagent (Life Technologies, Waltham, MA, US) according to the manufacturer's
925 protocol. The plasmid constructs and their final masses were as follows: 10 µg of psPAX2, 5
926 µg of psMD2.G, 15 µg of pLH sgRNA Chr1-telo or 15 µg of pLH sgRNA Chr9-cen. The cell
927 medium was replaced with the previously described DMEM medium 24 hours after
928 transfection. Lentiviruses containing sgRNA for Chr1-telo or Chr9-cen were harvested 48
929 hours after transfection by filtering the cell medium through 45 µm filters (No. 99745, TPP,
930 Switzerland). RPE1 cells stably expressing dCas9-GFP-3xFKBP were seeded in 6 well plates
931 (120 000 cells/well, Thermo Fisher Scientific, Waltham, MA, USA) the day before lentivirus
932 transduction. Lentiviruses were added to cells together with 6 µg/ml of polybrene (TR-1003-
933 G, Merck Milipore, Darmstadt, Germany) and incubated for 24 hours.

934 **Treatments with inhibitors**

935 The following Eg5 inhibitors were used on a "one cell per dish" principle: STLC (final
936 concentration 40 µM, 164739, Sigma-Aldrich, St. Louis, MO, USA) was added approximately

937 30 s before landing to cause spindle shortening; FCPT (final concentration 40 μM, a gift from
938 Timothy Mitchison) was added at the end of centripetal approaching to block the spindle
939 elongation; monastrol (final concentration 100 μM in RPE1 cells, HY-101071A,
940 MedChemExpress, Monmouth Junction, USA) was added 30 s before landing and then washed
941 out with a pre-warmed DMEM medium when spindle stopped shortening. Nocodazole (final
942 concentration 20 nM in RPE1 cells, HY-13520, MedChemExpress, Monmouth Junction,
943 USA), Mps1 inhibitor AZ3146 (final concentration 3 μM, HY-14710, MedChemExpress,
944 Monmouth Junction, USA), Mps1 inhibitor Cpd-5 (final concentration 62.5 nM, a gift from R.
945 Medema via G. J. P. L. Kops lab; (Klaasen et al., 2022; Koch et al., 2016)) and actin
946 polymerization inhibitor latrunculin A (final concentration 2 μM, 428021, Sigma-Aldrich, St.
947 Louis, MO, USA) were added approximately 45 minutes prior to imaging and cells within the
948 dish were subsequently imaged for 4 hours. CENP-E inhibitor GSK923295
949 (MedChemExpress, Monmouth Junction, USA, IC50 value 3.2 nM) was added at a final
950 concentration of 80 nM 1-4 hours before imaging.

951 For live-cell imaging of monastrol-treated OVSAHO cells, 15 μM monastrol was
952 chosen as it was sufficient to produce slower spindle elongation without inducing monopolar
953 arrest in the majority of cells. In MDA-MB-231 cells, 30 and 50 μM monastrol produced a
954 similar result. Only the cells that formed a bipolar spindle within the first ten minutes after
955 NEBD were analyzed. For fixed-cell imaging of nocodazole-treated cancer cells, 10 ng/mL
956 (~33 nM) of nocodazole was added 2 hours prior to fixation.

957 **Live-cell dyes**

958 To identify nuclear envelope breakdown in RPE1 cells stably expressing CENP-A-GFP and
959 Centrin1-GFP, the SPY-555 or SPY-595 DNA probe (1: 100 000, Spirochrome, Stein am
960 Rhein, Switzerland) was added to the cells 45 minutes to 2 hours prior to imaging. When
961 microtubules were visualized during live-cell imaging in the same cell line, the SPY-650-
962 tubulin probe (1:50 000, Spirochrome, Stein am Rhein, Switzerland) was added to the cells 45
963 minutes to 2 hours prior to imaging. For the live-cell imaging of OVSAHO, MDA-MB-231,
964 and Caco-2 cell lines, the SPY-555 DNA probe (1: 50 000, Spirochrome, Stein am Rhein,
965 Switzerland) was added to the cells along with the SiR-tubulin probe (50 nM, Spirochrome,
966 Stein am Rhein, Switzerland; (Lukinavičius et al., 2014)) 45 minutes prior to imaging. The
967 cells were subsequently imaged for 1-3 hours. For STED live-cell imaging, the SiR-tubulin
968 probe (100 nM, Spirochrome, Stein am Rhein, Switzerland; (Lukinavičius et al., 2014)) was
969 added to the cells 15 minutes prior to imaging and cells were subsequently imaged for 45
970 minutes. To avoid efflux of the dyes, a broad-spectrum efflux pump inhibitor verapamil
971 (Spirochrome, Stein am Rhein, Switzerland) was added at a final concentration of 1 μM to cells
972 along with tubulin and/or DNA probes. For the live-cell imaging of RPE1 cells stably
973 expressing EYFP-α-tubulin and H2B-mRFP, cells were incubated for 30 minutes with Janelia
974 Fluor 635 HaloTag ligand (a final concentration of 20 nM, Promega, Madison, WI, USA) 24
975 hours before imaging to visualize the transiently expressed CENP-A-HaloTag.

976 **Immunofluorescence**

977 To determine the RNAi efficiency, RPE1 cells stably expressing CENP-A-GFP and Centrin1-
978 GFP were grown on 35 mm uncoated dishes with the 0.17 mm (1.5 coverslip) glass thickness
979 (Ibidi GmbH, Gräfeling, Germany) and fixed by 1 ml of ice-cold methanol for 1 minute at –20
980 °C, except for Spindly/CCD99 immunostaining where cells were pre-extracted with 0,2%
981 Triton in PHEM buffer (60 mM PIPES, 10 mM EGTA, 25 mM HEPES, 4 mM MgCl2) for 1
982 minute and subsequently fixed with 4% pre-warmed to 37 ºC for 10 minutes. Cells for CENP-
983 E and ZW10 immunostainings were pre-extracted for 20 s with 0.5% Triton in PEM buffer
984 (0.1M PIPES, 1mM EGTA, 1mM MgCl2) followed by fixation by 1 ml of ice-cold methanol
985 for 1 minute. Following fixation, cells were washed three times for 5 minutes with 1 ml of PBS
986 and permeabilized with 0.5% Triton-X-100 in PBS for 15 minutes at room temperature. To
987 block unspecific binding, cells were incubated in 1 ml of blocking buffer (1% normal goat
988 serum (NGS)) for 1 hour at 4 °C. Cells were then washed three times for 5 minutes with 1 ml
989 of PBS and incubated with 250 µl of primary antibody solution overnight at 4 °C. The primary
990 antibodies were used as follows: rabbit anti-CENP-E (1:100 for determination of RNAi
991 efficiency, and 1:500 for staining of outer corona, C7488; Sigma-Aldrich), rabbit anti-
992 Spindly/CCD99 (1:1000, A301_354A, Bethyl), mouse anti-KIF4A (1:100, sc-365144; Santa
993 Cruz Biotechnology), mouse anti-Kid (1:100, sc-390640; Santa Cruz Biotechnology), rabbit
994 polyclonal anti-ZW10 (1:500, ab21582, Abcam), rabbit polyclonal anti-MAD2 (1:250,
995 924601, BioLegend), mouse monoclonal anti-Astrin, clone C-1 (1:250, MABN2487, Merck).
996 After the incubation with a primary antibody, cells were washed three times for 5 minutes with
997 1 ml of PBS and then incubated with 250 µl of secondary antibody for 1 hour at room
998 temperature. Alexa Fluor 594 (Abcam, ab150108 or ab150076) was used as a secondary
999 antibody at a 1:250 dilution for CENP-E, Kif4A, and Kid staining and at a 1:1000 dilution for
1000 Spindly staining in experiments where RNAi efficiency was tested. Alexa Fluor 647 (Abcam,
1001 ab150107) was used as a secondary antibody at a 1:500 dilution for Astrin staining. Alexa Fluor
1002 594 was used as a secondary antibody at a 1:500 dilution for staining of CENP-E and Mad2 on
1003 polar kinetochores. Alexa Fluor 647 (Abcam, ab150075) was used as a secondary antibody at
1004 a 1:1000 dilution for ZW10 staining.

1005 To image polar chromosomes in cancer cell lines OVSAHO, MDA-MB-231, and Caco-
1006 2, cells were fixed with 1 ml of 4% paraformaldehyde pre-warmed to 37 ºC for 10 minutes
1007 followed by all the previously described steps for immunostaining. The primary antibodies
1008 were used as follows: rat anti-tubulin (1:500, MA1-80017, Invitrogen) and human anti-
1009 centromere protein (1:300, 15-234, Antibodies Incorporated, CA, USA). The secondary
1010 antibodies were: donkey anti-rat Alexa Fluor 488 (1:1000, Abcam, ab150153) and goat anti-
1011 human DyLight 594 (1:500, Abcam, ab96909). DAPI (1 µg/mL) was used for chromosome
1012 visualization in all cell lines.

1013 For STED imaging, RPE1 cells stably expressing CENP-A-GFP and RPE1 cells stably
1014 expressing CENP-A-Cerulean and Mad2-mRuby were grown on 35 mm uncoated dishes with
1015 the 0.17 mm (1.5 coverslip) glass thickness (Ibidi GmbH, Gräfeling, Germany). Cell medium
1016 was removed and 0.5% Triton in PEM buffer (0.1M PIPES, 1mM EGTA, 1mM MgCl2) was
1017 added for 15 seconds to remove the components of the cytoplasm. Following extraction, cells
1018 were fixed in 3% paraformaldehyde and 0.1% glutaraldehyde solution for 10 minutes. To

1019 reduce the background fluorescence, quenching (100 mM glycine in PBS) and reduction (0.1%
1020 sodium borohydride in PBS) solutions were added for 7 and 10 minutes, respectively. To
1021 prevent non-specific binding, cells were incubated in blocking/permeabilization buffer (2%
1022 NGS and 0.5% Triton-X-100 in PBS) for 2 hours at 4 °C. Microtubules were then stained using
1023 the rat anti-tubulin primary antibody (1:500 in blocking/permeabilization buffer, MA1-80017,
1024 Invitrogen) with a 4 °C overnight incubation. The next day, cells were washed with PBS three
1025 times for 5 minutes. After washing, the secondary antibody donkey anti-rat Alexa Fluor 594
1026 (1:1000 in blocking/permeabilization buffer, Abcam, ab150156) or donkey anti-rat Alexa Fluor
1027 647 (1:1000 in blocking/permeabilization buffer, Abcam, ab150155) was added and incubated
1028 for 1 hour at room temperature. DAPI (1 µg/mL) or SPY-505-DNA (1:10 000, Spirochrome,
1029 Stein am Rhein, Switzerland) was added to visualize chromosomes. The protocol was
1030 originally modified for (Štimac et al., 2022) based on the protocols from (Ponjavić et al., 2021;
1031 Zhang et al., 2020). For validation of actin depolymerization by Latrunculin A, RPE1 cells
1032 stably expressing CENP-A-GFP and Centrin1-GFP were fixed following the same fixation
1033 protocol as above, and SiR-actin (200 nM in PBS, Spirochrome, Stein am Rhein, Switzerland)
1034 was incubated for 20 min at room temperature.

1035 To analyze the position of chromosomes 1 and 9 in interphase cells, RPE1 cells stably
1036 expressing Chr1-telo-GFP or Chr9-cen-GFP were stained for tubulin and centrin-3 following
1037 the same immunostaining protocol used for STED imaging. Rabbit anti-centrin-3 primary
1038 antibody (1:1000, ab228690, Abcam) and secondary donkey anti-rabbit Alexa Fluor 647
1039 (1:1000, Abcam, ab150075) were used for immunostaining.

1040 **Microscopy**

1041 STED microscopy of fixed cells, live-cell imaging of pivoting microtubules, live-cell imaging
1042 of EB3 comets and live-cell imaging of cells treated with Cpd-5 were performed using an
1043 Expert Line easy3D STED microscope system (Abberior Instruments, Göttingen, Germany)
1044 with the 100 x/1.4NA UPLSAPO100x oil objective (Olympus, Tokio, Japan) and an avalanche
1045 photodiode (APD) detector, as previously described (Koprivec et al., 2025). The 405 nm, 488
1046 nm, 561 nm and 647 nm laser lines were used for the excitation of Cerulean, GFP, Alexa Fluor
1047 594/mRuby/mCherry and Alexa Fluor 647/Janelia Fluor 635/SiR-tubulin, respectively. The
1048 775 nm laser line was used for the depletion of red and far-red lines during the STED
1049 superresolution imaging. Images were acquired using the Imspector software. The xy pixel size
1050 for fixed RPE1 cells stably expressing CENP-A-GFP was 20 nm and 20-30 focal planes were
1051 acquired with the 300 nm distance between them to cover the whole cell. The xy pixel size for
1052 fixed RPE1 cells stably expressing CENP-A-Cerulean and Mad2-mRuby was 25 nm and 1
1053 focal plane containing the kinetochores of polar chromosomes was acquired. For live-cell
1054 STED imaging of pivoting microtubules, the xy pixel size was set to 30 nm and one focal plane
1055 was acquired every 60 seconds. For confocal live-cell imaging of pivoting microtubules in
1056 RPE1 cells on the same microscope, the xy pixel size was set to 55 nm and 3 focal planes were
1057 acquired, with the 1 µm distance between the planes and 15 seconds time intervals between
1058 different time frames. For confocal live-cell imaging of EB3 comets in RPE1 cells, the xy pixel
1059 size was set to 80 nm and 3 focal planes were acquired, with the 1 µm distance between the
1060 planes and 20 seconds time intervals between different time frames. For confocal live-cell

imaging of EB3 comets in U2OS cells, the xy pixel size was set to 80 nm and one focal planes was acquired, with 1 second time intervals between different time frames. For confocal live-cell imaging of cells treated with Cpd-5, the 488 nm laser line was used to excite the GFP, the 647 nm laser line was used to excite the SPY-650-tubulin, the xy pixel size was 80 nm and 6-7 focal planes were acquired, with 1 µm distance between the planes and 20 seconds time intervals between different time frames, as previously described (Klaasen et al., 2022). Movies of U2OS cells expressing CENP-A-GFP and tubulin-mCherry were acquired as previously described (Klaasen et al., 2022).

Confocal microscopy of OVSAHO cells and RPE1 cells immunostained to check the respective RNAi efficiencies was performed using a previously described microscope setup (Buđa et al., 2017), consisting of a Bruker Opterra Multipoint Scanning Confocal Microscope (Bruker Nano Surfaces, Middleton, WI, USA), mounted on a Nikon Ti-E inverted microscope with a Nikon CFI Plan Apo VC 100 x/1.4 numerical aperture oil objective (Nikon, Tokyo, Japan). To excite DAPI, GFP, Alexa Fluor 594 or DyLight 594, a 405 nm, 488 nm and 561 nm laser lines were used, respectively. Opterra Dichroic and Barrier Filter Set 405/488/561 enabled the separation of excitation light from the emitted fluorescence. Images were acquired using the Evolve 512 Delta Electron Multiplying Charge Coupled Device (EMCCD) Camera (Photometrics, Tuscon, AZ, USA), with a camera readout mode of 20 MHz. The xy pixel size was 83 nm and the slit aperture was 22 µm. In all experiments, the whole spindle stack was imaged. The z-stacks were acquired using the unidirectional xyz scan mode with the 1 µm distance between the planes to cover the entire cell.

Confocal live cell imaging of RPE1 cells stably expressing CENP-A-GFP and Centrin1-GFP treated with STLC, FCPT, monastrol and AZ3146 was performed on a Dragonfly spinning disk confocal microscope system (Andor Technology, Belfast, UK) using the 100x/1.47 HC PL APO oil objective (Nikon, Tokyo, Japan) and Sona 4.2B-6 Back-illuminated sCMOS camera (acquisition mode set to high speed, Andor Technology) linked with iXon Life 888 EMCCD Camera (EM gain set to 208, Andor Technology). To simultaneously image two channels on two independent cameras, the 565 LP image splitter was used. Images were acquired using the Fusion software. During imaging, cells were maintained at 37°C and 5% CO2 within the heating chamber (Okolab, Pozzuoli, NA, Italy). For the excitation of GFP and SPY-650-tubulin, the 488-nm and 637-nm laser lines with corresponding filters were used, respectively. Image acquisition was done every 0.4 µm with 21 focal planes and a time interval of 10 seconds.

The Lattice Lightsheet 7 system (Carl Zeiss, Germany) was used for the live cell imaging of control RPE1 cells expressing CENP-A-GFP and Centrin1-GFP and for the imaging of cells with CENP-E, Spindly/CCD99 and Kid/KIF4A depletion, inhibition of actin polymerization or nocodazole addition. The same system was used for live-cell imaging of cancer cell lines. The system includes an illumination objective lens 13.3×/0.4 (at a 30° angle to cover the glass) with a static phase element and a detection objective lens 44.83×/1.0 (at a 60° angle to cover the glass) with an Alvarez manipulator, as previously described (Vukušić and Tolić, 2024). For the live-cell imaging of RPE1 cells, the GFP was excited using the 488-nm diode laser (power output 10 Mw), with the laser power set to 2.5%, LBF 405/488/561/642

1103 emission filter and 12 ms exposure time. The detection module consisted of a Hamamatsu
1104 ORCA-Fusion sCMOS camera. The width of the imaging area was set to 32-36 µm with the x
1105 interval of 0.3 µm. Images were acquired every 6 seconds. For the live-cell imaging of cancer
1106 cell lines, the SPY-555-DNA was excited using the 561-nm diode laser, with the laser power
1107 set to 2.0-4.0%. SiR-tubulin was excited using the 561-nm diode laser, with the laser power set
1108 to 1.0-1.5%. The exposure time was 15-20 ms. The width of the imaging area was set to 36 µm
1109 with the x interval of 0.5 µm. Images were acquired every minute. During the imaging, cells
1110 were kept at 37 °C and at 5% CO2 in a Zeiss stage incubation chamber system (Carl Zeiss,
1111 Germany). All movies were deskewed with the ZEN 3.7 software using the „Linear
1112 Interpolation“ and „Cover Glass Transformation“ settings. Deconvolution was performed
1113 using the „Constrained Iterative“ algorithm with automatic normalization and strength set to
1114 4.0. The imaging parameters for CENP-E inhibition experiments were described previously
1115 (Vukušić and Tolić, 2024).

1116 Confocal imaging of chromosomes 1 and 9 in RPE1 cells was performed on the
1117 Airyscan Zeiss LSM800 confocal laser scanning microscope with the 40x/0.95 Corr M27
1118 objective (Carl Zeiss, Germany) and LSM 800 camera. To excite DAPI, GFP, Alexa Fluor 594
1119 and 647, the 405 nm, 488 nm, 561 nm and 647 nm laser lines were used, respectively. Images
1120 were acquired in ZEN blue 3.5 software using the Tiles recording mode, with the 0.5 µm
1121 distance between the planes to cover the whole cells.

1122 **Image analysis**

1123 In lattice light-sheet and confocal videos, kinetochores as markers for chromosomes and
1124 centrosomes as markers for spindle poles were tracked in a z-stack using the Point Tool in
1125 Fiji/ImageJ. When the signal covered several z-planes, the central z-plane was used for
1126 tracking. Spindle length, pivoting angle (i.e., the angle between the long spindle axis and the
1127 line that connects the kinetochore midpoint with the closer centrosome), cTilt (i.e., the angle
1128 between the long spindle axis and the line that connects sister kinetochores; (Renda et al.,
1129 2022)), interkinetochore distance, distance to closer and further centrosome and distance to
1130 centrosome midpoint were subsequently calculated from the coordinates in 3D using a home-
1131 written MatLab script. The end of centripetal movement was determined as a time point when
1132 the distance of the kinetochore midpoint to the closer centrosome started varying instead of
1133 continuously becoming smaller. The landing on the main spindle surface was determined as a
1134 time point when the pivoting angle was below 60° and cTilt was below 22.5° (Renda et al.,
1135 2022), corresponding to the moment when kinetochores first align along the microtubules of
1136 the main spindle surface, even if they experience subsequent detachments. The landing was
1137 additionally verified visually by checking that a kinetochore pair was adjacent to the
1138 microtubules of the main spindle body. The alignment was defined as the moment when the
1139 kinetochore pair was equidistant (±1-2 µm) to both poles. The formation of the prometaphase
1140 ring was visually determined as a time point when most kinetochores finish their centripetal
1141 movement. The end of spindle elongation was defined as a time point when spindle length
1142 starts varying and/or decreasing instead of continuously increasing. The anaphase onset was
1143 visually determined as a time point when sister kinetochores first start separating. Polar
1144 chromosomes were defined as those that had a pivoting angle of >90° at NEBD and

1145 subsequently made their first contact with the spindle behind the spindle pole. The position of
1146 the first contact was determined at the end of centripetal movement, when the distance of the
1147 kinetochore pair to the spindle contour was usually <3 µm. Pivoting was then analyzed between
1148 the end of centripetal movement until after landing. Only kinetochores that could be reliably
1149 tracked from NEBD to alignment, remaining distinguishable from neighboring kinetochores
1150 throughout this period, were included in the analysis. In Eg5 manipulation experiments,
1151 analysis was done from the first frame when the inhibitor started working, i.e., when the spindle
1152 length started increasing or decreasing.

1153 Successful passage across the pole was defined as the passage across the 90° mark
1154 within 15 minutes from NEBD, not taking into account any subsequent failures to form stable
1155 attachments to microtubules of the main spindle surface. Misaligned chromosomes were
1156 defined as those located within the two spindle poles and less than 2 µm away from the
1157 centrosome/spindle pole in metaphase. Unaligned chromosomes were defined as those located
1158 behind the spindle pole or, alternatively, in front of the pole but not attached to microtubules
1159 of the main spindle surface in metaphase. Lagging chromosomes were defined as those located
1160 in the central part of the spindle with a stretched kinetochore during anaphase.

1161 When chromosomes were labeled instead of kinetochores, two points were put in the
1162 centromeric region during the tracking. When poles were marked with tubulin or EB3 instead
1163 of Centrin1, the point was put in the center of tubulin/EB3 signal. When astral microtubules
1164 were tracked instead of chromosomes or kinetochores, their movement was tracked by putting
1165 two points along the central part of the microtubule contour and their shape was determined by
1166 putting two points at the spindle poles and subsequent five along the entire microtubule
1167 contour. Kinetochore switching between microtubules was investigated using visual analysis.

1168 In STED images of fixed cells, NEBD was determined as the stage when the
1169 centrosomes were one above the other, or when the centrosomes were positioned sideways, but
1170 microtubules did not occupy the whole area between the centrosomes. The beginning of the
1171 centripetal movement was identified by the apparent attachment of all kinetochores to
1172 microtubules at varying distances from the centrosomes, including distances larger than 4 µm.
1173 The end of the centripetal movement was determined as the stage when kinetochores were
1174 arranged in a prometaphase ring at similar distances, smaller than 4 µm, to the centrosomes.
1175 Passage across the pole was identified by the attachment of a kinetochore pair to the
1176 microtubules that were not part of the main spindle body at a stage when the spindle was almost
1177 fully formed. Landing was determined as the stage when a kinetochore pair was found adjacent
1178 to the microtubules of the main spindle body less than 4 µm from the centrosome, and traveling
1179 to the equator when the kinetochores were between 4 µm away from the centrosome and 2 µm
1180 away from the equator.

1181 The length of long xy-, short xy- and z nuclear axes was measured on maximum
1182 intensity projections of the whole cell just before NEBD using the Line Tool in ImageJ. The
1183 long xy axis was defined as the axis with the largest distance between the two opposite sides
1184 of the nuclear border, the short xy axis was defined as perpendicular to the middle of the long
1185 xy axis and z axis was defined as the distance from the first focal plane in which the signal was

1186 present until the last. The spindle axis, used to determine the danger zone, was measured using
1187 the Line Tool in ImageJ on maximum intensity projections of the whole cell when the
1188 prometaphase ring formed and most kinetochores finished their centripetal movement. The
1189 angle between the long nuclear xy axis just before NEBD and the long spindle axis in
1190 prometaphase was then calculated to determine which chromosomes are most likely to attach
1191 behind the pole. This angle was also compared to the angle between the long cellular xy axis
1192 at NEBD, determined using the Line Tool in ImageJ, and the long spindle axis in prometaphase.

1193 The long axis of interphase RPE1 dCas9-GFP cells with labeled subtelomeric region of
1194 chromosome 1 or pericentromeric region of chromosome 9 was measured on maximum
1195 intensity projections of the whole cell. The long axis was then divided into three equal parts
1196 that represent the borders of three cellular compartments - two polar zones and the central zone.
1197 The position of the labeled chromosomes was determined as polar if they were located in any
1198 of the polar zones and as central if they were located in the central zone, respectively.

1199 To determine the position of kinetochore pairs relative to the pole in STED images,
1200 kinetochores and poles were marked in 3D using a Point Tool in ImageJ and the angle that the
1201 line connecting the kinetochore pair midpoint with the closer centrosome forms with the long
1202 spindle axis (i.e., pivoting angle) was subsequently calculated using a home-written MatLab
1203 script. Kinetochore pairs in fixed-cell STED images were considered polar if they were located
1204 above 90° or, alternatively, were located within ~3 μm from the pole but not attached to the
1205 microtubules of the main spindle surface during later stages of prometaphase when the spindle
1206 was already formed.

1207 Attachment types were determined from STED images of fixed cells. Polar
1208 chromosomes were considered attached to microtubules when there was a microtubule either
1209 directly ending at the kinetochore or in very close proximity to the kinetochore. Polar
1210 chromosomes were considered unattached when there was no microtubule in their proximity.
1211 The type of attachment was determined visually. A limitation of this method is that attachment
1212 cannot always be distinguished from mere proximity.

1213 For fixed-cell confocal images of CENP-A together with Mad2 or Astrin or CENP-E
1214 or ZW10, protein levels were measured using the Polygon Tool in ImageJ. The same polygon
1215 was used for measuring the signal in both channels for the same kinetochore, as well as for the
1216 background in the vicinity of the kinetochore in both channels. The final Mad2/CENP-A signal
1217 on the kinetochore was calculated using the formula: Mad2/CENP-A signal = (Integrated
1218 density of Mad2 on the kinetochore – (Kinetochore area x Mean fluorescence of the
1219 background))/(Integrated density of CENP-A on the kinetochore – (Kinetochore area x Mean
1220 fluorescence of the background)). The other 3 proteins were analyzed in the same manner. In
1221 fixed-cell confocal images, kinetochore pairs were classified as polar if their angle exceeded
1222 90°. For each cell, three to ten kinetochores located between the centrosomes were analyzed
1223 and classified as non-polar. Additionally, three to ten kinetochores per metaphase cell were
1224 analyzed. Metaphase cells were identified by the presence of fully formed metaphase plates.

1225 The intensity of microtubules from the opposite side of the spindle, the intensity of
1226 astral microtubules and the accompanying background were measured in a single z-plane using
1227 the 20x20 pixel Square Tool in ImageJ. The final intensity of the microtubules was then
1228 calculated using the formula: Microtubule intensity = Mean intensity of the microtubule –
1229 Mean intensity of the background.

1230 In the validation experiments for protein depletion by siRNA, CENP-E, Spindly,
1231 KIF4A and Kid intensities were measured in sum intensity projections of the entire cell,
1232 covering 33 z-planes or 33 µm. The total signal of the protein of interest within the spindle was
1233 marked by using the Polygon Tool in ImageJ. Background in the cytoplasm was measured
1234 using the 25x25 pixel Square Tool. The total intensities were calculated using the following
1235 formula: Protein intensity = Integrated density within the spindle – (Area of the spindle x Mean
1236 fluorescence of the background). The total intensities were then normalized to the mean total
1237 intensity obtained from control cells.

1238 Tracking of kinetochores in U2OS cells expressing CENP-A-GFP and tubulin-mCherry
1239 was performed using 2D maximum intensity projections and the 'TrackMate' plugin in ImageJ,
1240 with the LoG detector (Ershov et al., 2022). The estimated blob diameter was set to match the
1241 size of a single kinetochore labeled with CENP-A, and thresholding was adjusted until all
1242 visible kinetochores were detected, with no false positives outside the cell. To avoid
1243 interference from neighboring cells, the field of view was cropped accordingly. Using this
1244 approach, the average number of tracked kinetochore pairs at nuclear envelope breakdown
1245 (NEBD) was 42, fewer than the reported modal chromosome number for the U2OS cell line (n
1246 = 74, ATCC). This discrepancy is likely due to insufficient spatial resolution in 2D projections,
1247 which may prevent the complete separation of overlapping kinetochore pairs. The number of
1248 polar chromosomes that successfully passed the spindle pole and reached the metaphase plate
1249 by the end of spindle elongation in live-imaged U2OS cells was calculated by subtracting the
1250 number of identified polar kinetochores remaining behind the pole at the end of spindle
1251 elongation from the total number of polar kinetochores counted at NEBD. Kinetochore pairs at
1252 NEBD and at the end of spindle elongation were classified as polar if their pivoting angle in
1253 2D projection exceeded 90°. The end of spindle elongation was estimated as described
1254 previously (Klaasen et al., 2022). The majority of kinetochores remaining behind the pole were
1255 continuously backtracked frame by frame to NEBD, enabling clear distinction from those that
1256 successfully traversed the spindle pole.

1257 For live-cell measurements of spindle elongation and polar chromosome transit in
1258 cancer cell lines, the spindle length was measured each minute as the 2D distance between the
1259 two spindle poles using the Line Tool in ImageJ. Coupled with this were the measurements of
1260 the polar transit time for each cell, defined as the time point when the last chromosome of those
1261 that were initially polar moved from the back side to the front side of the centrosome.

1262 All measurements were performed in ImageJ/Fiji (National Institutes of Health),
1263 followed by data analysis in MATLAB (MathWorks). Figures and schematic representations
1264 were assembled in Adobe Illustrator CC (Adobe Systems). Generally, the Shapiro-Wilk test
1265 was used to determine normality of the sample data. T-test (for two samples unless stated

otherwise) or ANOVA with post-hoc Tukey test (for more than two samples) were then used for data that followed a normal distribution, and Mann-Whitney U test (for two samples) or Kruskal-Wallis with posthoc Dunn's test (for more than two samples) were used otherwise. To analyze categorical data, Chi-squared test was used for larger samples (N > 50) and Fisher's exact test was used for smaller samples. The result was considered statistically significant when the p-value was equal to or less than 0.05. Statistical analysis was performed as noted in the respective Figure captions.

Author Contribution

I.K. and V.Š. performed all experiments and analyzed the data, except for the following: experiments on Astrin and the cancer cell lines MDA-MB-231, Caco-2, and a subset of OVSAHO cells were conducted by M.Đ., experiments involving CENP-E inhibition, corona proteins, and U2OS cells with labeled kinetochores and microtubules were carried out by K.V., and experiments on chromosomes 1 and 9 were performed by P.M. I.K., V.Š., and I.M.T. wrote the manuscript with contribution from M.Đ. and K.V. I.M.T. supervised the project.

Acknowledgments

The authors thank Alexey Khodjakov, Jonathon Pines, Andrew Holland, Will Krek, Marin Barišić, Susanne Lens and Julie Welburn for the cell lines; Oliver Vugrek and Filip Rokić for help with lentiviral work, Marko Šprem and the Abberior team for help with the Expert Line easy3D STED microscope system setup and developing microscopy protocols; Ivana Šarić for help with the drawings, members of the Tolić, Pavin, Kops, and Meraldi groups for helpful discussions and advice. The authors acknowledge funding by the European Research Council (ERC Synergy Grant, GA Number 855158), the Croatian Science Foundation (HRZZ) through Swiss-Croatian Bilateral Projects (project IPCH-2022-10-9344) and Cooperation Programme with Croatian Scientists in the Diaspora "Research Cooperability" (project PZS-2019-02-7653), and projects co-financed by the Croatian Government and the European Union through the European Regional Development Fund—the Competitiveness and Cohesion Operational Programme: IPSted (Grant KK.01.1.1.04.0057) and QuantiXLie Center of Excellence (Grant KK.01.1.1.01.0004).

Competing interests

The authors declare no competing interests.

Data availability

Source data are provided with this paper. All other data supporting the findings of this study are available from the corresponding author on reasonable request.

Code availability

Codes used to analyze and plot the data are available from the corresponding author on request.

References

Alexander, S.P., Rieder, C.L., 1991. Chromosome motion during attachment to the vertebrate spindle: initial saltatory-like behavior of chromosomes and quantitative analysis of force production by nascent kinetochore fibers. J. Cell Biol. 113, 805–815. https://doi.org/10.1083/jcb.113.4.805

Bakhoum, S.F., Genovese, G., Compton, D.A., 2009. Deviant Kinetochore Microtubule Dynamics Underlie Chromosomal Instability. Curr. Biol. 19, 1937–1942. https://doi.org/10.1016/j.cub.2009.09.055

Barisic, M., Aguiar, P., Geley, S., Maiato, H., 2014. Kinetochore motors drive congression of peripheral polar chromosomes by overcoming random arm-ejection forces. Nat. Cell Biol. 16, 1249–1256. https://doi.org/10.1038/ncb3060

Barretina, J., Caponigro, G., Stransky, N., Venkatesan, K., Margolin, A.A., Kim, S., Wilson, C.J., Lehár, J., Kryukov, G.V., Sonkin, D., Reddy, A., Liu, M., Murray, L., Berger, M.F., Monahan, J.E., Morais, P., Meltzer, J., Korejwa, A., Jané-Valbuena, J., Mapa, F.A., Thibault, J., Bric-Furlong, E., Raman, P., Shipway, A., Engels, I.H., Cheng, J., Yu, G.K., Yu, J., Aspesi, P., de Silva, M., Jagtap, K., Jones, M.D., Wang, L., Hatton, C., Palescandolo, E., Gupta, S., Mahan, S., Sougnez, C., Onofrio, R.C., Liefeld, T., MacConaill, L., Winckler, W., Reich, M., Li, N., Mesirov, J.P., Gabriel, S.B., Getz, G., Ardlie, K., Chan, V., Myer, V.E., Weber, B.L., Porter, J., Warmuth, M., Finan, P., Harris, J.L., Meyerson, M., Golub, T.R., Morrissey, M.P., Sellers, W.R., Schlegel, R., Garraway, L.A., 2012. The Cancer Cell Line Encyclopedia enables predictive modelling of anticancer drug sensitivity. Nature 483, 603–607. https://doi.org/10.1038/nature11003

Berg, H.C., 1993. Random Walks in Biology: New and Expanded Edition, Subsequent edition. ed. Princeton University Press, Princeton, N.J.

Bird, A.W., Hyman, A.A., 2008. Building a spindle of the correct length in human cells requires the interaction between TPX2 and Aurora A. J. Cell Biol. 182, 289–300. https://doi.org/10.1083/jcb.200802005

Bolzer, A., Kreth, G., Solovei, I., Koehler, D., Saracoglu, K., Fauth, C., Müller, S., Eils, R., Cremer, C., Speicher, M.R., Cremer, T., 2005. Three-Dimensional Maps of All Chromosomes in Human Male Fibroblast Nuclei and Prometaphase Rosettes. PLOS Biol. 3, e157. https://doi.org/10.1371/journal.pbio.0030157

Booth, A.J., Yue, Z., Eykelenboom, J.K., Stiff, T., Luxton, G.G., Hochegger, H., Tanaka, T.U., 2019. Contractile acto-myosin network on nuclear envelope remnants positions human chromosomes for mitosis. eLife 8, e46902. https://doi.org/10.7554/eLife.46902

Buđa, R., Vukušić, K., Tolić, I.M., 2017. Dissection and characterization of microtubule bundles in the mitotic spindle using femtosecond laser ablation. Methods Cell Biol. 139, 81–101. https://doi.org/10.1016/bs.mcb.2016.11.007

Cai, S., O'Connell, C.B., Khodjakov, A., Walczak, C.E., 2009. Chromosome congression in the absence of kinetochore fibres. Nat. Cell Biol. 11, 832–838. https://doi.org/10.1038/ncb1890

Castrogiovanni, C., Inchingolo, A.V., Harrison, J.U., Dudka, D., Sen, O., Burroughs, N.J., McAinsh, A.D., Meraldi, P., 2022. Evidence for a HURP/EB free mixed-nucleotide zone in kinetochore-microtubules. Nat. Commun. 13, 4704. https://doi.org/10.1038/s41467-022-32421-x

Cerami, E., Gao, J., Dogrusoz, U., Gross, B.E., Sumer, S.O., Aksoy, B.A., Jacobsen, A., Byrne, C.J., Heuer, M.L., Larsson, E., Antipin, Y., Reva, B., Goldberg, A.P., Sander, C., Schultz, N., 2012. The cBio cancer genomics portal: an open platform for exploring multidimensional cancer genomics data. Cancer Discov. 2, 401–404. https://doi.org/10.1158/2159-8290.CD-12-0095

Choi, S.H., McCollum, D., 2012. A role for metaphase spindle elongation forces in correction of merotelic kinetochore attachments. Curr. Biol. CB 22, 225–230. https://doi.org/10.1016/j.cub.2011.12.022

Chong, M.K., Rosas-Salvans, M., Tran, V., Dumont, S., 2024. Chromosome size-dependent polar ejection force impairs mammalian mitotic error correction. J. Cell Biol. 223, e202310010. https://doi.org/10.1083/jcb.202310010

Craske, B., Welburn, J.P.I., 2020. Leaving no-one behind: how CENP-E facilitates chromosome alignment. Essays Biochem. 64, 313–324. https://doi.org/10.1042/EBC20190073

de Bruijn, I., Kundra, R., Mastrogiacomo, B., Tran, T.N., Sikina, L., Mazor, T., Li, X., Ochoa, A., Zhao, G., Lai, B., Abeshouse, A., Baiceanu, D., Ciftci, E., Dogrusoz, U., Dufilie, A., Erkoc, Z., Garcia Lara, E., Fu, Z., Gross, B., Haynes, C., Heath, A., Higgins, D., Jagannathan, P., Kalletla, K., Kumari, P., Lindsay, J., Lisman, A., Leenknegt, B., Lukasse, P., Madela, D., Madupuri, R., van Nierop, P., Plantalech, O., Quach, J., Resnick, A.C., Rodenburg, S.Y.A., Satravada, B.A., Schaeffer, F., Sheridan, R., Singh, J., Sirohi, R., Sumer, S.O., van Hagen, S., Wang, A., Wilson, M., Zhang, H., Zhu, K., Rusk, N., Brown, S., Lavery, J.A., Panageas, K.S., Rudolph, J.E., LeNoue-Newton, M.L., Warner, J.L., Guo, X., Hunter-Zinck, H., Yu, T.V., Pilai, S., Nichols, C., Gardos, S.M., Philip, J., AACR Project GENIE BPC Core Team, AACR Project GENIE Consortium, Kehl, K.L., Riely, G.J., Schrag, D., Lee, J., Fiandalo, M.V., Sweeney, S.M., Pugh, T.J., Sander, C., Cerami, E., Gao, J., Schultz, N., 2023. Analysis and Visualization of Longitudinal Genomic and Clinical Data from the AACR Project GENIE Biopharma Collaborative in cBioPortal. Cancer Res. 83, 3861–3867. https://doi.org/10.1158/0008-5472.CAN-23-0816

Dick, A.E., Gerlich, D.W., 2013. Kinetic framework of spindle assembly checkpoint signalling. Nat. Cell Biol. 15, 1370–1377. https://doi.org/10.1038/ncb2842

Dumont, M., Gamba, R., Gestraud, P., Klaasen, S., Worrall, J.T., De Vries, S.G., Boudreau, V., Salinas-Luypaert, C., Maddox, P.S., Lens, S.M., Kops, G.J., McClelland, S.E., Miga, K.H., Fachinetti, D., 2020. Human chromosome-specific aneuploidy is influenced by DNA-dependent centromeric features. EMBO J. 39, e102924. https://doi.org/10.15252/embj.2019102924

Ershov, D., Phan, M.-S., Pylvänäinen, J.W., Rigaud, S.U., Le Blanc, L., Charles-Orszag, A., Conway, J.R.W., Laine, R.F., Roy, N.H., Bonazzi, D., Duménil, G., Jacquemet, G., Tinevez, J.-Y., 2022. TrackMate 7: integrating state-of-the-art segmentation

algorithms into tracking pipelines. Nat. Methods 19, 829–832. https://doi.org/10.1038/s41592-022-01507-1

Ertych, N., Stolz, A., Stenzinger, A., Weichert, W., Kaulfuß, S., Burfeind, P., Aigner, A., Wordeman, L., Bastians, H., 2014. Increased microtubule assembly rates influence chromosomal instability in colorectal cancer cells. Nat. Cell Biol. 16, 779–791. https://doi.org/10.1038/ncb2994

Ferrandiz, N., Downie, L., Starling, G.P., Royle, S.J., 2022. Endomembranes promote chromosome missegregation by ensheathing misaligned chromosomes. J. Cell Biol. 221, e202203021. https://doi.org/10.1083/jcb.202203021

Gao, J., Aksoy, B.A., Dogrusoz, U., Dresdner, G., Gross, B., Sumer, S.O., Sun, Y., Jacobsen, A., Sinha, R., Larsson, E., Cerami, E., Sander, C., Schultz, N., 2013. Integrative analysis of complex cancer genomics and clinical profiles using the cBioPortal. Sci. Signal. 6, pl1. https://doi.org/10.1126/scisignal.2004088

Gasic, I., Nerurkar, P., Meraldi, P., 2015. Centrosome age regulates kinetochore–microtubule stability and biases chromosome mis-segregation. eLife 4, e07909. https://doi.org/10.7554/eLife.07909

Ghandi, M., Huang, F.W., Jané-Valbuena, J., Kryukov, G.V., Lo, C.C., McDonald, E.R., Barretina, J., Gelfand, E.T., Bielski, C.M., Li, H., Hu, K., Andreev-Drakhlin, A.Y., Kim, J., Hess, J.M., Haas, B.J., Aguet, F., Weir, B.A., Rothberg, M.V., Paolella, B.R., Lawrence, M.S., Akbani, R., Lu, Y., Tiv, H.L., Gokhale, P.C., de Weck, A., Mansour, A.A., Oh, C., Shih, J., Hadi, K., Rosen, Y., Bistline, J., Venkatesan, K., Reddy, A., Sonkin, D., Liu, M., Lehar, J., Korn, J.M., Porter, D.A., Jones, M.D., Golji, J., Caponigro, G., Taylor, J.E., Dunning, C.M., Creech, A.L., Warren, A.C., McFarland, J.M., Zamanighomi, M., Kauffmann, A., Stransky, N., Imielinski, M., Maruvka, Y.E., Cherniack, A.D., Tsherniak, A., Vazquez, F., Jaffe, J.D., Lane, A.A., Weinstock, D.M., Johannessen, C.M., Morrissey, M.P., Stegmeier, F., Schlegel, R., Hahn, W.C., Getz, G., Mills, G.B., Boehm, J.S., Golub, T.R., Garraway, L.A., Sellers, W.R., 2019. Next-generation characterization of the Cancer Cell Line Encyclopedia. Nature 569, 503–508. https://doi.org/10.1038/s41586-019-1186-3

Girish, V., Lakhani, A.A., Thompson, S.L., Scaduto, C.M., Brown, L.M., Hagenson, R.A., Sausville, E.L., Mendelson, B.E., Kandikuppa, P.K., Lukow, D.A., Yuan, M.L., Stevens, E.C., Lee, S.N., Schukken, K.M., Akalu, S.M., Vasudevan, A., Zou, C., Salovska, B., Li, W., Smith, J.C., Taylor, A.M., Martienssen, R.A., Liu, Y., Sun, R., Sheltzer, J.M., 2023. Oncogene-like addiction to aneuploidy in human cancers. Science 381, eadg4521. https://doi.org/10.1126/science.adg4521

Gomes, A.M., Orr, B., Novais-Cruz, M., De Sousa, F., Macário-Monteiro, J., Lemos, C., Ferrás, C., Maiato, H., 2022. Micronuclei from misaligned chromosomes that satisfy the spindle assembly checkpoint in cancer cells. Curr. Biol. CB 32, 4240-4254.e5. https://doi.org/10.1016/j.cub.2022.08.026

Griffis, E.R., Stuurman, N., Vale, R.D., 2007. Spindly, a novel protein essential for silencing the spindle assembly checkpoint, recruits dynein to the kinetochore. J. Cell Biol. 177, 1005–1015. https://doi.org/10.1083/jcb.200702062

Groen, A.C., Needleman, D., Brangwynne, C., Gradinaru, C., Fowler, B., Mazitschek, R., Mitchison, T.J., 2008. A novel small-molecule inhibitor reveals a possible role of kinesin-5 in anastral spindle-pole assembly. J. Cell Sci. 121, 2293–2300. https://doi.org/10.1242/jcs.024018

He, J., Zhang, Z., Ouyang, M., Yang, F., Hao, H., Lamb, K.L., Yang, J., Yin, Y., Shen, W.H., 2016. PTEN regulates EG5 to control spindle architecture and chromosome congression during mitosis. Nat. Commun. 7, 12355. https://doi.org/10.1038/ncomms12355

Hewitt, L., Tighe, A., Santaguida, S., White, A.M., Jones, C.D., Musacchio, A., Green, S., Taylor, S.S., 2010. Sustained Mps1 activity is required in mitosis to recruit O-Mad2 to the Mad1–C-Mad2 core complex. J. Cell Biol. 190, 25–34. https://doi.org/10.1083/jcb.201002133

Holland, A.J., Fachinetti, D., Da Cruz, S., Zhu, Q., Vitre, B., Lince-Faria, M., Chen, D., Parish, N., Verma, I.M., Bettencourt-Dias, M., Cleveland, D.W., 2012. Polo-like kinase 4 controls centriole duplication but does not directly regulate cytokinesis. Mol. Biol. Cell 23, 1838–1845. https://doi.org/10.1091/mbc.E11-12-1043

Jagrić, M., Risteski, P., Martinčić, J., Milas, A., Tolić, I.M., 2021. Optogenetic control of PRC1 reveals its role in chromosome alignment on the spindle by overlap length-dependent forces. eLife 10, e61170. https://doi.org/10.7554/eLife.61170

Kabeche, L., Compton, D.A., 2013. Cyclin A regulates kinetochore microtubules to promote faithful chromosome segregation. Nature 502, 110–113. https://doi.org/10.1038/nature12507

Kajtez, J., Solomatina, A., Novak, M., Polak, B., Vukušić, K., Rüdiger, J., Cojoc, G., Milas, A., Šumanovac Šestak, I., Risteski, P., Tavano, F., Klemm, A.H., Roscioli, E., Welburn, J., Cimini, D., Glunčić, M., Pavin, N., Tolić, I.M., 2016. Overlap microtubules link sister k-fibres and balance the forces on bi-oriented kinetochores. Nat. Commun. 7, 10298. https://doi.org/10.1038/ncomms10298

Kalinina, I., Nandi, A., Delivani, P., Chacón, M.R., Klemm, A.H., Ramunno-Johnson, D., Krull, A., Lindner, B., Pavin, N., Tolić-Nørrelykke, I.M., 2013. Pivoting of microtubules around the spindle pole accelerates kinetochore capture. Nat. Cell Biol. 15, 82–87. https://doi.org/10.1038/ncb2640

Kapitein, L.C., Peterman, E.J.G., Kwok, B.H., Kim, J.H., Kapoor, T.M., Schmidt, C.F., 2005. The bipolar mitotic kinesin Eg5 moves on both microtubules that it crosslinks. Nature 435, 114–118. https://doi.org/10.1038/nature03503

Kapoor, T.M., Lampson, M.A., Hergert, P., Cameron, L., Cimini, D., Salmon, E.D., McEwen, B.F., Khodjakov, A., 2006. Chromosomes can congress to the metaphase plate before biorientation. Science 311, 388–391. https://doi.org/10.1126/science.1122142

Kaseda, K., McAinsh, A.D., Cross, R.A., 2011. Dual pathway spindle assembly increases both the speed and the fidelity of mitosis. Biol. Open 1, 12–18. https://doi.org/10.1242/bio.2011012

Kashina, A.S., Rogers, G.C., Scholey, J.M., 1997. The bimC family of kinesins: essential bipolar mitotic motors driving centrosome separation. Biochim. Biophys. Acta 1357, 257–271. https://doi.org/10.1016/s0167-4889(97)00037-2

Kiewisz, R., Fabig, G., Conway, W., Baum, D., Needleman, D., Müller-Reichert, T., 2022. Three-dimensional structure of kinetochore-fibers in human mitotic spindles. eLife 11, e75459. https://doi.org/10.7554/eLife.75459

Klaasen, S.J., Truong, M.A., van Jaarsveld, R.H., Koprivec, I., Štimac, V., de Vries, S.G., Risteski, P., Kodba, S., Vukušić, K., de Luca, K.L., Marques, J.F., Gerrits, E.M., Bakker, B., Foijer, F., Kind, J., Tolić, I.M., Lens, S.M.A., Kops, G.J.P.L., 2022. Nuclear chromosome locations dictate segregation error frequencies. Nature 607, 604–609. https://doi.org/10.1038/s41586-022-04938-0

Kletter, T., Reusch, S., Cavazza, T., Dempewolf, N., Tischer, C., Reber, S., 2022. Volumetric morphometry reveals spindle width as the best predictor of mammalian spindle scaling. J. Cell Biol. 221, e202106170. https://doi.org/10.1083/jcb.202106170

Koch, A., Maia, A., Janssen, A., Medema, R.H., 2016. Molecular basis underlying resistance to Mps1/TTK inhibitors. Oncogene 35, 2518–2528. https://doi.org/10.1038/onc.2015.319

Koprivec, I., Štimac, V., Tolić, I.M., 2025. Super-Resolution Imaging of Mitotic Spindle Microtubules Using STED Microscopy. Methods Mol. Biol. Clifton NJ 2872, 3–19. https://doi.org/10.1007/978-1-0716-4224-5_1

Kuhn, J., Dumont, S., 2017. Spindle assembly checkpoint satisfaction occurs via end-on but not lateral attachments under tension. J. Cell Biol. 216, 1533–1542. https://doi.org/10.1083/jcb.201611104

Li, J., Yen, C., Liaw, D., Podsypanina, K., Bose, S., Wang, S.I., Puc, J., Miliaresis, C., Rodgers, L., McCombie, R., Bigner, S.H., Giovanella, B.C., Ittmann, M., Tycko, B., Hibshoosh, H., Wigler, M.H., Parsons, R., 1997. PTEN, a putative protein tyrosine phosphatase gene mutated in human brain, breast, and prostate cancer. Science 275, 1943–1947. https://doi.org/10.1126/science.275.5308.1943

Li, Y., Yu, W., Liang, Y., Zhu, X., 2007. Kinetochore dynein generates a poleward pulling force to facilitate congression and full chromosome alignment. Cell Res. 17, 701–712. https://doi.org/10.1038/cr.2007.65

Lukinavičius, G., Reymond, L., D'Este, E., Masharina, A., Göttfert, F., Ta, H., Güther, A., Fournier, M., Rizzo, S., Waldmann, H., Blaukopf, C., Sommer, C., Gerlich, D.W., Arndt, H.-D., Hell, S.W., Johnsson, K., 2014. Fluorogenic probes for live-cell imaging of the cytoskeleton. Nat. Methods 11, 731–733. https://doi.org/10.1038/nmeth.2972

Mack, G.J., Compton, D.A., 2001. Analysis of mitotic microtubule-associated proteins using mass spectrometry identifies astrin, a spindle-associated protein. Proc. Natl. Acad. Sci. 98, 14434–14439. https://doi.org/10.1073/pnas.261371298

Magidson, V., O'Connell, C.B., Lončarek, J., Paul, R., Mogilner, A., Khodjakov, A., 2011. The spatial arrangement of chromosomes during prometaphase facilitates spindle assembly. Cell 146, 555–567. https://doi.org/10.1016/j.cell.2011.07.012

Maiato, H., Gomes, A.M., Sousa, F., Barisic, M., 2017. Mechanisms of Chromosome Congression during Mitosis. Biology 6, 13. https://doi.org/10.3390/biology6010013

Marcozzi, C., Pines, J., 2018. Assays for the spindle assembly checkpoint in cell culture. Methods Cell Biol. 144, 1–13. https://doi.org/10.1016/bs.mcb.2018.03.001

Mayer, T.U., Kapoor, T.M., Haggarty, S.J., King, R.W., Schreiber, S.L., Mitchison, T.J., 1999. Small molecule inhibitor of mitotic spindle bipolarity identified in a phenotype-based screen. Science 286, 971–974. https://doi.org/10.1126/science.286.5441.971

Mazumdar, M., Sundareshan, S., Misteli, T., 2004. Human chromokinesin KIF4A functions in chromosome condensation and segregation. J. Cell Biol. 166, 613–620. https://doi.org/10.1083/jcb.200401142

McEwen, B.F., Chan, G.K.T., Zubrowski, B., Savoian, M.S., Sauer, M.T., Yen, T.J., 2001. CENP-E Is Essential for Reliable Bioriented Spindle Attachment, but Chromosome Alignment Can Be Achieved via Redundant Mechanisms in Mammalian Cells. Mol. Biol. Cell 12, 2776–2789.

Novais-Cruz, M., Pombinho, A., Sousa, M., Maia, A.F., Maiato, H., Ferrás, C., 2023. Mitotic DNA damage promotes chromokinesin-mediated missegregation of polar chromosomes in cancer cells. Mol. Biol. Cell 34, ar47. https://doi.org/10.1091/mbc.E22-11-0518

Pereira, C., Reis, R.M., Gama, J.B., Celestino, R., Cheerambathur, D.K., Carvalho, A.X., Gassmann, R., 2018. Self-Assembly of the RZZ Complex into Filaments Drives Kinetochore Expansion in the Absence of Microtubule Attachment. Curr. Biol. CB 28, 3408-3421.e8. https://doi.org/10.1016/j.cub.2018.08.056

Ponjavić, I., Vukušić, K., Tolić, I.M., 2021. Expansion microscopy of the mitotic spindle. Methods Cell Biol. 161, 247–274. https://doi.org/10.1016/bs.mcb.2020.04.014

Rajendraprasad, G., Eibes, S., Boldú, C.G., Barisic, M., 2021. TH588 and Low-Dose Nocodazole Impair Chromosome Congression by Suppressing Microtubule Turnover within the Mitotic Spindle. Cancers 13, 5995. https://doi.org/10.3390/cancers13235995

Reinhold, W.C., Sunshine, M., Liu, H., Varma, S., Kohn, K.W., Morris, J., Doroshow, J., Pommier, Y., 2012. CellMiner: a web-based suite of genomic and pharmacologic tools to explore transcript and drug patterns in the NCI-60 cell line set. Cancer Res. 72, 3499–3511. https://doi.org/10.1158/0008-5472.CAN-12-1370

Renda, F., Miles, C., Tikhonenko, I., Fisher, R., Carlini, L., Kapoor, T.M., Mogilner, A., Khodjakov, A., 2022. Non-centrosomal microtubules at kinetochores promote rapid chromosome biorientation during mitosis in human cells. Curr. Biol. CB 32, 1049-1063.e4. https://doi.org/10.1016/j.cub.2022.01.013

Rickert, K.W., Schaber, M., Torrent, M., Neilson, L.A., Tasber, E.S., Garbaccio, R., Coleman, P.J., Harvey, D., Zhang, Y., Yang, Y., Marshall, G., Lee, L., Walsh, E.S., Hamilton, K., Buser, C.A., 2008. Discovery and biochemical characterization of selective ATP competitive inhibitors of the human mitotic kinesin KSP. Arch. Biochem. Biophys. 469, 220–231. https://doi.org/10.1016/j.abb.2007.10.016

Rieder, C.L., Alexander, S.P., 1990. Kinetochores are transported poleward along a single astral microtubule during chromosome attachment to the spindle in newt lung cells. J. Cell Biol. 110, 81–95. https://doi.org/10.1083/jcb.110.1.81

Risteski, P., Martinčić, J., Jagrić, M., Tintor, E., Petelinec, A., Tolić, I.M., 2024. Microtubule poleward flux as a target for modifying chromosome segregation errors. Proc. Natl. Acad. Sci. 121, e2405015121. https://doi.org/10.1073/pnas.2405015121

Sacristan, C., Ahmad, M.U.D., Keller, J., Fermie, J., Groenewold, V., Tromer, E., Fish, A., Melero, R., Carazo, J.M., Klumperman, J., Musacchio, A., Perrakis, A., Kops, G.J., 2018. Dynamic kinetochore size regulation promotes microtubule capture and chromosome biorientation in mitosis. Nat. Cell Biol. 20, 800–810. https://doi.org/10.1038/s41556-018-0130-3

Schmidt, J.C., Kiyomitsu, T., Hori, T., Backer, C.B., Fukagawa, T., Cheeseman, I.M., 2010. Aurora B kinase controls the targeting of the Astrin-SKAP complex to bioriented kinetochores. J. Cell Biol. 191, 269–280. https://doi.org/10.1083/jcb.201006129

Shi, Y., Tabet, J.S., Milkie, D.E., Daugird, T.A., Yang, C.Q., Ritter, A.T., Giovannucci, A., Legant, W.R., 2024. Smart lattice light-sheet microscopy for imaging rare and complex cellular events. Nat. Methods 21, 301–310. https://doi.org/10.1038/s41592-023-02126-0

Shrestha, R.L., Draviam, V.M., 2013. Lateral to end-on conversion of chromosome-microtubule attachment requires kinesins CENP-E and MCAK. Curr. Biol. CB 23, 1514–1526. https://doi.org/10.1016/j.cub.2013.06.040

Simunić, J., Tolić, I.M., 2016. Mitotic Spindle Assembly: Building the Bridge between Sister K-Fibers. Trends Biochem. Sci. 41, 824–833. https://doi.org/10.1016/j.tibs.2016.07.004

Skoufias, D.A., DeBonis, S., Saoudi, Y., Lebeau, L., Crevel, I., Cross, R., Wade, R.H., Hackney, D., Kozielski, F., 2006. S-trityl-L-cysteine is a reversible, tight binding inhibitor of the human kinesin Eg5 that specifically blocks mitotic progression. J. Biol. Chem. 281, 17559–17569. https://doi.org/10.1074/jbc.M511735200

Stepanova, T., Slemmer, J., Hoogenraad, C.C., Lansbergen, G., Dortland, B., De Zeeuw, C.I., Grosveld, F., van Cappellen, G., Akhmanova, A., Galjart, N., 2003. Visualization of microtubule growth in cultured neurons via the use of EB3-GFP (end-binding protein 3-green fluorescent protein). J. Neurosci. Off. J. Soc. Neurosci. 23, 2655–2664. https://doi.org/10.1523/JNEUROSCI.23-07-02655.2003

Stiff, T., Echegaray-Iturra, F.R., Pink, H.J., Herbert, A., Reyes-Aldasoro, C.C., Hochegger, H., 2020. Prophase-Specific Perinuclear Actin Coordinates Centrosome Separation and Positioning to Ensure Accurate Chromosome Segregation. Cell Rep. 31, 107681. https://doi.org/10.1016/j.celrep.2020.107681

Štimac, V., Koprivec, I., Manenica, M., Simunić, J., Tolić, I.M., 2022. Augmin prevents merotelic attachments by promoting proper arrangement of bridging and kinetochore fibers. eLife 11, e83287. https://doi.org/10.7554/eLife.83287

Tamura, N., Shaikh, N., Muliaditan, D., Soliman, T.N., McGuinness, J.R., Maniati, E., Moralli, D., Durin, M.-A., Green, C.M., Balkwill, F.R., Wang, J., Curtius, K., McClelland, S.E., 2020. Specific Mechanisms of Chromosomal Instability Indicate Therapeutic Sensitivities in High-Grade Serous Ovarian Carcinoma. Cancer Res. 80, 4946–4959. https://doi.org/10.1158/0008-5472.CAN-19-0852

Thompson, S.L., Compton, D.A., 2008. Examining the link between chromosomal instability and aneuploidy in human cells. J. Cell Biol. 180, 665–672. https://doi.org/10.1083/jcb.200712029

Tovini, L., McClelland, S.E., 2019. Impaired CENP-E Function Renders Large Chromosomes More Vulnerable to Congression Failure. Biomolecules 9, 44. https://doi.org/10.3390/biom9020044

Truong, M.A., Cané-Gasull, P., de Vries, S.G., Nijenhuis, W., Wardenaar, R., Kapitein, L.C., Foijer, F., Lens, S.M., 2023. A kinesin-based approach for inducing chromosome-specific mis-segregation in human cells. EMBO J. 42, e111559. https://doi.org/10.15252/embj.2022111559

Tucker, J.B., Bonema, S.C., García-Varela, R., Denu, R.A., Hu, Y., McGregor, S.M., Burkard, M.E., Weaver, B.A., 2023. Misaligned Chromosomes are a Major Source of Chromosomal Instability in Breast Cancer. Cancer Res. Commun. 3, 54–65. https://doi.org/10.1158/2767-9764.CRC-22-0302

Turnham, D.J., Bullock, N., Dass, M.S., Staffurth, J.N., Pearson, H.B., 2020. The PTEN Conundrum: How to Target PTEN-Deficient Prostate Cancer. Cells 9, 2342. https://doi.org/10.3390/cells9112342

Vasquez, R.J., Howell, B., Yvon, A.M., Wadsworth, P., Cassimeris, L., 1997. Nanomolar concentrations of nocodazole alter microtubule dynamic instability in vivo and in vitro. Mol. Biol. Cell 8, 973–985. https://doi.org/10.1091/mbc.8.6.973

Vukušić, K., Tolić, I.M., 2024. CENP-E initiates chromosome congression by opposing Aurora kinases to promote end-on attachments. bioRxiv 2023.10.19.563150. https://doi.org/10.1101/2023.10.19.563150

Vukušić, K., Tolić, I.M., 2022. Polar Chromosomes-Challenges of a Risky Path. Cells 11, 1531. https://doi.org/10.3390/cells11091531

Wandke, C., Barisic, M., Sigl, R., Rauch, V., Wolf, F., Amaro, A.C., Tan, C.H., Pereira, A.J., Kutay, U., Maiato, H., Meraldi, P., Geley, S., 2012. Human chromokinesins promote chromosome congression and spindle microtubule dynamics during mitosis. J. Cell Biol. 198, 847–863. https://doi.org/10.1083/jcb.201110060

Waters, J.C., Chen, R.H., Murray, A.W., Salmon, E.D., 1998. Localization of Mad2 to kinetochores depends on microtubule attachment, not tension. J. Cell Biol. 141, 1181–1191. https://doi.org/10.1083/jcb.141.5.1181

Wood, K.W., Lad, L., Luo, L., Qian, X., Knight, S.D., Nevins, N., Brejc, K., Sutton, D., Gilmartin, A.G., Chua, P.R., Desai, R., Schauer, S.P., McNulty, D.E., Annan, R.S., Belmont, L.D., Garcia, C., Lee, Y., Diamond, M.A., Faucette, L.F., Giardiniere, M., Zhang, S., Sun, C.-M., Vidal, J.D., Lichtsteiner, S., Cornwell, W.D., Greshock, J.D., Wooster, R.F., Finer, J.T., Copeland, R.A., Huang, P.S., Morgans, D.J., Dhanak, D., Bergnes, G., Sakowicz, R., Jackson, J.R., 2010. Antitumor activity of an allosteric

1642 inhibitor of centromere-associated protein-E. Proc. Natl. Acad. Sci. 107, 5839–5844.
1643 https://doi.org/10.1073/pnas.0915068107
1644 Woodruff, J.B., Wueseke, O., Hyman, A.A., 2014. Pericentriolar material structure and
1645 dynamics. Philos. Trans. R. Soc. Lond. B. Biol. Sci. 369, 20130459.
1646 https://doi.org/10.1098/rstb.2013.0459
1647 Worrall, J.T., Tamura, N., Mazzagatti, A., Shaikh, N., van Lingen, T., Bakker, B., Spierings,
1648 D.C.J., Vladimirou, E., Foijer, F., McClelland, S.E., 2018. Non-random Mis-
1649 segregation of Human Chromosomes. Cell Rep. 23, 3366–3380.
1650 https://doi.org/10.1016/j.celrep.2018.05.047
1651 Wu, J., Raas, M.W.D., Alcaraz, P.S., Vos, H.R., Tromer, E.C., Snel, B., Kops, G.J.P.L.,
1652 2023. A farnesyl-dependent structural role for CENP-E in expansion of the fibrous
1653 corona. J. Cell Biol. 223, e202303007. https://doi.org/10.1083/jcb.202303007
1654 Yajima, J., Edamatsu, M., Watai-Nishii, J., Tokai-Nishizumi, N., Yamamoto, T., Toyoshima,
1655 Y.Y., 2003. The human chromokinesin Kid is a plus end-directed microtubule-based
1656 motor. EMBO J. 22, 1067–1074. https://doi.org/10.1093/emboj/cdg102
1657 Yang, Z., Tulu, U.S., Wadsworth, P., Rieder, C.L., 2007. Kinetochore Dynein Is Required for
1658 Chromosome Motion and Congression Independent of the Spindle Checkpoint. Curr.
1659 Biol. CB 17, 973–980. https://doi.org/10.1016/j.cub.2007.04.056
1660 Yao, X., Anderson, K.L., Cleveland, D.W., 1997. The Microtubule-dependent Motor
1661 Centromere–associated Protein E (CENP-E) Is an Integral Component of Kinetochore
1662 Corona Fibers That Link Centromeres to Spindle Microtubules. J. Cell Biol. 139,
1663 435–447. https://doi.org/10.1083/jcb.139.2.435
1664 Yin, Y., Shen, W.H., 2008. PTEN: a new guardian of the genome. Oncogene 27, 5443–5453.
1665 https://doi.org/10.1038/onc.2008.241
1666 Zhang, C., Kang, J.S., Asano, S.M., Gao, R., Boyden, E.S., 2020. Expansion Microscopy for
1667 Beginners: Visualizing Microtubules in Expanded Cultured HeLa Cells. Curr. Protoc.
1668 Neurosci. 92, e96. https://doi.org/10.1002/cpns.96
1669

Supplementary Material

Supplementary Figures S1-S7

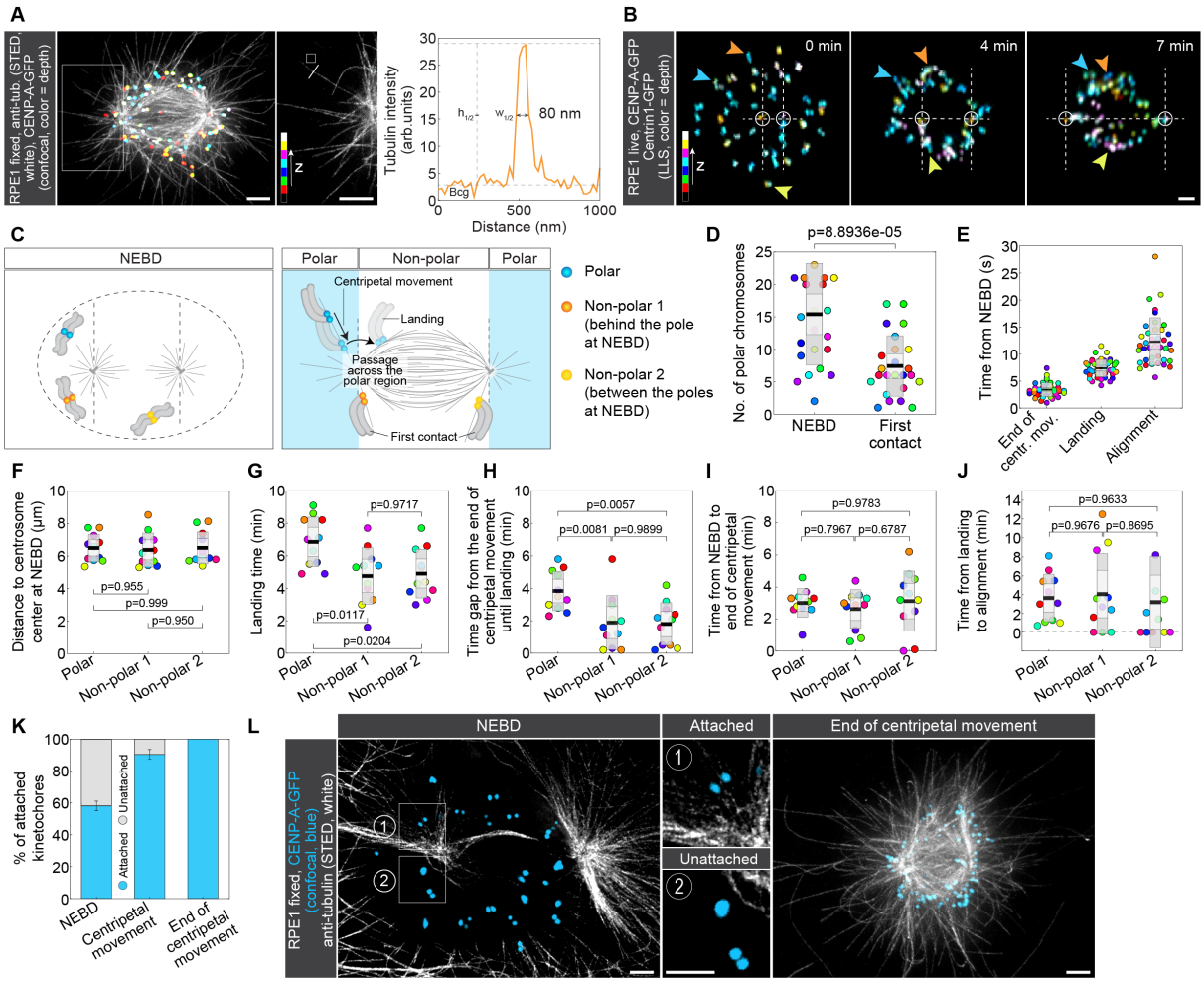

Supplementary Figure 1. **(A)** STED superresolution images of microtubules immunostained for α-tubulin (white) in RPE1 cells stably expressing CENP-A-GFP (colorful, confocal). Images show maximum intensity projection of the whole cell (left) and the inset of a single z-plane with the astral microtubule of interest (right), marked with the white square on the left image. Kinetochores are color-coded for depth with the brgbcmyw LUT in ImageJ throughout 12 z-planes, correspoding to 3.6 µm. Line Tool (length = 1 µm, thickness = 1) and Square Tool (25x25 pixel, corresponding to 0.5x0.5 µm) from ImageJ are drawn on the inset and represent tools to measure the intensity profile of the astral microtubule and the mean intensity of the nearby background, respectively. The graph on the right shows the intensity profile of the line drawn perpendicularly to the astral microtubule in the STED image inset. The resolution is defined as the width of the peak at its half-maximum, after subtracting the background. **(B)** Time-lapse LLS images of RPE1 cells stably expressing CENP-A-GFP and Centrin1-GFP (colorful, lattice light-sheet). Images show maximum intensity projections of 29, 34 and 40 z-

planes (4.2-5.8 µm) covering the whole cell, respectively. The blue arrow represents a polar kinetochore, orange and yellow arrows represent non-polar kinetochores located behind the pole or between the poles at NEBD, respectively. All kinetochores are tracked from NEBD until alignment to the spindle equator. Kinetochores are color-coded for depth with the brgbcmyw LUT in ImageJ. **(C)** Schematic representation of three groups of kinetochores. Blue kinetochores represent polar kinetochores located behind the spindle pole at NEBD and at their first contact with the spindle. Orange kinetochores represent non-polar kinetochores that are located behind the spindle pole at NEBD but between the two poles when they make their first contact with the spindle. Yellow kinetochores represent non-polar kinetochores located between the spindle poles at NEBD and during their first contact with the spindle. Colors for each group correspond to arrows in (B). **(D)** Univariate scatter plot of the number of chromosomes located behind the pole at NEBD and at their first contact with the spindle. Each color represents the same cell at each time point. N = 24 cells from 8 experiments. Statistical analysis: t-test. **(E)** Univariate scatter plot of the time from NEBD until the end of centripetal movement, landing and alignment. Each color represents the same kinetochore pair. N = 39 kinetochore pairs in 20 cells from 8 experiments. **(F-J)** Univariate scatter plot of the (F) distance to centrosome center at NEBD, (G) landing time, (H) time gap from the end of centripetal movement until landing, (I) time from NEBD to centripetal movement, and (J) time from landing to alignment for the three groups of kinetochores described in (C). Each color represents one kinetochore pair. N = 11 kinetochore pairs in 10 cells from 7 experiments. Statistical tests: Anova with post-hoc Tukey test. **(K)** The fractions of kinetochore pairs next to microtubules (blue) and without microtubules in their proximity (gray) during NEBD, centripetal movement and at the end of centripetal movement. N = 241 kinetochore pairs in 15 cells from 6 experiments (NEBD), 73 kinetochore pairs in 4 cells from 3 experiments (centripetal movement), 11 cells from 4 experiments, where all kinetochore pairs located behind the pole had a microtubule attached to them (end of centripetal approaching). **(L)** STED superresolution images of microtubules immunostained for α-tubulin (white) in RPE1 cells stably expressing CENP-A-GFP (blue, confocal) at NEBD and at the end of centripetal movement. Images show a single z-plane at NEBD and a maximum intensity projection of 23 z-planes (6.9 µm) covering the whole cell at the end of centripetal movement. Two types of attachments (attached vs. unattached) are shown in insets from NEBD. **(D-J)** Boxes represent standard deviation (dark gray), 95% confidence interval of the mean (light gray) and mean value (black). **(A,B,L)** Scale bars, 2 µm.

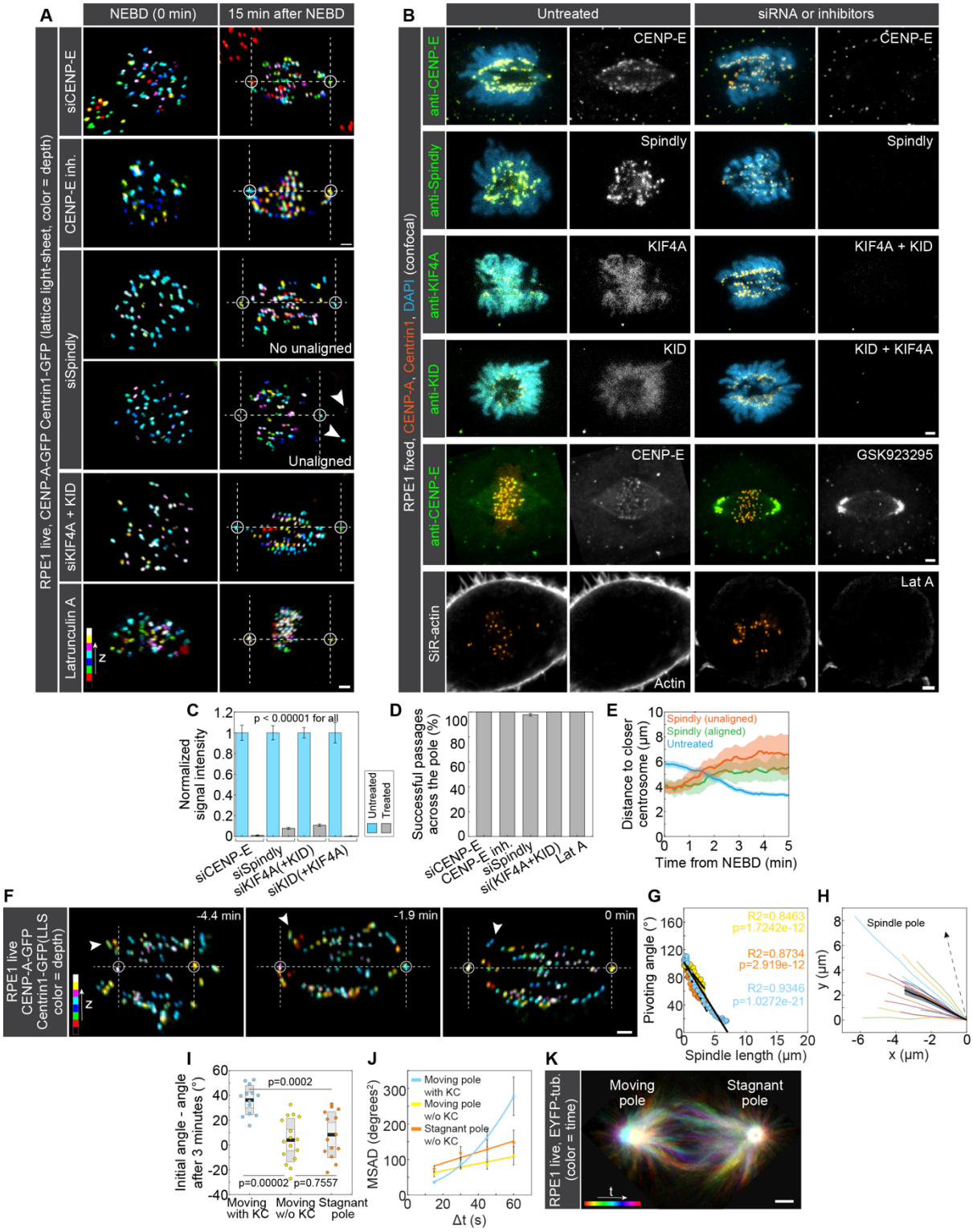

1722

1723 **Supplementary Figure 2. (A)** Time-lapse images of RPE1 cells stably expressing CENP-A-
1724 GFP and Centrin1-GFP (colorful, lattice light-sheet) after CENP-E depletion by siRNA,
1725 CENP-E inhibition by 80 nM GSK923295, Spindly depletion by siRNA, KIF4A/Kid co-
1726 depletion by siRNA, and actin depolymerization by Latrunculin A treatment. Images show
1727 maximum intensity projections of the whole cell. Kinetochores are color-coded for depth with
1728 the brgbcmyw LUT in ImageJ throughout 27-77 z-planes, corresponding to 3.9-11.2 µm. White
1729 arrowheads mark unaligned kinetochores after Spindly depletion. **(B)** Validation of protein

depletion by siRNA, CENP-E inhibition, and actin depolymerization. Columns 1 and 2 show untreated cells, and columns 3 and 4 treated cells. Columns 1 and 3 display merged channels of confocal images, and columns 2 and 4 only the protein of interest. Cells were immunostained for the proteins of interest denoted in images in column 2 (shown in green in merged images, except for actin which was stained by SiR-actin and shown in white), and the treatments are denoted in images in column 4. RPE1 cells stably expressing CENP-A-GFP and Centrin1-GFP (both in orange) were used, with chromosomes stained with DAPI (blue, rows 1-4), except in row 5, where RPE1 cells stably expressing CENP-A-GFP were used. Images are maximum intensity projections of the whole cell (33 z-planes), corresponding to 16.5 µm, except row 6, which is a single plane. Note that inhibition of actin polymerization by latrunculin A was additionally validated by retraction and rounding of interphase cells. **(C)** Normalized signal intensity for siRNA treatments in (B) for untreated (blue) and treated (gray) cells. N = 36 control and 36 CENP-E siRNA-treated cells from 3 experiments. N = 32 control and 30 Spindly siRNA-treated cells from 3 experiments. N = 37 control and 35 KIF4A/Kid siRNA-treated cells from 3 experiments stained with KIF4A antibody. N = 33 control and 30 KIF4A/Kid siRNA-treated cells from 3 experiments stained with Kid antibody. Statistical test: Mann-Whitney U test. **(D)** Fraction of successful passages of polar kinetochore pairs across the spindle pole in cells treated with CENP-E siRNA, CENP-E inhibitor GSK923295, Spindly siRNA, KIF4A+Kid siRNA, and latrunculin A. Successful passage was defined as passage across the 90° mark with respect to the spindle axis within 15 minutes from NEBD. All polar kinetochores moved across the pole within 15 minutes from NEBD in all treatments, except for Spindly depletion. N >150 polar kinetochore pairs in 11 cells from 3 experiments for CENP-E siRNA. N >300 polar kinetochore pairs in 22 cells from 2 experiments for CENP-E inhibition by GSK923295. N = 188 polar kinetochore pairs in 12 cells from 6 experiments for Spindly siRNA, 4 out of which failed to pass the pole. N >100 polar kinetochore pairs in 10 cells from 3 experiments for KIF4A+Kid siRNA. N >100 polar kinetochore pairs in 10 cells from 4 experiments for Latrunculin A. Note that, for cases in which all polar kinetochores crossed the pole within 15 minutes of NEBD, we did not directly count kinetochores per cell, but instead estimated a conservative lower bound based on the average number of polar kinetochores per cell at NEBD. **(E)** Distance of a polar kinetochore pair to the closer centrosome in time for polar kinetochore pairs in untreated cells (blue), polar kinetochore pairs in Spindly depletion that successfully crossed the pole (green) and polar kinetochore pairs that failed to cross the pole (orange). Values are shown as mean (dark line) and SEM (shaded areas). N = 39 polar kinetochore pairs in 20 untreated cells from 8 experiments. N = 4 polar kinetochore pairs that successfully crossed the pole in 3 Spindly-depleted cells from 2 experiments. N = 4 polar kinetochore pairs that failed to cross the pole in 3 Spindly-depleted cells from 2 experiments. **(F)** Time-lapse images of RPE1 cells stably expressing CENP-A-GFP and Centrin1-GFP (colorful, lattice light-sheet). Images show maximum intensity projections of the whole cell. Kinetochores are color-coded for depth with the brgbcmyw LUT in ImageJ throughout 34-38 z-planes, corresponding to 4.9-5.5 µm. White arrows represent one polar kinetochore tracked from the end of centripetal movement until it passed the spindle pole and landed on the main spindle surface (t = 0 minutes). **(G)** The anticorrelation between the pivoting angle and the spindle length for three individual polar kinetochore pairs as in (F). Linear regression. N = 3 randomly chosen polar kinetochore pairs in 3 cells from 3 experiments. **(H)** The shape of astral

1774 microtubules with attached polar kinetochores tracked mid-pivoting. The spindle pole is
1775 located in (0,0). N = 16 microtubules in 10 cells from 4 experiments. Values are shown as mean
1776 (dark line) and SEM (shaded areas) and individual microtubules are depicted in colors. **(I)**
1777 Pivoting angle change over a period of 3 minutes from the beginning of pivoting for astral
1778 microtubules with polar kinetochores attached to them on the moving pole (blue), microtubules
1779 without polar kinetochores attached to them on the moving pole (yellow) and microtubules
1780 without polar kinetochores attached to them on the stagnant pole (orange). N = 13 microtubules
1781 with polar kinetochores attached to them on the moving pole in 9 cells from 4 experiments. N
1782 = 16 microtubules without polar kinetochores attached to them on the moving pole in 10 cells
1783 from 4 experiments. N = 14 microtubules without polar kinetochores attached to them on the
1784 stagnant pole in 6 cells from 4 experiments. Boxes represent standard deviation (dark gray),
1785 95% confidence interval of the mean (light gray) and mean value (black). Statistical test: Anova
1786 with post-hoc Tukey test. **(J)** Mean squared angular displacement (MSAD) for astral
1787 microtubules with polar kinetochores attached to them on the moving pole (blue), microtubules
1788 without polar kinetochores attached to them on the moving pole (yellow) and microtubules
1789 without polar kinetochores attached to them on the stagnant pole (orange). MSAD = v^2t^2 +
1790 $2D_{MT}\Delta t$ + offset for microtubules with polar kinetochores attached to them on the moving pole
1791 and MSAD = $2D_{MT}\Delta t$ + offset for the other two groups of microtubule (Berg, 1993). R2 =
1792 0.999, 0.841 and 0.913, respectively. Error bars represent SEM. N = 16 microtubules with polar
1793 kinetochores attached to them on the moving pole in 10 cells from 4 experiments. N = 16
1794 microtubules without polar kinetochores attached to them on the moving pole in 10 cells from
1795 4 experiments. N = 14 microtubules without polar kinetochores attached to them on the
1796 stagnant pole in 6 cells from 4 experiments. **(K)** An image of an RPE1 cell stably expressing
1797 EYFP-tubulin (colorful, confocal) and H2B-mRFP (not imaged) with added HaloTag-CENP-
1798 A (not shown). The image is a temporal maximum intensity projection of the spindle and
1799 centrosome movements over 3 central z-planes (3 µm) and a time period of 4.5 minutes, color-
1800 coded for time with the Spectrum LUT in ImageJ. **(A,B,F,K)** Scale bars, 2 µm.

1801

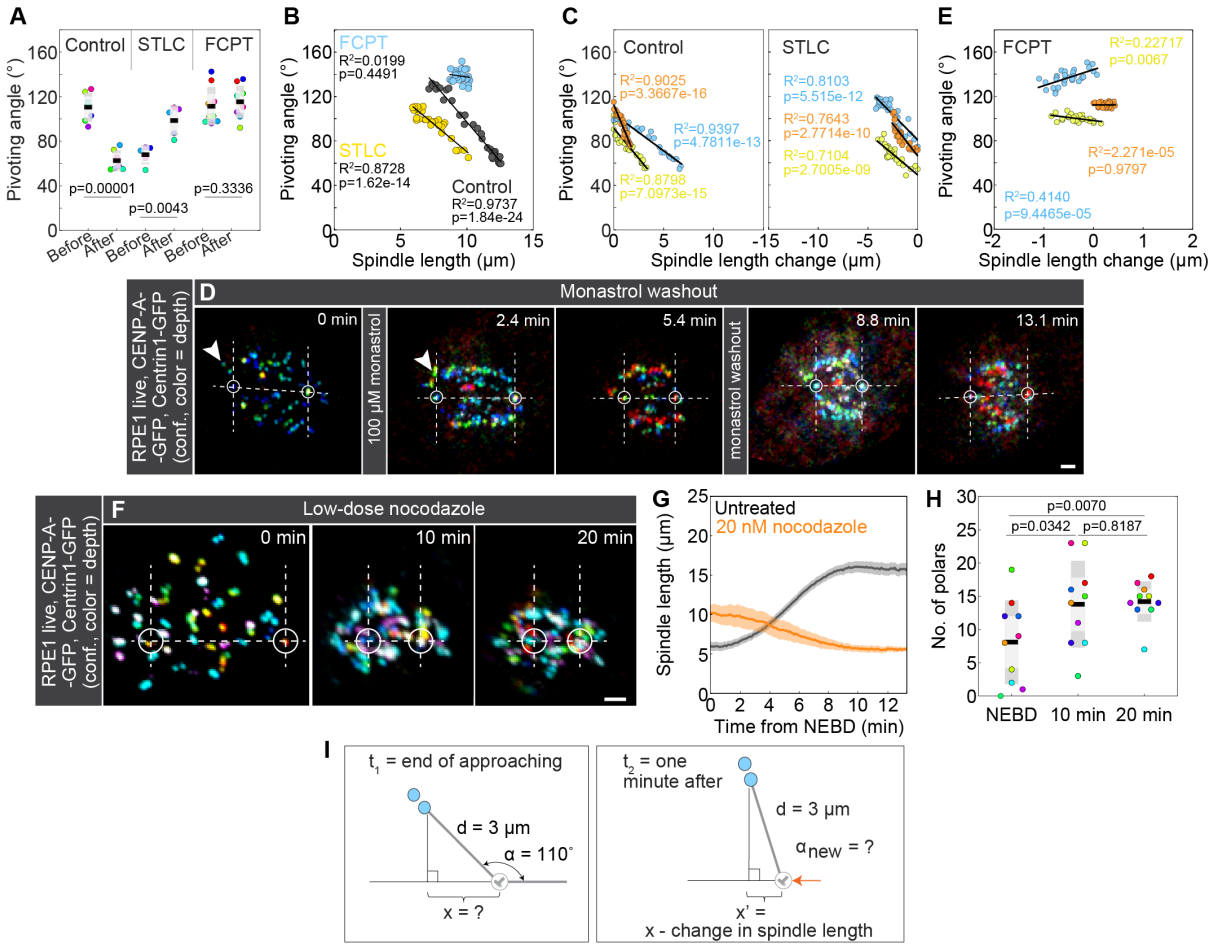

Supplementary Figure 3. (A) Univariate scatter plot of the pivoting angle before and 5 minutes after the addition of DMSO (left), STLC (middle) and FCPT (right). Each color represents a different kinetochore pair. If landing occurred less than 5 minutes after the addition of DMSO, it was taken as the final step instead. N = 7 kinetochore pairs in 7 cells from 7 experiments (DMSO), 5 kinetochore pairs in 3 cells from 3 experiments (STLC), 9 kinetochore pairs in 7 cells from 7 experiments (FCPT). Statistical test: paired t-test. **(B)** Anticorrelation of the pivoting angle and spindle length for the control, STLC and FCPT treatment. N = 1 kinetochore pair from 1 cell and 1 experiments for each. **(C)** Anticorrelations of the pivoting angle and spindle length change for three other kinetochore pairs in control (left) and STLC treatment. N = 3 kinetochore pairs in 3 cells from 3 experiments. **(D)** Time-lapse images of an RPE1 cell stably expressing CENP-A-GFP and Centrin1-GFP (colorful, confocal) for monastrol treatment and washout. White circles represent spindle poles, horizontal dashed lines represent the long spindle axis and lines perpendicular to it denote the borders of the polar region. Monastrol treatment caused spindle shortening and was reversed by washout. Kinetochores are color-coded for depth with the brgbcmyw LUT in ImageJ. **(E)** Pivoting angle versus spindle length change for three kinetochore pairs in FCPT treatment. N = 3 kinetochore pairs in 3 cells from 3 experiments. **(F)** Time-lapse lattice light-sheet images of RPE1 cells stably expressing CENP-A-GFP and Centrin1-GFP (colorful, confocal) in low-dose nocodazole treatment (20 nM). Images are maximum intensity projections of the whole cell. Kinetochores are color-coded for depth with the brgbcmyw LUT in ImageJ throughout 37-52 z-planes, corresponding to 5.4-7.5 µm. White circles represent spindle poles, dashed lines

1824 represent the long spindle axis and lines perpendicular to it denote the borders of the polar
1825 region. **(G)** Change of spindle length in time from NEBD for untreated (gray) and cells treated
1826 with 20 nM nocodazole (orange). Values are shown as mean (dark line) and SEM (shaded
1827 areas). N = 20 untreated cells from 8 experiments. N = 10 nocodazole-treated cells from 4
1828 experiments. **(H)** The number of chromosomes behind the pole at NEBD and 10 and 20 minutes
1829 after NEBD for cells treated with 20 nM nocodazole. Each color represents one cell. N = 10
1830 cells from 4 experiments. Statistical test: repeated measures Anova. **(I)** Schematic
1831 representation for calculating the theoretical line shown in Figure 3H. d = distance between the
1832 closer spindle pole and the kinetochore pair (measured in Supplementary Figure 2E), x =
1833 distance between the spindle pole and the orthogonal projection of the kinetochore pair onto
1834 the spindle axis, x' = x – change in spindle length, α = pivoting angle, α_{new} = calculated as the
1835 arccos (x'/d). The values of d and α were obtained from the DMSO and STLC experiments.
1836 **(A,H)** Boxes represent the standard deviation (dark gray), 95% confidence interval of the mean
1837 (light gray) and mean value (black). **(B,C,E)** Linear regression. **(D,F)** Scale bars, 2 µm.

1838

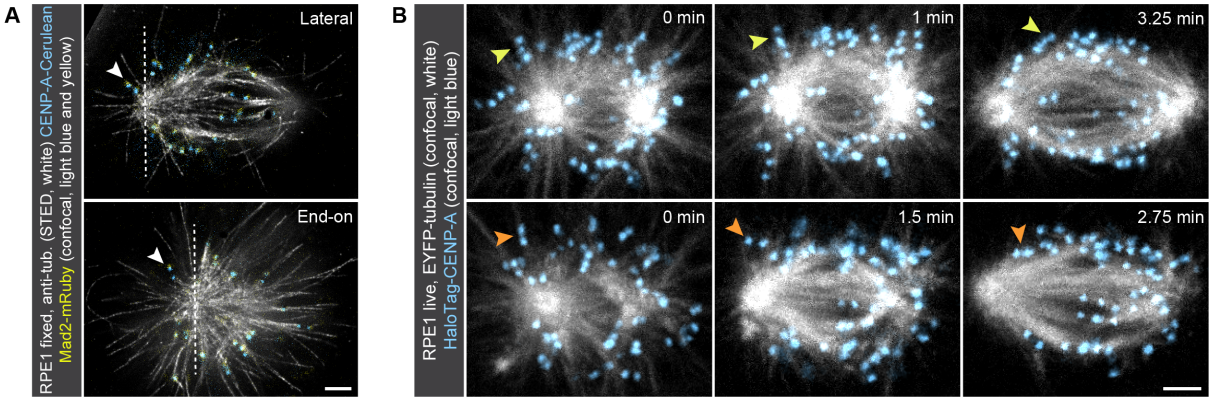

Supplementary Figure 4. **(A)** STED superresolution images of microtubules immunostained for α-tubulin (white) in RPE1 cells stably expressing CENP-A-Cerulean (blue) and Mad2-mRuby (yellow). Images show single z-planes of spindles with laterally or end-on attached polar kinetochores shown in Figure 4. **(B)** Time-lapse confocal images of RPE1 cells stably expressing EYFP-α-tubulin (white) and H2B-mRFP (not imaged) with added HaloTag-CENP-A (blue). The first row represents a kinetochore pair that constantly remains attached to the same microtubule during pivoting. The second row represents a kinetochore pair that changes the attachment of its further kinetochore during pivoting from lateral to bilateral. The images are maximum intensity projections of 3 central z-planes spanning 3 µm. Kinetochores are smoothed with 0.75-mm-sigma Gaussian blur. **(A-B)** Scale bars, 2 µm.

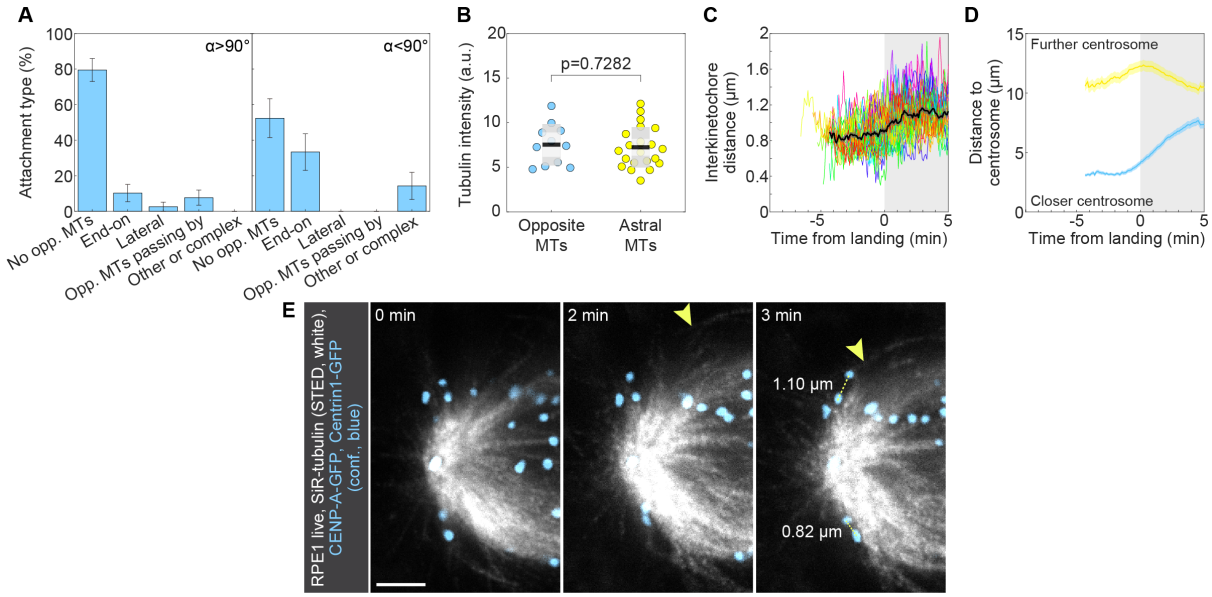

Supplementary Figure 5. (A) Percentage of different attachment types with microtubules from the opposite side of the spindle for kinetochores between the end of centripetal movement and landing as measured from STED images in the areas with the pivoting angle above or below 90°. N = 8 kinetochore pairs in 8 cells from 3 experiments for above 90°. N = 10 kinetochore pairs in 9 cells from 4 experiments for below 90°. **(B)** Univariate scatter plot of the tubulin intensity for microtubules that come from the opposite side of the spindle and attach to polar kinetochores (blue) and astral microtubules (yellow). Boxes represent the standard deviation (dark gray), 95% confidence interval of the mean (light gray), and mean value (black). N = 11 opposite microtubules in 10 cells from 4 experiments. N = 22 astral microtubules in the same 10 cells from 4 experiments. Statistical test: t-test. **(C)** Interkinetochore distance of polar kinetochores over time from the end of centripetal movement. Different colors correspond to different kinetochore pairs. N = 39 kinetochore pairs in 20 cells from 8 experiments. **(D)** Distance to further (yellow) and closer (blue) centrosome over time for polar kinetochores from the end of centripetal movement. Values are shown as mean (dark line) and SEM (shaded areas). N = 39 kinetochore pairs in 20 cells from 8 experiments. **(E)** Time-lapse images from live-cell STED microscopy of RPE1 cells stably expressing CENP-A-GFP and Centrin1-GFP (blue, confocal) and stained with 100 nM SiR-tubulin (STED, white). Each image represents a single z-plane. The yellow arrow denotes the microtubule coming from the opposite side of the spindle. Dashed yellow lines represent the interkinetochore distance at landing. **(E)** Scale bar, 2 µm.

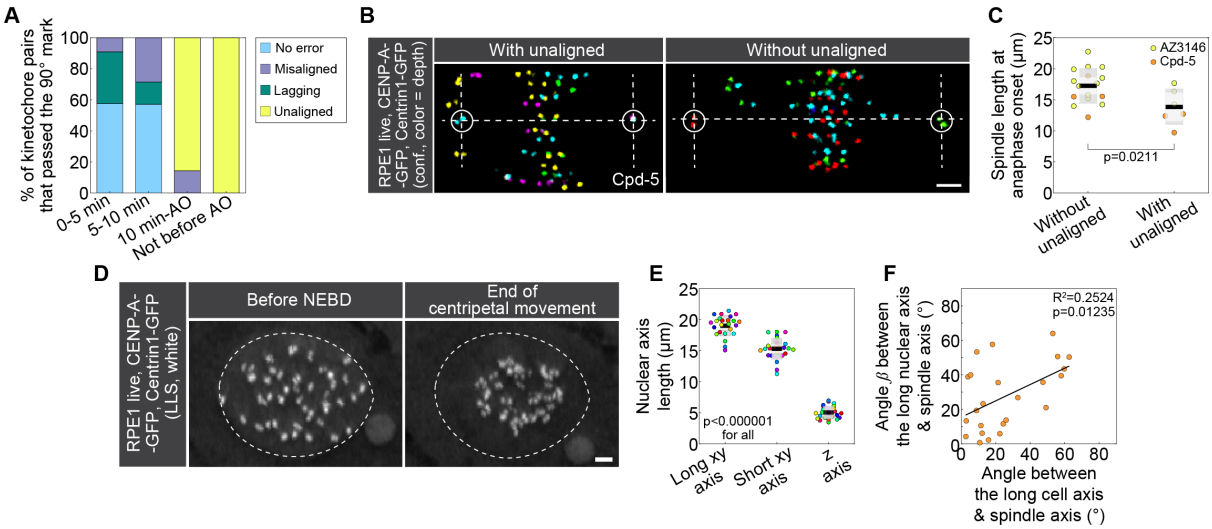

Supplementary Figure 6. (A) Fractions of kinetochore pairs that passed the 90° mark in the first five minutes after NEBD, between 5 to 10 minutes after NEBD, between 10 minutes after NEBD and the anaphase onset, and those that failed to pass the 90° mark before anaphase onset. Kinetochore pairs are classified as no error (blue), lagging (green), misaligned (purple) and unaligned (yellow). N = 52 kinetochore pairs initially located behind the pole in 7 cells from 4 experiments. **(B)** Images of RPE1 cells stably expressing CENP-A-GFP and Centrin1-GFP (colorful, confocal) and treated with Mps1 inhibitor Cpd-5. Images show maximum intensity projections of the imaged cells. The left panel represents cells with unaligned chromosomes and the right panel represents cells without unaligned chromosomes at anaphase onset. Circles depict the spindle poles and dashed lines the boundaries of the polar region. Kinetochores are color-coded for depth with the Spectrum LUT in ImageJ throughout 4 z-planes, corresponding to 4 µm. Cells were originally imaged as part of the dataset for (Klaasen et al., 2022). **(C)** Univariate scatter plot of the spindle length at anaphase onset for cells without (left) and with (right) unaligned chromosomes at anaphase onset. Cells are divided based on the treatment, to those treated with AZ3146 (yellow) or Cpd-5 (orange). N = 7 cells from 4 experiments for AZ3146. N = 15 cells from 4 experiments for Cpd-5. Statistical test: t-test. Cells with added Cpd-5 were originally imaged as part of the dataset for (Klaasen et al., 2022). **(D)** Time-lapse images of RPE1 cells stably expressing CENP-A-GFP and Centrin1-GFP (white, lattice-lightsheet). Images show maximum intensity projections of 36 and 42 z-planes covering the whole cell, corresponding to 5.2 µm and 6.1 µm, respectively. The left image represents the nucleus before NEBD and the right image represents the kinetochore and centrosome arrangement at the end of centripetal movement. Dashed lines denote the borders of the nucleus as outlined before NEBD. **(E)** Univariate scatter plot of the long xy nuclear axis length (left), short xy nuclear axis length (middle) and z nuclear axis length (right). N = 24 cells from 8 experiments. Statistical test: Anova with post-hoc Tukey test. **(F)** A correlation between the angle that the long nuclear axis in interphase forms with the spindle axis at the end of the centripetal movement and the angle that the long cellular axis in interphase forms with the spindle axis at the end of the centripetal movement. N = 24 cells from 8 experiments. Linear regression. **(C,E)** Boxes represent standard deviation (dark gray), 95% confidence interval of the mean (light gray) and mean value (black). **(B,D)** Scale bar, 2 µm.

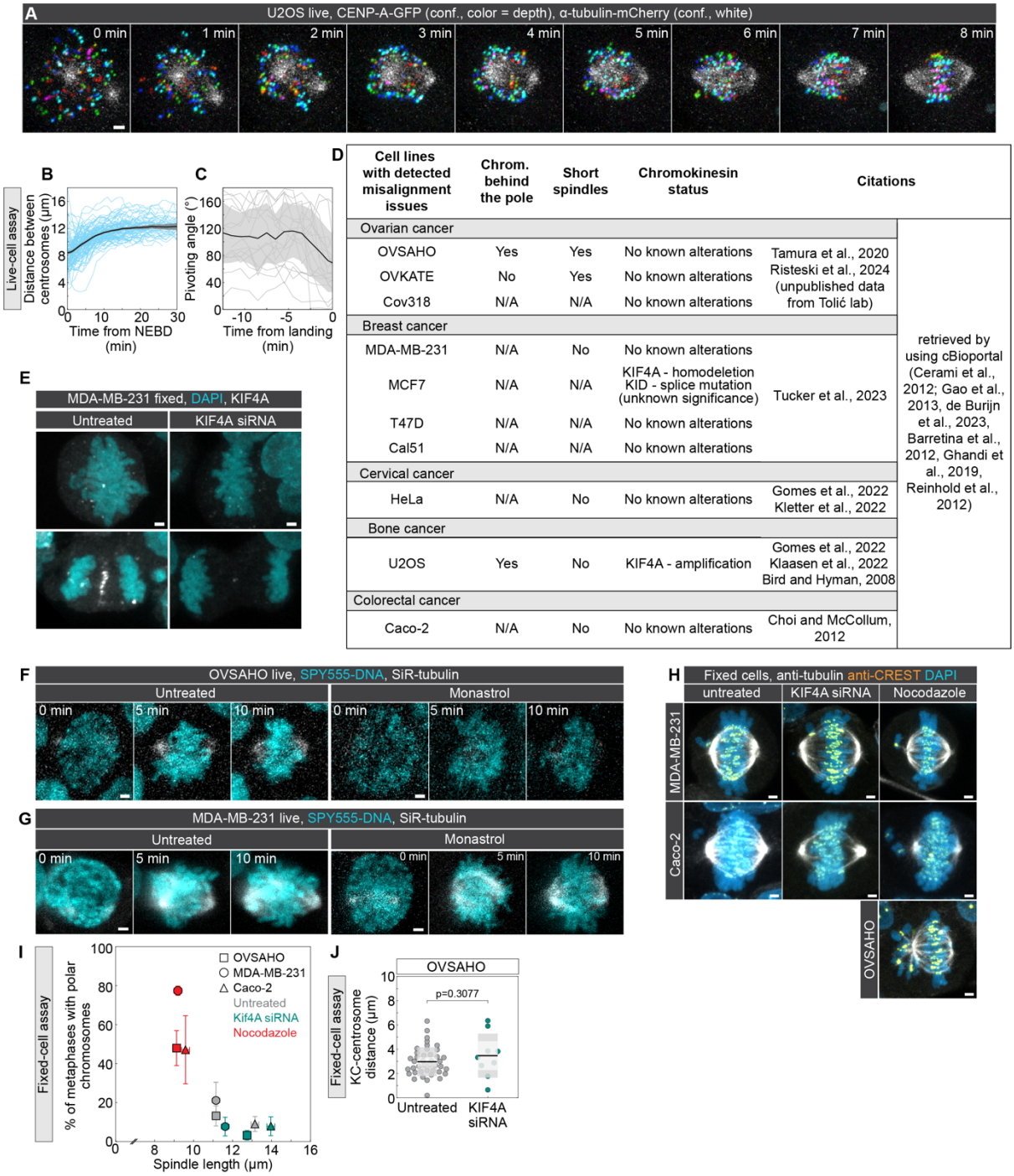

Cell lines with detected misalignment issues	Chrom. behind the pole	Short spindles	Chromokinesin status	Citations	
Ovarian cancer					retrieved by using cBioportal (Cerami et al., 2012; Gao et al., 2013, de Burijn et al., 2023, Barretina et al., 2012, Ghandi et al., 2019, Reinhold et al., 2012)
OVSAHO	Yes	Yes	No known alterations	Tamura et al., 2020	
OVKATE	No	Yes	No known alterations	Risteski et al., 2024 (unpublished data from Tolić lab)	
Cov318	N/A	N/A	No known alterations		
Breast cancer					
MDA-MB-231	N/A	No	No known alterations	Tucker et al., 2023	
MCF7	N/A	N/A	KIF4A - homodeletion KID - splice mutation (unknown significance)		
T47D	N/A	N/A	No known alterations		
Cal51	N/A	N/A	No known alterations		
Cervical cancer					
HeLa	N/A	No	No known alterations	Gomes et al., 2022 Kletter et al., 2022	
Bone cancer					
U2OS	Yes	No	KIF4A - amplification	Gomes et al., 2022 Klaasen et al., 2022 Bird and Hyman, 2008	
Colorectal cancer					
Caco-2	N/A	No	No known alterations	Choi and McCollum, 2012	

Supplementary Figure 7. (A) Time-lapse confocal images of a live U2OS cell stably expressing CENP-A-GFP (colored for depth) and α-tubulin-mCherry (white), showing how polar kinetochores transit across the pole during spindle elongation. **(B)** Spindle length over time for U2OS cells as in **(A)**, N = 115 cells. Thick line, mean; shaded area, SEM; thin lines, individual cells. **(C)** Pivoting angle of pairs of unaligned kinetochores over time until landing, where time 0 denotes landing on the main spindle surface calculated for each kinetochore pair, for U2OS cells as in **(A)**, N = 23 kinetochore pairs from 23 cells. Thick line, mean; shaded area, SEM; thin lines, individual kinetochore pairs. **(D)** Mini-screen of cancer cell lines for studying elongation-driven pivoting, from the literature (Barretina et al., 2012; Bird and Hyman, 2008; Cerami et al., 2012; Choi and McCollum, 2012; de Bruijn et al., 2023; Gao et

al., 2013; Ghandi et al., 2019; Gomes et al., 2022; Klaasen et al., 2022; Kletter et al., 2022; Reinhold et al., 2012; Risteski et al., 2024; Tamura et al., 2020; Tucker et al., 2023). **(E)** Images of fixed MDA-MB-231 cells, control (left) and treated with Kif4A siRNA (right), immunostained for Kif4A (white) and stained with DAPI (blue). **(F)** Time-lapse images of control (left) and treated with 15 µM monastrol (right) live OVSAHO cells stained with SPY-555-DNA (blue) and SiR-tubulin (white), imaged using lattice light-sheet microscopy. **(G)** Time-lapse images of control (left) and treated with 30 µM monastrol (right) live MDA-MB-231 cells stained with SPY-555-DNA (blue) and SiR-tubulin (white), imaged using lattice light-sheet microscopy. **(H)** Images of fixed immunolabeled cells of control (left column), KIF4A siRNA-treated (middle column), and nocodazole-treated (10 ng/mL, right column) MDA-MB-231 cells (top row), Caco-2 (middle row), and OVSAHO (bottom image). Cell are stained with anti-α-tubulin antibody (white), anti-CREST (orange) and DAPI (blue). **(I)** Fraction of fixed metaphase cells with polar chromosomes, i.e., at least one chromosome behind the pole, as a function of spindle length for fixed cells of 3 cancer cell lines (marked with different symbols as indicated). In the order of untreated (grey), Kif4A siRNA-treated (blue), and nocodazole-treated (10 ng/mL, red): N= 319, 157, 146 for OVSAHO, N= 128, 52, 115 for MDA-MB-231, and N= 122, 89, 138 for Caco-2. Error bars denote SEM. **(J)** Univariate scatter plot of the distance between the closer centrosome and the kinetochores of polar chromosomes for untreated (left) and KIF4A siRNA treated (right) fixed OVSAHO cells in metaphase. N = 39 chromosomes in 25 untreated cells from 3 experiments. N = 7 chromosomes in 6 KIF4A siRNA-treated cells from 2 experiments. Statistical test: t-test. Boxes represent standard deviation (dark gray), 95% confidence interval of the mean (light gray) and mean value (black). All scale bars, 2 µm.

1939 **Supplementary Videos**

1940 **Video 1.** RPE1 cells stably expressing CENP-A-GFP and Centrin1-GFP (colorful, lattice light-
1941 sheet). Kinetochores are color-coded for depth with the brgbcmyw LUT in ImageJ throughout
1942 32-40 z-planes. One polar kinetochore (white arrow) is tracked from NEBD until alignment to
1943 the spindle equator. Note that its passage across the polar region happens during the rapid
1944 movement of centrosomes (white circles) outwards. Scale bar, 2 µm.

1945 **Video 2.** RPE1 cells stably expressing EYFP-tubulin (white, confocal) and H2B-mRFP (not
1946 imaged) with added HaloTag-CENP-A (blue, confocal). Polar kinetochore (white arrow) is
1947 adjacent to the microtubule signal that pivots around the spindle pole towards the spindle
1948 surface. Scale bar, 2 µm.

1949 **Video 3.** RPE1 cells stably expressing EYFP-tubulin (white, confocal) and H2B-mRFP (not
1950 imaged) with added HaloTag-CENP-A (blue, confocal). Polar kinetochore (white arrow) is
1951 adjacent to the microtubule signal that pivots around the spindle pole towards the spindle
1952 surface. Scale bar, 2 µm.

1953 **Video 4.** RPE1 cells stably expressing EB3-GFP (white) and H2B-mCherry (blue). Note that
1954 spindle poles are moving rapidly outwards, while chromosomes remain stationary during this
1955 process. Scale bar, 2 µm.

1956 **Video 5.** RPE1 cells stably expressing CENP-A-GFP and Centrin1-GFP (colorful, lattice light-
1957 sheet) in DMSO control (left), STLC (middle) and FCPT (left) treatment. Kinetochores are
1958 color-coded for depth with the brgbcmyw LUT in ImageJ throughout 14-21 z-planes. In DMSO
1959 control cell, centrosomes (white circles) moved outwards, while polar kinetochore (white
1960 arrow) pivoted towards the spindle body. The situation was opposite in STLC treatment, where
1961 centrosomes moved inwards and polar kinetochore pivoted outwards. In FCPT treatment,
1962 spindle elongation was blockes and pivoting of polar kinetochore did not occur. Scale bar, 2
1963 µm.

1964 **Video 6.** RPE1 cells stably expressing CENP-A-GFP and Centrin1-GFP (colorful, lattice light-
1965 sheet) in monastrol treatment (left, duration 3 min 10 s) and after monastrol washout (right,
1966 duration 10 min 10 s). Kinetochores are color-coded for depth with the brgbcmyw LUT in
1967 ImageJ throughout 14-21 z-planes. Pivoting of polar kinetochore (white arrow) is driven by
1968 movement of centrosomes (white circle). Scale bar, 2 µm.

1969 **Video 7.** RPE1 cells stably expressing CENP-A-GFP and Centrin1-GFP (colorful, lattice light-
1970 sheet) and treated with Mps1 inhibitor AZ3146. The left movie represents cells without
1971 unaligned chromosomes and the right movie represents cells with unaligned chromosomes.
1972 Kinetochores are color-coded for depth with the brgbcmyw LUT in ImageJ throughout 14-21
1973 z-planes. White circles and arrows represent centrosomes and unaligned kinetochores,
1974 respectively. Scale bar, 2 µm.

1975 **Video 8.** RPE1 cells stably expressing CENP-A-GFP and Centrin1-GFP (white, lattice light-
1976 sheet). Note that the cell aligned the centrosomes along the long nuclear and cellular axis. Scale
1977 bar, 2 µm.

1978 **Video 9.** U2OS cell stably expressing EB3-GFP (white) and CENP-A-mCherry (blue) in early
1979 prometaphase, showing a region close to one centrosome (big white spot). Note that astral
1980 microtubules attached to a pair of polar kinetochores pivot around the centrosome towards the
1981 main spindle surface (in the clockwise direction). Time is given in min:s. Scale bar, 2 µm.

1982 **Video 10.** U2OS cell stably expressing CENP-A–GFP (color-coded by depth, left panel) and
1983 α-tubulin–mCherry (white, right panel), imaged from nuclear envelope breakdown until
1984 telophase. Note that all polar kinetochores pivot around and successfully pass the centrosome
1985 early in mitosis. Kinetochores are depth color-coded using the 16-color LUT across all acquired
1986 z-planes. Scale bar, 2 µm.

1987 **Video 11.** MDA-MB-231 cells stained with SPY-555-DNA (blue) and SiR-tubulin (white)
1988 imaged using lattice light-sheet microscopy. The left movie shows untreated cells, and the right
1989 movie shows cells treated with 30 µM monastrol. Note that the monastrol-treated cell has a
1990 delayed and reduced spindle elongation during prometaphase, leading to a delay in the
1991 movement of polar chromosomes. Scale bar, 2 µm.

1992 **Video 12.** OVSAHO cells stained with SPY-555-DNA (blue) and SiR-tubulin (white) imaged
1993 using lattice light-sheet microscopy. The left movie shows an untreated cell with chromosomes
1994 stuck at the spindle pole in metaphase (white arrow), and the right movie shows a Kif4A
1995 siRNA-treated cell. Note that in the Kif4A siRNA-treated cell the spindle elongated more
1996 rapidly, rescuing the phenotype observed in the untreated cell. Scale bar, 2 µm.